Automatic Control of Commercial Airliners in Formation Flight

by

Denzil Büchner

Thesis presented in fulfilment of the requirements for the degree of Master of Electronic Engineering in the Faculty of Engineering at Stellenbosch University

Department of Electrical and Electronic Engineering,
University of Stellenbosch,
Private Bag X1, Matieland 7602, South Africa.

Supervisor: Mr J.A.A. Engelbrecht

March 2015

Declaration

By submitting this thesis electronically, I declare that the entirety of the work contained therein is my own, original work, that I am the sole author thereof (save to the extent explicitly otherwise stated), that reproduction and publication thereof by Stellenbosch University will not infringe any third party rights and that I have not previously in its entirety or in part submitted it for obtaining any qualification.

March, 2015

Abstract

This thesis presents research contributing towards the automatic control of formation flight for commercial airliners. The motivation behind this research is to ultimately reduce fuel consumption of the trailing airliner through the utilisation of the aerodynamic coupling interactions between the trailing airliner and the wake vortices of the leading airliner.

A traditional model for an airliner in isolated flight is developed and expanded to include formation flight interactions as functions of the vertical and lateral separation between the trailing and leading airliners. A trim analysis is done, and resulting actuator trims are presented over ranges of lateral and vertical separation. Regions of reduced throttle setting are identified, as well as risks and challenges for maintaining formation within these regions. These regions comprise of a potentially risky and challenging region, coined the "sandwich region"; as well as a safer, more practically viable region, coined the "outer region". The former is a narrow region sandwiched between two regions that are untrimmable with respect to maximum aileron deflection, whereas the latter is only constrained by an inboard untrimmable bound, but has less significant drag reduction.

Subsequently, a state space representation is constructed, and a linear dynamics analysis follows. It is determined that the trimmed, uncontrolled trailing airliner is naturally unstable; hence a flight control system is required for stability. Furthermore, the analysis revealed that the dynamics stay essentially constant, especially for conventional modes, within the outer region. In the sandwich region however, the dynamics change much more drastically.

Next, a control system for the conventional airliner is designed based on the available information of current representative fly-by-wire systems; and its performance is analysed in formation flight scenarios by means of both linear and non-linear simulations. It is found that, given sufficiently high control law gains, particularly for lateral controllers, the conventional architecture is sufficient for maintaining formation. Additional structures are suggested, such as saturation elements to limit the lateral separation rate and acceleration; and a state machine controller, with states for entering and exiting the wake vortices. Following this, a robustness analysis was done by once again evaluating the linear dynamics over ranges of lateral and vertical separation; this time with the flight controllers augmented into the linear models. The robustness analysis proved that the controllers are robust against lateral and vertical separation perturbation, at least in the outer region.

Finally, a series of non-linear simulations prove the success of the control system in maintaining formation in various atmospheric turbulence conditions. Furthermore, the trailing airliner consistently has a reduced throttle setting, though with greater dynamic throttling compared to the leading airliner. Lastly, it is determined that the standard deviations of the control surface deflections of the trailing airliner are in the same order of magnitude as those of the leading airliner in simulations with moderate turbulence. Interestingly, it is found that the elevator deflection of the trailing airliner has a lower standard deviation than that of the leading airliner, possibly due to the leading airliner carrying the burden of regulating the formation's altitude.

Opsomming

Hierdie tesis handel oor navorsing wat 'n bydrae maak tot die outomatiese vlugbeheer van kommersiële passasiersvliegtuie in formasievlug. Die navorsing is gemotiveer deur die potensiële vermindering in die brandstofverbruik van die volgervliegtuig wat verkry kan word deur voordeel te trek uit die aerodinamiese koppeling tussen die volgervliegtuig en die nasleurvortekse van die voorste vliegtuig.

'n Tradisionele vlugmeganika model vir 'n passasiersvliegtuig is ontwikkel en uitgebrei om formasievlug-interaksies in te sluit, as funksies van die vertikale en laterale skeidingsafstande tussen die volgervliegtuig en die voorste vliegtuig. 'n Ewewig-analise is uitgevoer, en die nodige ewewig-instellings is bereken oor die bereik van moontlike laterale en vertikale skeidingsafstande. Twee gebiede van verminderde enjin-krag instellings is gedentifiseer, en die risikos en uitdagings verbonde aan formasievlug in hierdie gebiede is beskou. Twee gebiede is uitgeken: 'n uitdagende, potensiëel gevaarlike gebied, genoem die "sandwich" of "ingeperkte" gebied; en 'n veiliger, meer lewensvatbare gebied, genoem die "outer" of buitenste gebied. Die "ingeperkte" gebied is 'n baie nou gebied wat ingedruk is tussen twee ewewig-oninstelbare gebiede, waar aileron defleksie instellings vereis word wat die maksimum moontlike defleksies oorskry. Die "buitenste" gebied is 'n gebied wat net aan die binnekant begrens word deur 'n ewewig-oninstelbare gebied, maar wat nie so 'n groot besparing in brandstofverbruik bied as die "ingeperkte" gebied nie.

Vervolgens is 'n toestandsveranderlike voorstelling van die vlugdinamika afgelei, en 'n dinamiese analise is uitgevoer. Die dinamiese analise het gewys dat die ewewig-ingestelde, onbeheerde vliegtuig natuurlik onstabiel is, en dat 'n vlugbeheerstelsel benodig word om vlugstabiliteit te verseker. Daarby het die analise ook onthul dat die vlugdinamika baie min verander oor die bereik van die "buitenste" gebied, maar dat die vlugdinamika baie meer drasties verander oor die bereik van die "ingeperkte" gebied.

'n Konvensionele vlugbeheerstelsel vir die vliegtuig is volgende ontwerp, gebaseer op beskikbare inligting oor die argitektuur van tipiese "fly-by-wire" beheerstelsels wat tans op passasiersvliegtuie gebruik word. Die prestasie van die konvensionele vlugbeheerstelsel in formasievlugtoestande is ontleed deur middel van beide lineêre en nie-lineêre simulasies. Die simulasies het gewys dat die konvensionele vlugbeheerargitektuur in staat is om formasievlug te handhaaf, gegee dat voldoende hoë beheeraanwinste gebruik word. Bykomende strukture is voorgestel, insluitendend versadigingselemente om die koers en versnelling van die laterale skeidingsafstand te beperk; en 'n toestandsmasjien-beheerder, met toestande om die nasleurvortekse binne te gaan en te verlaat. 'n Robuustheidsanalise is ook gedoen, deur die geslotelusdinamika met die beheerders ingesluit te analiseer oor die bereik van laterale en vertikale skeidingsafstande. Die robuustheidsanalise het gewys dat die beheerders wel robuust is oor die bereik van beide laterale en vertikale skeidingsafstande, ten minste in die "buitenste" gebied.

Ten slotte is 'n omvattende reeks nie-lineêre simulasies uitgevoer om die vermoë van die vlugbeheerstelsel om formasievlug te behou te bevestig in 'n verskeidenheid van turbulensietoestande. Die simulasies het verder gewys dat die volgervliegtuig deurgaans 'n verminderde enjin-krag instelling het, maar met aansienlik meer dinamiese enjin-krag instelling variasies vergeleke met die voorste vliegtuig. Laastens het die simulasies gewys dat die standaard afwykings van die volgervliegtuig se beheeroppervlakdefleksies van dieselfde ordegrootte is as dié van die voorste vliegtuig. Interessant genoeg is bevind dat die elevator defleksies van die volgervliegtuig 'n laer standaardafwyking het as dié van die voorste vliegtuig, waarskynlik omdat die voorste vliegtuig die groter las dra om die formasie se hoogte te reguleer.

Acknowledgements

I would like to express my sincere gratitude to the following people and organisations for their contribution towards this thesis:

- Japie Engelbrecht – soon to be Dr Engelbrecht – for his invaluable, fundamental insight into flight mechanics and for leading me through our discovery of the workings of formation flight. Furthermore, thank you for helping me improve the quality of my work, through tedious sessions of proofreading.
- Prof. Chris Redelinghuys and Jordan Adams for sharing their wisdom regarding aerodynamics and formation flight mechanics. Also, especially Jordan for having vast amounts of patience while explaining his valuable insights to me.
- My best friend and girlfriend, Vereesé van Tonder, for listening to my woes, and giving me advice throughout the project, presentations and the write-up of this thesis. Thank you for keeping me motivated throughout it all! Also, a special thanks for helping me with some of the illustrations in this thesis!
- My office buddies, Cornelus le Roux and Chris Fourie, for being available for helpful discussions throughout the project. A special thanks to Cornelus for developing the turbulence model for the ESL, used in this thesis.
- Evert and Gerrie for double checking my work and spotting mistakes.
- My mom and dad for their support, both financially and emotionally, throughout this project; and for raising me to be the person I am today.
- The Airbus company and the NAC for financial support in the form of a bursary, and especially Airbus for providing the interesting topic.
- My friends, for distracting me and keeping my sanity in check.
- My uncles, Willem Büchner and Naas Venter, and aunt, Anette Venter; as well as a kind, but wise stranger, Dr Johannes van der Horst, for helping me with the much needed proofreading of the thesis!

Contents

List of Figures

List of Tables

Nomenclature

Acronyms

6-DOF	6 Degrees of Freedom
CT	Cross Track
DRD	Dutch Roll Damper
FPA	Flight Path Angle
NSA	Normal Specific Acceleration

Symbols

a_1	Tailplane lift coefficient
AR	Aspect ratio
$b, \bar{c}$	Wingspan, wing chord
b_f	Double the tailfin height
b_h	Tailplane span
c_{l_α}	2-D wing lift coefficient gradient
C_D	Drag coefficient
C_L	Lift coefficient
C_l	Rolling moment coefficient
C_m	Pitching moment coefficient
C_n	Yawing moment coefficient
C_S	Sideforce coefficient in stability frame
C_Y	Sideforce coefficient in body frame

C_X	Longitudinal force in body frame
C_Z	Vertical force in body frame
g	Gravitational acceleration
h	Mass centre position
h_0	Wing aerodynamic centre
I_{xx}, I_{yy}, I_{zz}	Moments of inertia in body frame
m	Aircraft mass (unloaded aircraft)
M	Mach number
n_z	Normal specific acceleration / Load factor
L, M, N	Moments coordinated in body axes
$\bar{q}$	Dynamic pressure ($\frac{1}{2}\rho\bar{V}^2$)
r_c	Core radius
S, S_f	Wing area, tailfin area
T	Thrust
u, v, w	Linear velocity components
p, q, r	Angular velocity components
$\bar{V}$	Freestream velocity / airspeed
$\bar{V}_s$	Speed of sound in air
V_f,V_T	Tail volume ratio, fin volume ratio
X, Y, Z	Longitudinal, lateral and vertical forces in body axes
α	Angle of attack
β	Sideslip angle
$\delta_a, \delta_e, \delta_r$	Aileron, elevator, rudder deflection angles
$\Delta\psi$	Relative heading/heading difference
ϵ	Downwash angle
γ	Flight path angle
ξ	Longitudinal separation normalised to wingspan
η	Lateral separation normalised to wingspan
ζ	Vertical separation normalised to wingspan
ζ_f	$\frac{b_f}{b}$

ζ_v	$\frac{z_v}{b}$
η_h	$\frac{b_h}{b}$
θ, ϕ, ψ	Pitch, roll and yaw angle
μ	$\frac{r_c}{b}$
ρ	Air density
σ	Downwash influence factor
τ	Moment influence factor

Subscripts

f	Tailfin
f'	Formation flight conditions
j	Leading airliner
k	Trailing aircraft
long	Longitudinal
lat	Lateral
t	Trim conditions

Chapter 1

Introduction

1.1 Background

There is increasing pressure to improve fuel efficiency in the passenger air-travel industry. It is largely driven by the increasingly thin operating margins due to the ever-rising fuel costs faced by airlines. This cost translates to greater travelling expenses for air-travelling passengers, which also increases pressure from the global community and the economy. Furthermore, concerns about climate change due to global warming, and health concerns due to air pollution, further drive the pressure for greater fuel efficiency to reduce the environmental impact of airliners.

This pressure has spurred research into improving the fuel efficiency of airliners. This includes the design of more efficient, lighter airframes and aerodynamic structures such as winglets, the development of more efficient fuels and bio-fuels, and better scheduling and routing of flights. One novel proposal calls for the formation flight of passenger aircraft as a contributing solution to the problem – and that is the focus of *this* thesis.

Airliners generate persisting wake vortices during flight, which trail behind them for miles. The complex interactions between the trailing airliner and the wake vortices generated by the leading airliner in formation flight result in a reduction of induced drag and ultimately reduced fuel consumption. This is also seen in nature, with geese flying in V-formations to conserve energy; and is also established from military formation flight exercises.

Wind-tunnel tests using models simulating formation flight have shown that drag reductions of as high as 25% may be achieved, depending on the configuration of the formation [1]. A higher-level analysis by Bower et al., showed that a 13% reduction in overall fuel consumption may be practically realised for commercial airliners when considering formation geometries and route optimisation [2].

A previous study performed by Mr N. Bizinos, and supervised by Prof C. Redelinghuys of the University of Cape Town investigated the aerodynamic interaction of the trailing airliner in formation flight, with the wake vortices generated by a leading airliner [3]. A model describing the

induced forces and moments due to these aerodynamic interactions was constructed, using incremental coefficients for each of the individual induced forces and moments. It was found that a highly non-linear relationship exists between the induced forces and moments, and the separation distance between the trailing airliner and the vortex core; and that the non-linearity was largest near the peak for optimum fuel-consumption reduction.

The results of this study lead to questions about the stability and performance of the flight control system of the trailing airliner in formation flight. The induced forces and moments would require unconventional trim settings for the trailing airliner's control surfaces, such as non-zero aileron and rudder deflections. The settings of the control surfaces would also be very sensitive to changes in the relative position of the trailing airliner, particularly near the optimum position for fuel-consumption reduction. This thesis addresses these questions and concerns.

1.2 Research Objectives

The objective of this research is to ultimately determine whether it is realistically possible to implement formation flight on commercial airliners through the use of feedback control systems. The approach that leads towards this overarching goal is divided into the following manageable outcomes:

1. An integrated mathematical model that captures the dynamics of the airliner in formation flight shall be constructed, from a representative flight mechanics model and the formation flight aerodynamic interaction model, developed by Bizinos [3].
2. The required trim settings for the engines and control surfaces of the trailing airliner shall be determined and analysed over ranges of lateral and vertical separation relative to the leading airliner.
3. The natural flight stability of the trailing airliner shall be analysed over ranges of lateral and vertical separation relative to the leading airliner.
4. The stability of a current, representative fly-by-wire system shall be analysed over ranges of lateral and vertical separation relative to the leading airliner.
5. An integrated simulation model for formation flight shall be constructed by incorporating a representative flight mechanics model, the current, representative fly-by-wire flight control system, and the aerodynamic interaction model.
6. The stability and performance of the representative fly-by-wire system shall be verified in full non-linear simulation.
7. Specialised requirements for formation flight shall be derived accordingly, and architectural changes or a new architecture elements shall be suggested to address the requirements of formation flight.

8. The performance of the new flight control system shall be illustrated using the integrated simulation model.

1.3 Related Work

Formation flight has become a popular topic of research over the last few decades. The modelling of the wake vortices; benefits and challenges of formation flight; and flight control systems, including flight scheduling and routing aspects, have been at the core of many research activities. A brief overview of a few of these studies will be given in order to establish an understanding of the current state of the industry, and discover possible unexplored avenues regarding the topic.

1.3.1 Benefits and Challenges of Formation Flight

Formation flight research over the last decades have verified that formation flight can effectively allow for increased flight range, via induced drag reduction. Various studies involving wind-tunnel tests have shown that, a drag reduction of up to 30% is achievable [1, 4–6]. Furthermore, Beukenberg and Hummel have shown that a mean reduction in required engine power of 10% is realistically obtainable for the trailing airliner in a two-ship formation, using analytical studies and flight-test measurements [4].

The induced reduction in drag is achieved through interactions of the trailing airliner's lifting surfaces with the pair of wake vortices generated by the leading airliner as it produces lift. When positioned outboard of the wake vortex pair, upwash is induced along the trailing airliner's lifting surfaces. This upwash is a function of the trailing airliner's position within the wake vortices, and swaps direction and becomes downwash as the trailing aircraft moves inboard of the wake vortices. When positioned within upwash, the trailing airliner experiences an effective increase in angle of attack, that increases the magnitude and direction of the induced aerodynamic forces and moments on its wings and empennage. The airliner can then be re-trimmed to take advantage of the increase in lift and reduction of drag, for an effective reduction of fuel consumption and greater range performance.

Along with the benefits of formation flight, potential hazards and challenges are also introduced. The trailing vortices induce large forces and moments, which can cause dangerous handling characteristics. At the optimal induced drag benefit region, the induced moments and side force become significant enough to demand large control surface deflections for trim, which reduces the realistically achievable benefit through unmodelled drag effects [7]. The hazard posed by the vortices of an airliner during take-off or landing is well-known and documented [8–12], where the induced rolling moment is particularly of concern [13].

1.3.2 Formation Flight Scheduling and Control Systems

The challenges in flight control and potential benefits associated with formation flight has spurred a large interest in the field of automated formation-flight control. A large portion of past and current research activities investigates aerial-refuelling and the formation flight of unmanned aerial vehicles. Only more recent studies have been investigating topics such as flight control systems for manned formation-flying aircraft.

Numerous studies [1–7,14–21] verify this trend of interest in formation flight due to the possibility of fuel consumption reduction. A concrete model for the aerodynamic interactions is often neglected however, or details on the implementation are unclear. In a paper by Zou et al. [14], the assumption was made that an uncertainty exists in the induced drag coefficient for the trailing aircraft in formation flight, and an adaptive algorithm was developed to estimate this drag coefficient in real-time. Following this, a control algorithm was developed to achieve formation flight within a practically small bounded tracking error; though the complete effects of the induced forces and moments were ignored.

Brodecki et al. illustrated similar concepts during a series of related studies, which assumed that the position of the sweet spot for fuel consumption reduction cannot practically be known. Their research addresses this issue by developing a control system that uses an advanced extremum seeking algorithm, which utilises an extended Kalman filter to estimate gradients within the wake vortex [15]. Furthermore, the emergent behaviour of this developed control system is investigated. The desired echelon formation commonly used in formation flight consistently emerges naturally after formation is initialised at random starting points, using a Monte Carlo scheme. This is achieved without inter-vehicle communication, using only minimal information about the other formation members, and the extremum seeking control system. This naturally drives each member to the sweet spot for fuel consumption minimisation, which corresponds to the echelon configuration [16].

Furthermore, numerous other studies approach the wake-sensing and estimation problem, but from different perspectives. Specifically, Henmati et al. conducted wake-sensing research, with the premise that formation flight cannot be optimally achieved without having knowledge of the leading airliner's wake position. A wake-sensing strategy is employed for estimating the position and strength of the wake vortex in a two-aircraft formation. The estimator synthesizes pressure-distribution measurements along the wing, taken an the trailing airliner, by making use of an augmented lifting-line model in conjunction with particle filters and a Kalman filter [17].

Okolo et al. approached the "sweet spot"-determination problem by first determining the optimal position in a static analysis using a wake model constructed through vortex lattice methods, and examining lift-to-drag ratios and other force and moment coefficients. The trailing airliner was then re-trimmed, and a dynamic simulation was used to determine whether the sweet spot moved significantly due to the new control surface trims and thrust requirements. The results of the dynamic simulation showed that the position of the sweet spot differed from that of the static analysis [18].

Besides the numerous, ongoing sweet spot determination and wake sensing research activities, many have also investigated the control systems side of the problem. Methodologies similar to that used in the Brodecki et al. studies discussed previously [15, 16] are often used; extremum-seeking control is investigated in numerous independent studies as a potential solution to the problem of being unable to deterministically know the position of the wake [19, 20]. The approach commonly begins with developing a wake model, sometimes based on a bound horseshoe vortex model. The optimum position for drag reduction is then estimated by means of a Kalman filter as was done by Chichka et al. [19], or by minimising the trailing airliner's pitch, as was done by Binetti et al. [20]. Extremum-seeking control techniques, such as sinusoidally perturbing the lateral and vertical separation, are employed to sense changes in drag, often using proxy states such as the pitch angle. The trailing airliner then tracks the most optimal position that was found in the local region.

Furthermore, various studies go beyond the lower-level details involved with the modelling and control aspects associated with formation flight, and focus instead on topics such as formation configuration and route optimisation. In a study by Xu et al. [21], the fuel and cost benefits of applying extended formation flight to commercial operations is investigated and discussed in great detail. Different configurations are considered; including the two-ship echelon formation, as well as the three-ship echelon formation, V formation and inverted-V formation. Furthermore, the problem of scheduling formation flights is investigated, and heuristic searches are suggested as a solution to finding viable candidates for formation grouping. Next, individual missions are optimised for either minimum cost or minimum fuel consumption, using gradient-based optimisation to reduce computational cost. Finally, high level scheduling optimisation is done to find the best combination of formation and solo missions, using a binary integer programming tool.

This thesis however, intends to explore a perceived void currently in the field; and develop and analyse a control system based on an incremental aerodynamic interaction model. Although overlapping or even more advanced work have already been explored in the field, new avenues will be explored and new findings will be presented. More advanced topics, such as wake-sensing and seeking, which has already been researched in detail [15, 16, 19, 20], will not be pursued during this thesis.

Instead, this thesis presents the first control systems research contributing towards a larger collaborative research effort between Stellenbosch University, the University of Cape Town, and the Airbus Company; and as such, intends to establish a firm base for future control systems research. Both the aerodynamic interaction model and the control systems design will improve in fidelity and complexity as the collaborative research project matures. Finally, the control systems developed during this thesis are kept as simple as possible, in order to best reflect current fly-by-wire systems used by commercial airliners [22, 23].

1.3.3 Aerodynamic Interaction Model

The wake model that is used in this thesis is the aerodynamic interaction model developed by Bizinos et al. [3]. Note that it is of lower fidelity and complexity compared to some other models, such as the model by Okolo et al. [18]. A major motivation for using this model is that many of the models used during other research projects are not readily available, as they were privately developed in software through vortex lattice methods, or were not discussed in enough detail to replicate easily. Contrary to this, Bizinos's model is available as a set of mathematical expressions, describing the induced force and moment coefficients as functions of the trailing airliner's relative position within the leading airliner's wake vortices; and as such, can easily be used by anyone who wishes to investigate the topic.

The second major reason for using Bizinos's model, is that it forms part of a larger, ongoing research collaboration, as previously discussed. Bizinos's model is the first model developed by our partners at the University of Cape Town, and a more mature model, though in development, was not yet ready during the course of this project. The model is essentially a set of mathematical expressions, describing the interactions between the trailing airliner and the leading airliner's wake vortices. It was developed to approximate the impact of formation flight on the comfort levels of passengers aboard the trailing airliner. It is a simple aerodynamic model that supports formations of 2 aircraft: a leader and a follower. The model was constructed using the bound horseshoe vortex model, as an approximation for two counter-rotating rolled-up trailing vortices, generated at the tips of the leading airliner's wing [3].

By integrating along the bound vortex span, expressions for the incremental force and moment coefficients are obtained. These expressions are dependent on the trailing airliner's relative wingspan-normalised position within the leading airliner's wake vortices. Furthermore, the model includes the effect of turbulence on the wake vortices, through simplifying approximations. This model is discussed in greater detail in Chapter 2.

1.4 Project Overview

The project is divided into the following 5 major sections, closely matching the general outline of this thesis:

1. Mathematical models for the mechanics of the conventional airliner in isolated flight are developed. Furthermore, these models are extended to include the aerodynamic interaction model for the trailing airliner in formation flight. This is discussed in Chapter 2.
2. The models developed in (1) are used to conduct formation flight mechanics analyses, pertaining to the trim and dynamic response of the trailing airliner; as discussed in Chapter 3. This reveals interesting characteristics of the trailing airliner due to the formation flight interactions, and sets a foundation for the design of the flight controllers for formation flight.

3. Chapter 4 discusses the design of the flight controllers for the conventional airliner in isolated flight. The designs are verified by means of full non-linear simulations throughout this section.
4. The flight controllers developed in (3) are extended for formation flight, as discussed in Chapter 5. These controller designs are also verified by means of full non-linear simulations.
5. Finally, Chapter 6 presents the results of the extended non-linear simulations performed. These simulations were done in order to evaluate the performance of the formation flight controllers in various levels of atmospheric turbulence, according to different metrics, such as position-tracking capability and throttle setting reductions.

1.5 Overview of Work

A comprehensive model was first developed for the flight mechanics of the conventional airliner in isolated flight. The model encapsulates kinetic and kinematics models, and uses aerodynamic, gravity and thrust models to drive the system through corresponding forces and moments, and is similar to approaches commonly encountered in literature [27–29]. Certain simplifying assumptions were made, including rectangular wings, as opposed to elliptic wings, with no sweep or dihedral. Furthermore, incompressibility effects due to large Mach numbers were ignored. Lastly, a simplistic first-order engine model was used with a time constant matching what is expected from available data.

The model's parameters and conventions were based on available data from the Boeing-747 modelling data document [23], as well as Condition 9 from a NASA flight test report [24]. The specific condition from the NASA report refers to a certain combination of trim parameters, such as airspeed and altitude, and yields aerodynamic coefficients corresponding to this condition.

The conventional model was then expanded to include the aerodynamic interaction model developed by Bizinos et al. [3]. This model describes the induced forces and moments on the trailing airliner, due to interactions with the wake vortices generated by the leading airliner. It makes the assumption that the derivatives of the induced forces and moments to longitudinal separation are small. The functions yielding the induced forces and moments are thus only dependant on lateral and vertical separations as variables, and not on longitudinal separation. The interaction model assumes a constant in-track distance of 10 wingspans.

Next, the isolated and formation flight mechanics models were translated into Simulink models, which allowed for the full non-linear simulation of isolated and formation flight. A Von Kármán turbulence model, based on the mathematical representation in the Military Specification MIL-F-8785C [25] and Military Handbook MIL-HDBK-1797 [26], was included in the Simulink models for increased fidelity. The turbulence model was then integrated with the aerodynamic interaction model, to simulate the effective perturbation of the wake vortices due to atmospheric turbulence.

Subsequently, trim and linear dynamics analyses were done to discover more about the underlying

mechanics of formation flight. Firstly, the trim analysis was done over ranges of lateral and vertical separation, in order to find the trim required to hold position within the leading airliner's wake, for each corresponding position. Furthermore, this analysis yields important conclusions about the potential operating regions of the trailing airliner in formation flight. These regions describe where formation flight is possible with regard to maximum control surface deflections. Trim requirements exceeding the maximum control surface deflections renders the trailing airliner physically incapable of maintaining formation within that region. Additionally, the required throttle setting eliminates certain regions, as they require an increased throttle setting at trim. This results in an increase in fuel consumption, making these regions undesirable for extended formation flight.

The full non-linear models for both the isolated airliner, as well as the trailing airliner in formation flight, were linearised in order to construct state space representations. These state space representations were then used to determine the linear dynamics and stability of the both the conventional and trailing airliners. Subsequently, the trailing airliner's dynamics was compared to that of the conventional airliner to make deductions about the effect of the formation flight interactions. This analysis was done for all discovered trim regions in order to draw comparisons between them.

A set of flight controllers, loosely based on a conventional fly-by-wire architecture [22, 23], was designed and verified in non-linear simulation. Multiple architectures for lateral control were suggested during this design, based on the bank-to-turn and skid-to-turn strategies. Following this, the controllers were extended to allow for the tracking of the leading airliner at a fixed relative position. The design of the controllers included minor architectural changes, as well as iterative redesign of control laws, though these control laws were fed back into the conventional controllers as well.

Furthermore, additional structures, such as saturation elements, were added to the architecture to improve safety and performance for large step inputs of vertical, lateral and longitudinal separation. Additionally, a rudimentary state machine controller was added with states for entering the wake and maintaining formation at a specified relative separation. Throughout the design of the formation flight controllers, the design was verified in non-linear simulation.

A robustness analysis was then performed to determine whether the controllers were robust to perturbation in lateral and vertical separation. This was done by means of a linear dynamics analysis; specifically using individual root locus plots over ranges of lateral and vertical separation, based on the full, closed-loop linear models augmented with the flight controllers.

Lastly, extended non-linear simulations were done in order to determine the performance of the controllers over extended durations; this was done under various atmospheric turbulence conditions, including moderate and severe turbulence. The performance was evaluated under metrics of position tracking, mean engine setting and dynamic engine throttling, and control surface deflection.

Chapter 2

Mathematical Models

The development of the mathematical models for both the conventional airliner in isolated flight, as well as the trailing airliner in formation flight, will serve as a foundation for all analyses, control systems design and simulations that will be done in this thesis. It is thus very important that these models are verifiable and as accurate as possible. Where appropriate, certain simplifying assumptions will be made at the cost of accuracy, though only where doing so is defensible. The approaches taken for the derivation of the conventional models are based on approaches which are standard to the industry [27–29]; and the formation flight models are an extension of this, but based on the derivations by Bizinos and Redelinghuys [3]. Furthermore, ideal sensors are assumed; and as such, sensor noise and bias are not modelled.

2.1 Reference Frames and Conventions

A number of axis systems are used in the development of the conventional flight mechanics and formation flight interaction models.

2.1.1 Conventional Axis Systems

The conventional aircraft uses 4 major, orthogonal axis systems: the body axes, wind axes, stability axes and inertial axes. Note that these axis systems are discussed here as defined in the Boeing-747 modelling data document [23]. The wind axis system definition differs slightly from that in popular literature, by Cook [28]. The major difference is that in Cook, the wind and stability axes are synonymous. The wind axes in the Boeing-747 modelling data document however, are defined with the x_w-axis coinciding with the relative wind vector.

2.1.1.1 Body Axes

The body axes, shown in Fig. 2.1, are bound to the airliner's fuselage, with the origin coinciding with the airliner's centre of mass. The x-axis runs along the fuselage, the y-axis is perpendicular to the aircraft's plane of symmetry and points in the direction of the starboard wing-root, and the z-axis completes the orthogonal axis system, pointing downwards relative to the fuselage.

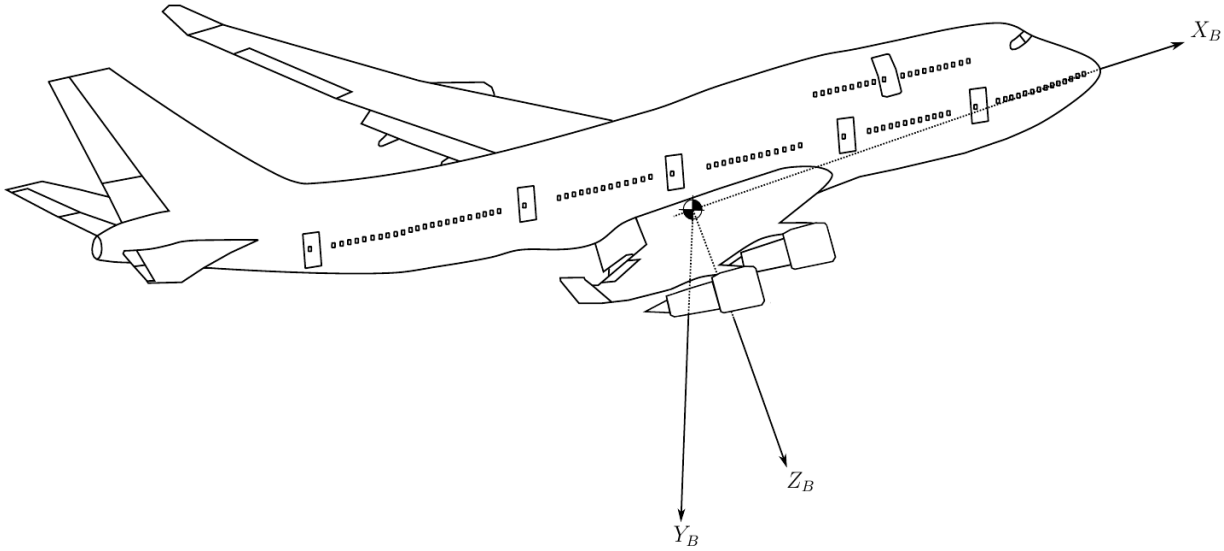

Figure 2.1: Conventional body axis system

2.1.1.2 Stability and Wind Axes

The stability axes are useful for supporting the calculations of the aerodynamic forces and moments acting upon the airframe. However, the body axis system is required for finally resolving and applying all forces and moments – including gravity, thrust and aerodynamics – to the airliner's body.

The transformations from wind to body axes are supported by the stability axes, as illustrated in Fig. 2.2. The x_w-axis coincides with the incoming wind vector, which further corresponds to the velocity vector of the airliner in a still-air environment. A rotation of the wind axes around the z_w-axis by the sideslip angle β, results in the stability axes. The resulting y_s-axis then coincides with y_b-axis, but the z_s-axis still coincides with the z_w-axis. Further, the x_w- and y_w-axes lie in a plane formed by the x_s- and y_s-axes. If a rotation α is then applied to the stability axes around the y_s-axis, the result is the body axes. This means that the x_s-axis lies in the x-z plane of symmetry of the airliner, and is thus rotated about z_s away from the relative wind vector, by the sideslip angle, β.

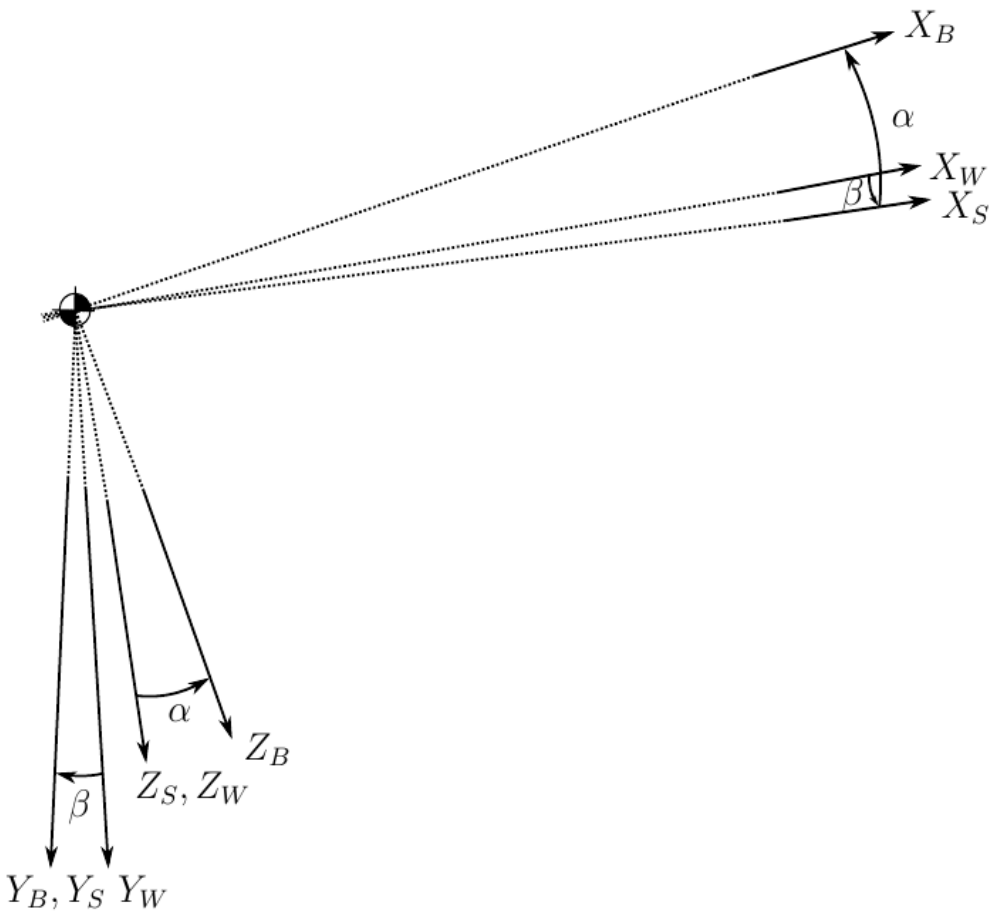

Figure 2.2: Body, stability and wind axes transformations

2.1.1.3 Inertial Axes

The inertial axes are used to represent the airliner's position in physical space. A simple North-East-Down (NED) orthogonal coordinate system is used for this purpose, with the x-, y- and z-axes corresponding to North, East and Down respectively. This axis assumes a fixed, non-rotating Earth. The effect of the Earth's rotation is significantly slow, and will be rejected by the control systems. Furthermore, as this thesis investigates formation flight controllers, relative positions are of interest, and the effect of the rotation is reduced as both the leading and trailing airliners will experience this.

2.1.1.4 Sign Conventions

Fig. 2.3 illustrates the appropriate sign conventions, as per definition in the Boeing-747 modelling data document [23]. Positive aileron, elevator and rudder deflections (δ_A, δ_E, δ_R), cause negative pitching, rolling and yawing moments (l, m, n) respectively. Regarding the ailerons, a positive deflection is defined as a downwards deflection of the trailing edge of the left-hand wing, and vice versa for that of the right-hand wing.

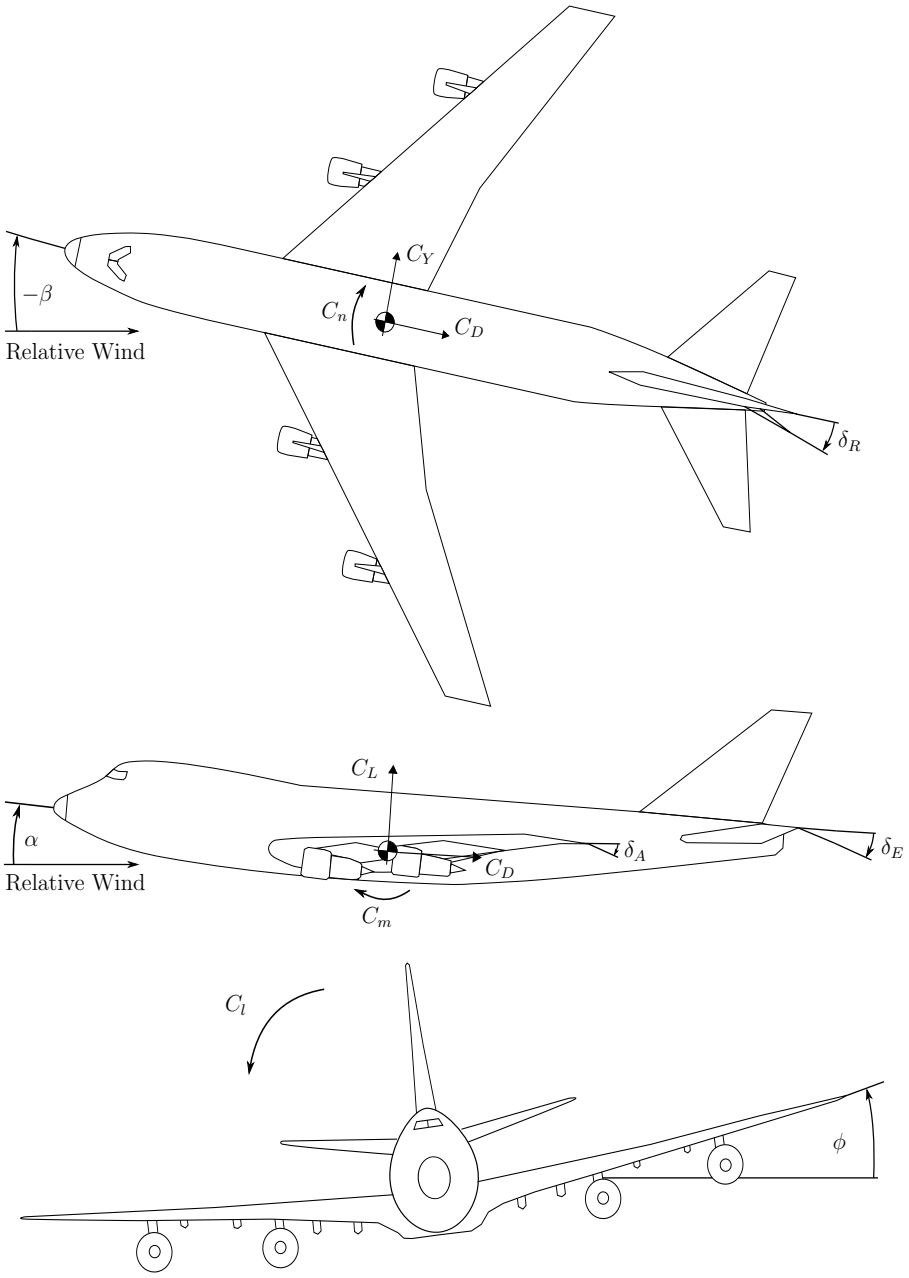

Figure 2.3: Standard sign conventions for actuators and moments

2.1.2 Relative Separations

The relative separation between the trailing and leading airliners is called the instantaneous separation. It is analogous to DGPS measurements or differential inertial coordinates, mapped to the

inertial axes of the straight formation track. The orientation of the leading airliner's stability axes is used to approximate the inertial axes of the track. Fig. 2.4 shows the instantaneous separations, Δx, Δy and Δz, between the leading and trailing airliners, using top and side views of the formation. The instantaneous separations can be measured between the centres of mass of each airliner, though this need not be the case. The point from which to measure only needs to be consistent for each airliner. Normalising the instantaneous separations, Δx, Δy and Δz, by wingspan b, yields longitudinal separation ξ, lateral separation η and vertical separation ζ respectively. The instantaneous separation is the likely choice of input to the outer-loop controllers that will eventually be designed.

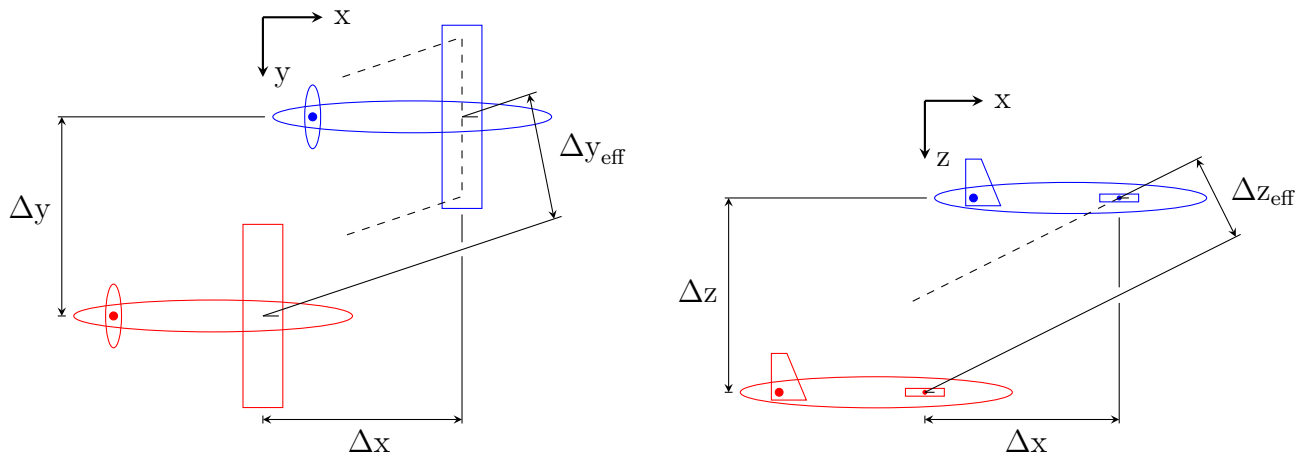

(a) Top-down view, x-y plane

(b) Side view, x-z plane

Figure 2.4: Axis systems for instantaneous and effective separations

Note however, that the induced forces and moments do not directly relate to the physical separation between the leading and trailing airliners. Rather, it depends on the trailing airliner's position inside the wake vortices generated by the leading airliner. By including the effect of wind gusts or turbulence in the calculations of the effective separations, the wind axes of the leading airliner are effectively used to coordinate the relative separations.

It is assumed that the wake vortices remain static in their position at the point they were generated in clean, non-turbulent air. In the presence of turbulence, the wake vortices are displaced based on the velocity vector of the generated turbulence at each point in the turbulence field. The vortex can thus be seen as constituting of infinitesimally small particles along its length. The assumption is then that, in the presence of a static turbulence field, each particle experiences a constant, induced velocity as given by its position in the static turbulence field. By the time the trailing airliner reaches the particle, it has been displaced by the turbulence. The displacement distance is determined by the turbulence velocity at that point in the turbulence field, and the time it took for the trailing airliner to reach the particle after it had been generated by the leading airliner. This is not accurate for large longitudinal separations, or for formations that are banking or changing flight path angle.

The result of this is that the effective lateral and vertical separations change according to the turbulence field, and are no longer the same as the instantaneous separations, as illustrated in Fig. 2.4. The dashed lines of Fig. 2.4 indicate the direction of the wake vortices due to the displacement by gusts of wind. The effective separation thus changes as a function of the gust velocities v_g and w_g, the free stream velocity V, and the geometric separation [3]. Assuming small induced angles, $\frac{v_g}{V}$ and $\frac{w_g}{V}$, the effective vertical and lateral separation are then respectively given by,

$$\begin{aligned} \eta_{eff} &= \sqrt{\xi^2+\eta^2}\sin\left(\tan^{-1}\left(\frac{\eta}{\xi}\right)-\frac{v_g}{V}\right) \\ &\approx \eta-\xi\left(\frac{v_g}{V}\right) \end{aligned} \tag{2.1}$$

and

$$\begin{aligned} \zeta_{eff} &= \sqrt{\xi^2+\zeta^2}\sin\left(\tan^{-1}\left(\frac{\zeta}{\xi}\right)-\frac{w_g}{V}\right) \\ &\approx \zeta-\xi\left(\frac{w_g}{V}\right). \end{aligned} \tag{2.2}$$

2.2 Airliner Motion Model

The airliner is modelled as a six degree of freedom (6-DOF) rigid body. These consist of the 3 translational and 3 rotational degrees of freedom. A rigid body implies that every element of mass in the airliner's body remains fixed relative to each other, though in reality, airliners have flexible structures. These modes of motion are assumed to fall outside the bandwidth of the controllers in this thesis, and will thus not be taken into account during the modelling process. This assumption however, will need to be revisited in future work.

Kinetics is the branch of mechanics that relate to the forces and moments acting upon an object. These forces and moments affect the object's kinematic state, which includes its position, velocity and acceleration. A simple kinetics model based on Newton's laws of motion for 6-DOF rigid bodies, will be used to describe the kinetics of the airliner. This model is presented in Eq. 2.3, with all vectors coordinated in body axes. The various cross product terms arise due to the Coriolis effect, which is due to the coordination of the model in body axes, as opposed to inertial axes.

$$\begin{aligned} X &= m\left(\dot{U}-VR+WQ\right) & L &= \dot{P}I_{xx}+QR\left(I_{zz}-I_{yy}\right) \\ Y &= m\left(\dot{V}+UR-WP\right) & M &= \dot{Q}I_{yy}+PR\left(I_{xx}-I_{zz}\right) \\ Z &= m\left(\dot{W}-UQ+VP\right) & N &= \dot{R}I_{zz}+PQ\left(I_{yy}-I_{xx}\right) \end{aligned} \tag{2.3}$$

This model makes the assumption that the cross products of inertia are negligibly small.

2.3 Force and Moment Models

The forces and moments acting upon the conventional and formation-flying airliners will be investigated. For the conventional airliner, the relevant models that will be developed are the aerodynamic, gravitational and thrust models. These models generate all the significant forces and moments for the airliner in isolated flight, assuming clear, non-turbulent air. The summation of these forces and moments in Eqs. 2.4, are applied to the 6-degree of freedom model to drive the mechanics of the airliner.

$$\begin{aligned} X &= X^A + X^T + X^G & L &= L^A + L^T + L^G \\ Y &= Y^A + Y^T + Y^G & M &= M^A + M^T + M^G\,, \\ Z &= Z^A + Z^T + Z^G & N &= N^A + N^T + N^G \end{aligned} \tag{2.4}$$

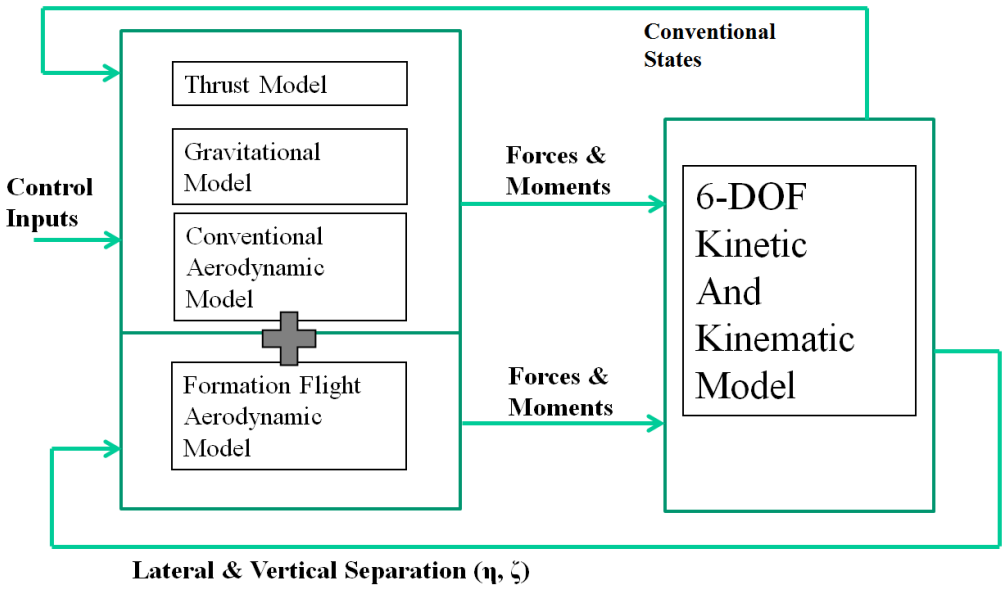

Figure 2.5: Trailing airliner mechanics overview

The trailing airliner in formation flight experiences additional induced aerodynamic forces and moments, due to the interactions with the leading airliner's wake vortices. These are encapsulated into a model that can be superimposed with the conventional aerodynamics model, as illustrated in Fig 2.5.

2.3.1 Gravitational and Thrust Models

2.3.1.1 Gravitational Model

The components for the gravitational force in body axes are adequately modelled, with the gravitational acceleration vector downwards in inertial axes, as:

$$\begin{bmatrix} X^G \\ Y^G \\ Z^G \end{bmatrix} = \begin{bmatrix} -\sin\Theta \\ \cos\Theta\sin\Phi \\ \cos\Theta\cos\Phi \end{bmatrix} mg. \tag{2.5}$$

Because the airliner's centre of gravity coincides with its centre of mass due to the assumed uniformity of the gravitational field, no moment is produced, as is intuitively expected.

2.3.1.2 Thrust Model

A simplistic, first order thrust model was developed. It assumes a single force applied to the centre of mass of the airliner, perfectly aligned with the x-body-axis, and is described by:

$$\dot{T} = -\frac{1}{\tau}T + \frac{1}{\tau}T_c, \tag{2.6}$$

where T is the time-dependant thrust magnitude, and T_c is the thrust command. The forces and moments, decomposed to their equivalent body-axes components are, $X^T = T$, and the remaining forces and moments are all zero.

It may be necessary to develop a more complex engine model during future research, as the simplifying assumptions made here neglect effects that could potentially have a significant effect on the control and fuel performance of the airliner. In particular, the thrust of the engines may be vertically offset from the centre of mass, which could induce pitching moments. Dynamic throttling of the engines would then introduce additional pitching dynamics, which could affect altitude regulation and passenger comfort.

Furthermore, the dynamic throttling would be of concern for the trailing airliner, as it will try to regulate its in-track position behind the leading airliner. This is further complicated by the wake interactions and turbulence. It is thus necessary to develop a more complex model which accounts for these factors, to allow for greater confidence in the formation flight model and the results it produces.

The typical engine model contains slew rates and time delays. The slew rates have not been included in this model, though this assumption should not have a significant effect, as the throttling

is small in steady, trimmed flight. Furthermore, the time delay should be sufficiently approximated by the first order model included in the full non-linear simulation model.

2.3.2 Conventional Aerodynamic Model

The conventional model for the airliner in isolated flight, given by Eqs. 2.8, is based on standard derivations commonly encountered in literature [27–29]. It uses linearised stability and control derivatives to describe normalised aerodynamic force and moment coefficients. The notation of the control and stability derivatives uses the following format,

$$C_{A_B} = n\frac{\partial \hat{C}_A}{\partial B}, \tag{2.7}$$

where C_A is the aerodynamic coefficient affected by the state or input variable B, and n is the optional normalising coefficient associated with B. The term "control derivatives" refers to the aerodynamic coefficient derivatives by an input matrix variable, whereas the term "stability derivatives" refers to the aerodynamic derivatives by a state variable. Furthermore, the hat notation on the coefficients indicate that the coefficient deals with the conventional airliner in isolated flight. The derivatives do not require the hat notation, as they are independent of the formation flight interactions. This will become clear in the aerodynamic interaction model discussion in the subsequent section. Lastly note that as the aerodynamics are linearised about a trim, it is only safe to assume that the model is accurate near the trim.

$$\begin{aligned}
\hat{C}_D &= C_{D_t} + C_{D_\alpha}(\alpha - \hat{\alpha}_t) + C_{D_M}\frac{\overline{V} - \overline{V}_t}{\overline{V}_s} \\
\hat{C}_L &= C_{L_t} + C_{L_\alpha}(\alpha - \hat{\alpha}_t) + C_{L_M}\frac{\overline{V} - \overline{V}_t}{\overline{V}_s} + C_{L_{\dot{\alpha}}}\dot{\alpha} + \frac{\bar{c}}{2\overline{V}_t}C_{L_q}q + C_{L_{\delta_e}}\left(\delta_e - \hat{\delta_{e_t}}\right) \\
\hat{C}_Y &= C_{Y_\beta}\beta + \frac{b}{2\overline{V}_t}C_{Y_p}p + \frac{b}{2\overline{V}_t}C_{Y_r}r + C_{Y_{\delta_a}}\delta_a + C_{Y_{\delta_r}}\delta_r \\
\hat{C}_l &= C_{l_\beta}\beta + \frac{b}{2\overline{V}_t}C_{l_p}p + \frac{b}{2\overline{V}_t}C_{l_r}r + C_{l_{\delta_a}}\delta_a + C_{l_{\delta_r}}\delta_r \\
\hat{C}_m &= C_{m_t} + C_{m_\alpha}(\alpha - \hat{\alpha}_t) + C_{m_{\dot{\alpha}}}\dot{\alpha} + C_{m_M}\frac{\overline{V} - \overline{V}_t}{\overline{V}_s} + \frac{\bar{c}}{2\overline{V}_t}C_{m_q}q + C_{m_{\delta_e}}\left(\delta_e - \hat{\delta_{e_t}}\right) \\
\hat{C}_n &= C_{n_\beta}\beta + \frac{b}{2\overline{V}_t}C_{n_p}p + \frac{b}{2\overline{V}_t}C_{n_r}r + C_{n_{\delta_a}}\delta_a + C_{n_{\delta_r}}\delta_r \\
\hat{C}_X &= -\hat{C}_D\cos\alpha + \hat{C}_L\sin\alpha \\
\hat{C}_Z &= -\hat{C}_L\cos\alpha - \hat{C}_D\sin\alpha
\end{aligned} \tag{2.8}$$

The typical model includes coefficients C_{L_0}, C_{m_0} and C_{D_0}, which are the the static lift, static pitching moment and parasitic drag coefficients respectively. Unfortunately, none of these coefficients are available from Heffley and Jewel [24], which is the source that was used to construct this model. Instead, the trim lift and drag coefficients, C_{L_t} and C_{D_t} were supplied. The trim pitching moment coefficient C_{m_t} is of course 0, as the airliner should not pitch during trim flight.

This requires knowledge of the trim angle of attack and elevator deflection values. The trim angle of attack is available in Heffley and Jewel [24], though the trim elevator deflection is not. This issue will be addressed in Section 3.1, where the trim values are calculated. Further note that the hat notation, indicating that the parameter applies to the conventional airliner, also applies to trim states and control inputs, such as angle of attack and elevator deflection.

From the aerodynamic coefficients in Eqs. 2.8, the induced aerodynamic forces and moments, decomposed to their body-axes equivalents, can be calculated as follows:

$$\begin{aligned} X^A &= qSC_X & Y^A &= qSC_Y & Z^A &= qSC_Z \\ L^A &= qSbC_l & M^A &= qS\bar{c}C_m & N^A &= qSbC_n \end{aligned} \tag{2.9}$$

where,

$$q = \frac{1}{2}\rho\bar{V}^2. \tag{2.10}$$

2.3.3 Aerodynamic Interaction Model

The aerodynamic model for formation flight interactions, developed by Bizinos and Redelinghuys [3], yields incremental coefficients for expressing the induced forces and moments as functions of lateral and vertical separation. It makes the assumption that the gradients of the interaction forces and moments are negligibly small along the longitudinal axis, meaning that longitudinal separation is not a dependant variable. Instead, the functions are fixed at an in-track distance of 10 wingspans; leaving lateral and vertical separation as the only variables to these functions. Furthermore, the model assumes rectangular wings without sweep or dihedral, and that the leading and trailing airliners are of the same wingspan. The aerodynamic interaction coefficients, denoted by subscript f', are superimposed onto the conventional aerodynamic coefficients as shown in Eqs. 2.11.

$$
\begin{aligned}
C_D &= \hat{C_D} + C_{Df'} \langle \eta, \zeta \rangle & C_L &= \hat{C_l} + C_{lf'} \langle \eta, \zeta \rangle \\
C_Y &= \hat{C_L} + C_{Lf'} \langle \eta, \zeta \rangle & C_l &= \hat{C_m} + C_{mf'} \langle \eta, \zeta \rangle \\
C_m &= \hat{C_Y} + C_{Yf'} \langle \eta, \zeta \rangle & C_n &= \hat{C_n} + C_{nf'} \langle \eta, \zeta \rangle \\
C_X &= -C_D \cos\alpha + C_L \sin\alpha & C_Z &= -C_L \cos\alpha - C_D \sin\alpha
\end{aligned}
\tag{2.11}
$$

The model was developed using the single horseshoe vortex model for the approximation of the two, counter-rotating fully rolled-up trailing vortices. The horseshoe vortex consists of a bound vortex of span $b_v = \frac{\pi}{4}b$, and two trailing vortices extending to infinity. The leading airliner's wing is represented by a single horseshoe vortex, whereas the trailing airliner is represented as a horseshoe vortex on each wing, tailplane and tailfin, illustrated by Fig. 2.6.

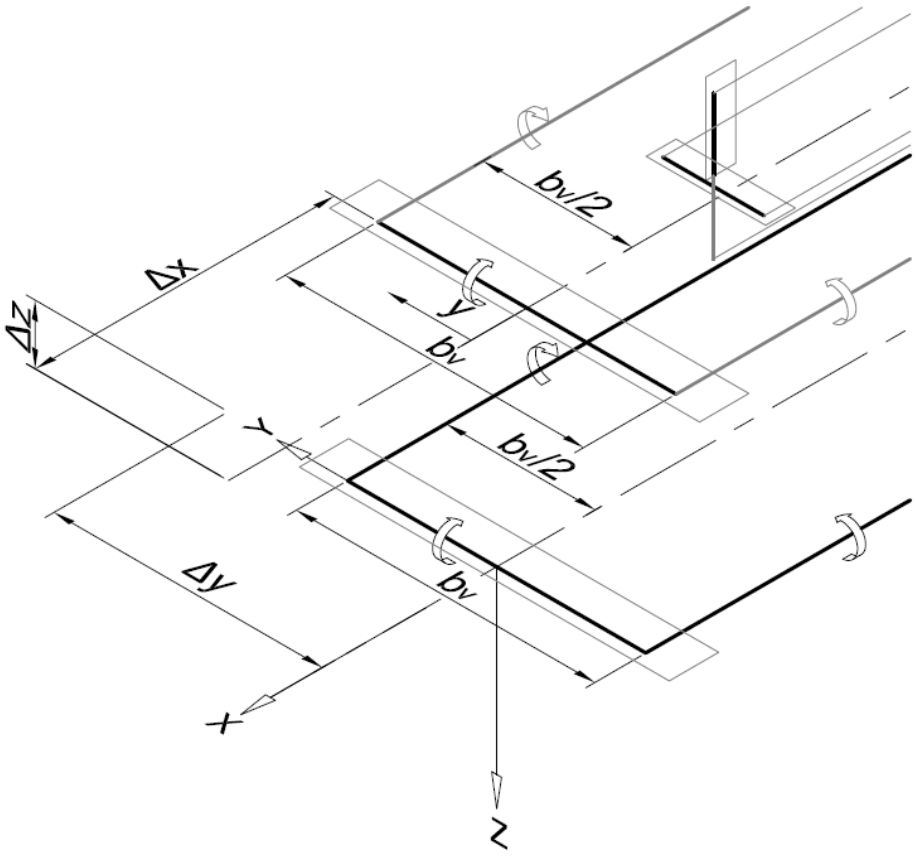

Figure 2.6: Horseshoe vortices in right echelon formation [3].

The wake vortices generated by the leading airliner induce downwash along the trailing airliner's lifting surfaces. The aerodynamic loads acting on the wing of the trailing airliner are approximated by first determining the downwash at a specific position on the wing bound vortex. For particular following regions, the downwash switches signs, and effectively becomes upwash. This upwash induces an effective angle of attack on the trailing airliner's wings, which results in increased lift, and decreased induced drag when re-trimmed.

Expressions for the incremental lift, drag, rolling moment and yawing moments are obtained by integrating along the bound vortex. It is assumed that the induced lift, drag and rolling moment are caused by the wing; induced side-force by the tailfin; and the induced yawing moment by both the wing and the tailfin. The incremental pitching moment however, is estimated by considering the change in downwash at the tailplane, due to the induced downwash at the wing. These aerodynamic loads are then converted to coefficients, which yield the incremental coefficients listed in Eqs. 2.12. These coefficients are proportional to certain dimensionless parameters, that only depend on the formation geometry. These parameters are referred to as influence factors, and are listed in Eqs. 2.13. The downwash influence factor σ influences the lift, drag, side-force and yawing moment; and the moment influence factor influence the rolling and yawing moments.

$$\begin{aligned}
C_{Df'} &= \frac{2C_{L,k}C_{L,j}}{\pi^3 \mathcal{R}}\sigma_{jk} & C_{mf'} &= C_{Lf'}\left(h-h_0\right) - \bar{V}_T C_{L\omega_h f'}\left(1-\frac{d\epsilon}{d\alpha}\right) \\
C_{Lf'} &= \frac{-c_{l_\alpha}C_{L,j}}{2\pi^2 \mathcal{R}}\sigma_{jk} & C_{L\omega_h f'} &= \frac{-2a_1 C_{L,j}}{\pi^3 \mathcal{R}\eta_h}\sigma_{jk\omega_h} \\
C_{Yf'} &= \frac{S_f}{S}\frac{2C_{L,j}}{\pi \mathcal{R}\zeta_f}\sigma_{jkf} & C_{nf'} &= \frac{2C_{L,k}C_{L,j}}{\pi^3 \mathcal{R}}\tau_{jk} - \bar{V}_f\frac{2C_{L,j}}{\pi \mathcal{R}\zeta_f}\sigma_{jkf} \\
C_{lf'} &= \frac{c_{l_\alpha}C_{L,j}}{2\pi^2 \mathcal{R}}\tau_{jk}
\end{aligned} \tag{2.12}$$

The influence factors, $\sigma_{jk}, \sigma_{jkf}, \tau_{jk}$ and $\sigma_{jk\omega_h}$, of Eqs. 2.13 are highly non-linear functions of lateral and vertical separation. Furthermore, they are dependant on the following geometry-based parameters, all normalised to wingspan: μ, which is the radius of the vortex core; ζ_v, which is the tailfin root displacement above the wing; ζ_f, which is double the vortex height; and η_h, which is the tailplane span. The extreme non-linearity of the influence factors hosts potential difficulties with the trim and control systems design. The first step for the control systems design would be to linearise these equations for operation about a particular trim, and the linearisation may not be sufficiently accurate.

$$
\begin{aligned}
\sigma_{jk} &= \ln\left|\frac{\left((\eta-(\pi/4))^2+\zeta^2+\mu^2\right)\left((\eta+(\pi/4))^2+\zeta^2+\mu^2\right)}{\left(\eta^2+\zeta^2+\mu^2\right)^2}\right| \\
\sigma_{jkf} &= \ln\left|\frac{(\eta-\pi/8)^2+(\zeta+\zeta_v)^2+\mu^2}{(\eta-\pi/8)^2+(\zeta+\zeta_v-\zeta_f\pi/8)^2+\mu^2}\right| - \ln\left|\frac{(\eta+\pi/8)^2+(\zeta+\zeta_v)^2+\mu^2}{(\eta+\pi/8)^2+(\zeta+\zeta_v-\zeta_f\pi/8)^2+\mu^2}\right| \\
\tau_{jk} &= -2\sqrt{\zeta^2+\mu^2}\left[\tan^{-1}\left(\frac{\eta-\pi/4}{\sqrt{\zeta^2+\mu^2}}\right)+\tan^{-1}\left(\frac{\eta+\pi/4}{\sqrt{\zeta^2+\mu^2}}\right)-2\tan^{-1}\left(\frac{\eta}{\sqrt{\zeta^2+\mu^2}}\right)\right]\ldots \\
&\quad -\eta\ln\left|\frac{\left((\eta-\pi/4)^2+\zeta^2+\mu^2\right)\left((\eta+\pi/4)^2+\zeta^2+\mu^2\right)}{\left(\eta^2+\zeta^2+\mu^2\right)^2}\right| - \frac{\pi}{8}\ln\left|\frac{(\eta+\pi/4)^2+\zeta^2+\mu^2}{(\eta-\pi/4)^2+\zeta^2+\mu^2}\right| \\
\sigma_{jk\omega_h} &= \ln\left|\frac{\left(\zeta^2+\left(\eta-\frac{\pi}{8}-\frac{\pi}{8}\eta_h\right)^2+\mu^2\right)\left(\zeta^2+\left(\eta+\frac{\pi}{8}+\frac{\pi}{8}\eta_h\right)^2+\mu^2\right)}{\left(\zeta^2+\left(\eta-\frac{\pi}{8}+\frac{\pi}{8}\eta_h\right)^2+\mu^2\right)\left(\zeta^2+\left(\eta+\frac{\pi}{8}-\frac{\pi}{8}\eta_h\right)^2+\mu^2\right)}\right|
\end{aligned}
\tag{2.13}
$$

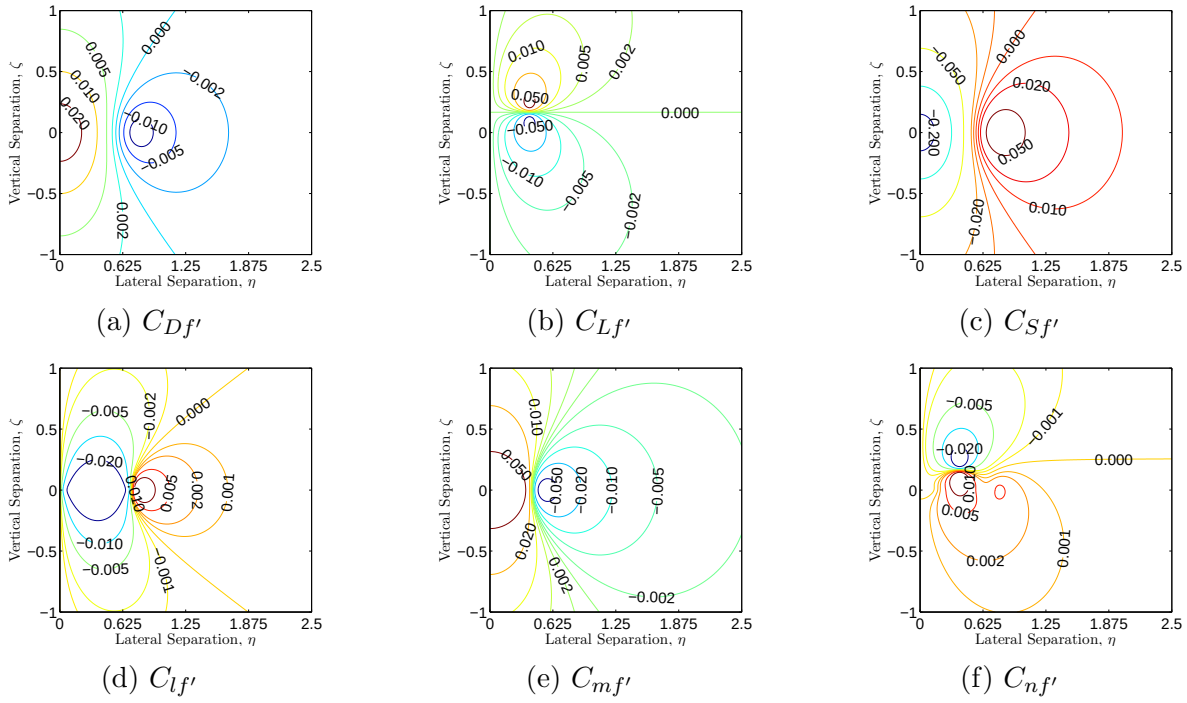

(a) $C_{Df'}$ (b) $C_{Lf'}$ (c) $C_{Sf'}$

(d) $C_{lf'}$ (e) $C_{mf'}$ (f) $C_{nf'}$

Figure 2.7: Induced force and moment contours over lateral and vertical separation

The induced forces and moments are reproduced in Fig. 2.7 as contour plots over lateral and vertical separation. From these contour plots, it can be deduced that the induced drag and lift peaks at zero vertical separation, though the same is true for the induced rolling moment. This is further discussed in Chapter 3, where it is proven that no throttle reduction benefit is found at non-zero vertical separation, compared to what is achievable at zero vertical separation.

Fig. 2.8 shows the induced forces and moments plotted as functions of lateral separation, with vertical separation fixed at 0. From these figures, it is apparent that the point of optimum drag reduction and lift increase closely corresponds to a peak in induced rolling moment. This potentially poses challenges with respect to trim and control of formation flight, and could ultimately result in formation flight not being achievable at the optimum point for fuel-consumption benefit.

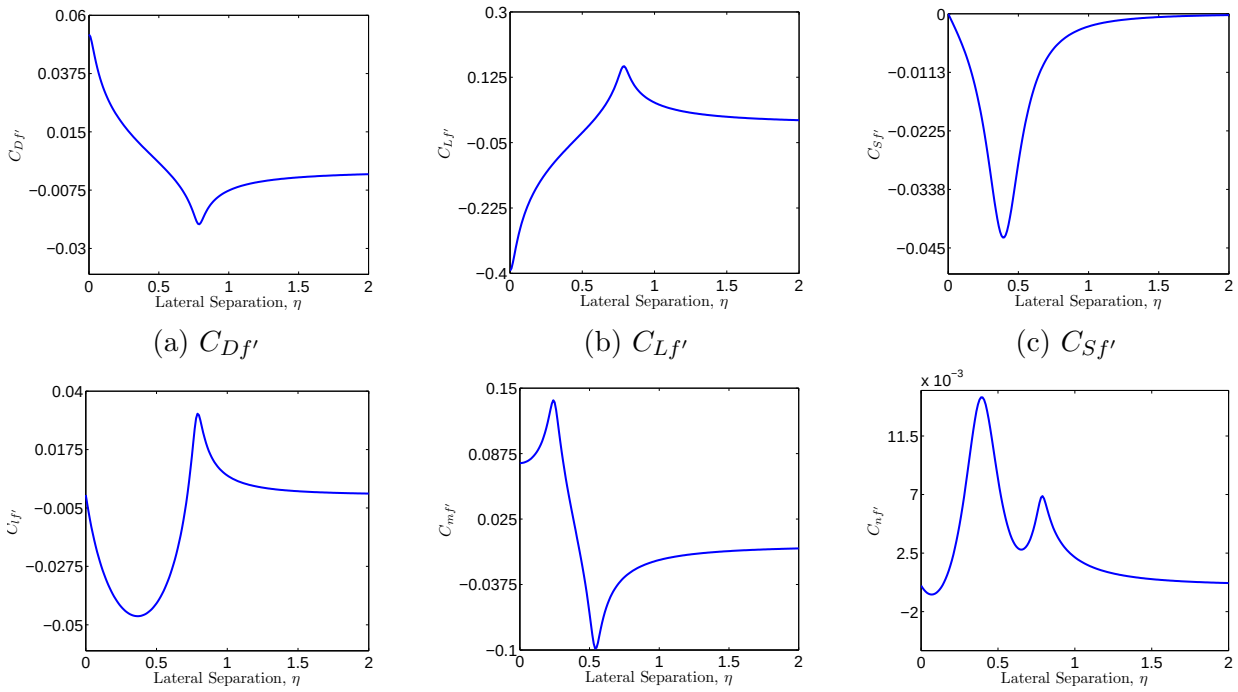

(a) $C_{Df'}$ (b) $C_{Lf'}$ (c) $C_{Sf'}$

(d) $C_{lf'}$ (e) $C_{mf'}$ (f) $C_{nf'}$

Figure 2.8: Induced force and moment coefficients as functions of lateral separation η and vertical separation $\zeta = 0$

2.4 Turbulence Model

In order to increase the fidelity of the system, a turbulence model based on the Von Kármán turbulence model was included in the Simulink model. This model was developed and packaged as a Simulink block by Cornelus le Roux of the ESL, Stellenbosch, South Africa; and is based on the mathematical representation in the Military Specification MIL-F-8785C [25] and Military Handbook MIL-HDBK-1797 [26]. A static, homogeneous and isotropic Gaussian turbulence field is assumed [30]. An aircraft flying with speed V through the static turbulence field with a spacial frequency of Ω radians per meter, will experience a circular frequency of $\omega = V \times \Omega$. The spectral forms used for the implementation are given by Eqs. 2.14.

$$
\begin{aligned}
\Phi_u(\omega) &= \frac{2\sigma_u^2 L_u}{\pi V} \cdot \frac{1}{\left(1+\left(1.339 L_u \frac{\omega}{V}\right)^2\right)^{\frac{5}{6}}} & \Phi_p(\omega) &= \frac{\sigma_w^2}{2VL_w} \cdot \frac{0.8\left(\frac{2\pi L_w}{4b}\right)^{\frac{1}{3}}}{1+\left(\frac{4b\omega}{\pi V}\right)^2} \\
\Phi_v(\omega) &= \frac{2\sigma_v^2 L_v}{\pi V} \cdot \frac{1+\frac{8}{3}\left(2.678 L_v \frac{\omega}{V}\right)^2}{\left(1+\left(2.678 L_v \frac{\omega}{V}\right)^2\right)^{\frac{11}{6}}} & \Phi_q(\omega) &= \frac{\left(\frac{\omega}{V}\right)^2}{1+\left(\frac{4b\omega}{\pi V}\right)^2} \cdot \Phi_w(\omega) \\
\Phi_w(\omega) &= \frac{2\sigma_w^2 L_w}{\pi V} \cdot \frac{1+\frac{8}{3}\left(2.678 L_w \frac{\omega}{V}\right)^2}{\left(1+\left(2.678 L_w \frac{\omega}{V}\right)^2\right)^{\frac{11}{8}}} & \Phi_r(\omega) &= -\frac{\left(\frac{\omega}{V}\right)^2}{1+\left(\frac{3b\omega}{\pi V}\right)^2} \cdot \Phi_v(\omega)
\end{aligned}
\tag{2.14}
$$

In Eqs. 2.14, the σ values correspond to the turbulence intensities and L values are the turbulence length scales. The spectral equations with subscripts u, v and w relate to turbulence velocities in the body axes of the airliner; whereas spectral equations with subscripts p, q and r relate to angular velocities. The length scales are prescribed as $L_u = 2L_v = 2L_w = 2500ft$ by MIL-F-8785C, indicating that the wavelengths are large compared to the typical airliner. The vertical and lateral separations between the leading and trailing airliners are also considered small compared to the length scales. The longitudinal separation however, is not small compared to the dominant wavelengths, which implies that time lags need to be introduced. The trailing airliner will thus experience the same turbulence as the leading airliner, but delayed in time by τ_d. The time delay τ_d is related to the in-track distance and airspeed, and is approximated by,

$$\tau_d = \frac{\xi b}{V_t}. \tag{2.15}$$

As a measure to limit the divergence of this assumption, the longitudinal separation is limited to 10 wingspans.

The turbulence intensities σ, are obtained from a lookup table, illustrated in Fig. 2.9. The contours are categorically defined under turbulence severities, ranging from light (left) to severe turbulence (right). The contours are defined, from left to right, as 2×10^{-1}, 10^{-1}, 10^{-2}, 10^{-3}, 10^{-4}, 10^{-5} and 10^{-6}.

In order to generate a turbulence signal with the correct characteristics, a unit variance band-limited white noise signal is passed through forming filters. The filter forms are derived from the spectral square roots of the spectrum equations. The implemented filter forms are shown in Eqs. 2.16. The Von Kármán implementation of the turbulence model accurately describes the turbulence, but only approximates the filter required to shape the noise.

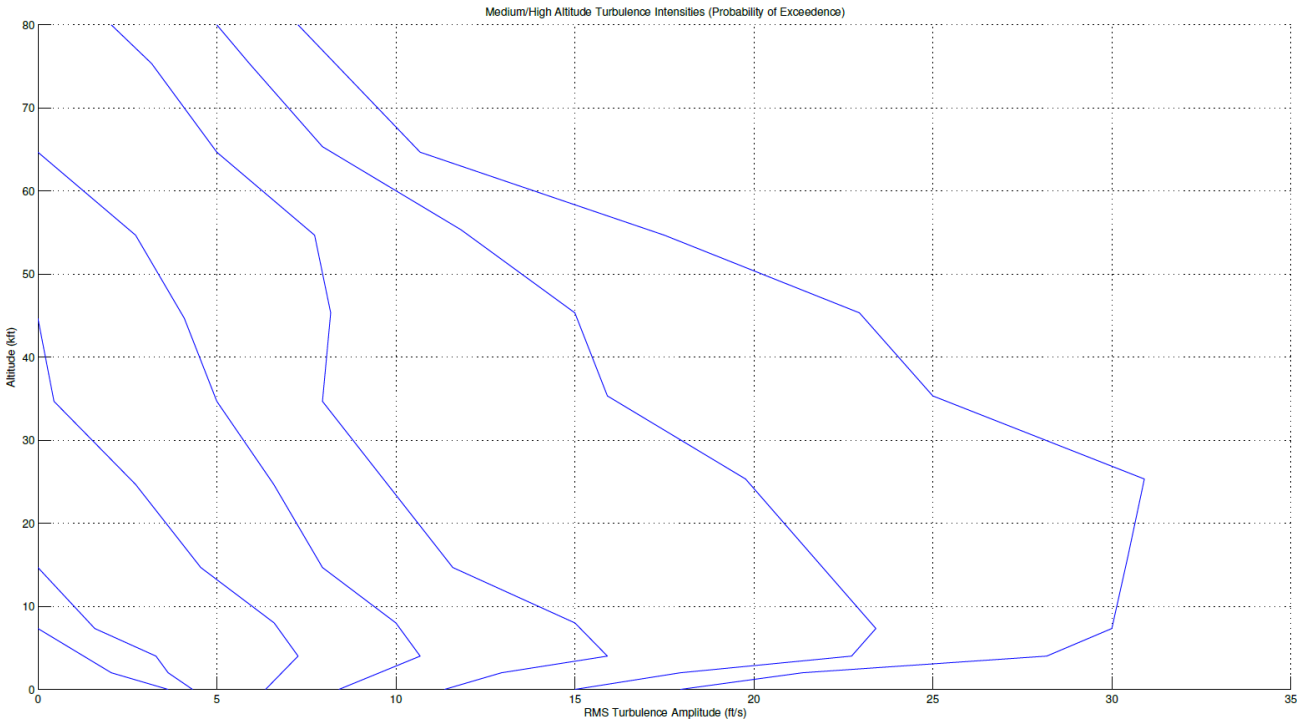

Figure 2.9: High altitude turbulence intensities lookup table

$$
\begin{aligned}
H_u(s) &= \frac{\sigma_u\sqrt{\frac{2L_u}{\pi V}}\left(1+0.25\frac{L_u}{V}s\right)}{1+1.357\frac{L_u}{V}s+0.1987\left(\frac{L_u}{V}\right)^2 s^2} \qquad & H_p(s) &= \frac{\sigma_w\sqrt{\frac{0.8}{V}}\left(\frac{\pi}{4b}\right)^{\frac{1}{6}}}{(2L_w)^{\frac{1}{3}}\left(1+\frac{4b}{\pi V}s\right)} \\
H_v(s) &= \frac{\sigma_v\sqrt{\frac{2L_v}{\pi V}}\left(1+2.7478\frac{2L_v}{V}s+0.3398\left(\frac{2L_v}{V}\right)^2 s^2\right)}{1+2.9958\frac{2L_v}{V}s+1.9754\left(\frac{2L_v}{V}\right)^2 s^2+0.1539\left(\frac{2L_v}{V}\right)^3 s^3} \qquad & H_q(s) &= \frac{\frac{s}{V}}{1+\frac{4b}{\pi V}s}\cdot H_w(s) \\
H_w(s) &= \frac{\sigma_w\sqrt{\frac{2L_w}{\pi V}}\left(1+2.7478\frac{2L_w}{V}s+0.3398\left(\frac{2L_w}{V}\right)^2 s^2\right)}{1+2.9958\frac{2L_w}{V}s+1.9754\left(\frac{2L_w}{V}\right)^2 s^2+0.1539\left(\frac{2L_w}{V}\right)^3 s^3} \qquad & H_r(s) &= \frac{-\frac{s}{V}}{1+\frac{3b}{\pi V}s}\cdot H_v(s)
\end{aligned}
\tag{2.16}
$$

2.5 Conclusion

A complete mathematical framework has been developed, describing the mechanics of the trailing and conventional airliners. This addresses research objective (1). The framework developed includes supporting axis-systems; mechanics models based on Newton's laws of motion; force and moment models for aerodynamics, thrust and gravity; a Von Kármán turbulence model; and a formation flight interaction model for the trailing airliner in formation flight. Furthermore, research

objective (5) is partially addressed, as these models have been translated to a Simulink environment. More complex analyses of the trailing airliner's trims and dynamics can subsequently be done using these flight mechanics models.

Chapter 3

Formation Flight Mechanics Analysis

An analysis of the mechanics of formation flight will characterise the behaviour of formation flight. It is a topic that has not been covered in literature extensively, and the results could likely be interesting and distinct from the results in current literature. The mechanics will first be approached from a steady-state perspective, where the trim will be calculated and analysed. The trim analysis is expected to yield interesting results regarding the aileron deflection and the throttle setting. The Bizinos model, backed up by literature, predicts that strong rolling moments exist and that potential throttle setting reductions can be expected.

Next, the mechanics will be approached from a dynamics perspective. The dynamics will be linearised, and the poles of the resulting state space representation will be plotted over ranges of lateral and vertical separation. It will determine whether formation flight is naturally stable, or whether a control system is required for stability. The dynamics of the sandwich region is expected to be particularly noteworthy, as the force and moment gradients in this region are large.

3.1 Trim Analysis

The trim analysis is done to derive conclusions about the effect of the formation flight interactions on the trailing airliner's steady state actuator settings. The calculated trim will be used as a basis for linearisation for the linear dynamics analysis, but is also important for trim or default settings of the trailing airliner's actuators for specific trailing positions in formation flight.

3.1.1 Conventional Airliner Trim Solution

The first step toward solving the trim for the trailing airliner in formation flight, is to solve the trim of the conventional airliner in isolated flight. The resulting trims are also required for the leading airliner. Certain simplifications and assumptions can be made to ease the process of finding

the trims. Firstly, it is known that the rudder and ailerons will have 0° deflection, as there are no induced rolling or yawing moments that need to be countered in trimmed, conventional flight. Furthermore, it is assumed that $\alpha_t \approx \theta_t$, where the trim angle of attack for the conventional airliner is available from Heffley and Jewel [24] .

The trim elevator deflection can then be solved for by using the equation for the trim induced aerodynamic pitching moment,

$$\hat{C_{m_t}} = C_{m_0} + C_{m_\alpha}\hat{\alpha_t} + C_{m_{\delta_E}}\hat{\delta_{E_t}} \tag{3.1}$$

As discussed in Chapter 2, the trim aerodynamic pitching moment $\hat{C_{m_t}}$ is equal to the trim pitching moment produced by the engines M^T. Consequently, $\hat{C_{m_t}} = 0$, as it was assumed that the engines produce no pitching moment. Furthermore, it is assumed that C_{m_0} is negligibly small, and is dropped from the equation. This assumption is required, as there are still too many unknowns to solve the equation. The assumption is likely valid however, as the Boeing-747 has a horisontal stabiliser which could be used to cancel this term. Nevertheless, if this assumption is incorrect, the consequence that will follow is that the trim elevator deflection will be incorrect. This will have additional implications for the trim lift, through the control derivative for lift to elevator deflection $C_{L_{\delta_e}}$. The trim elevator deflection is then given by,

$$\hat{\delta_{E_t}} = -\frac{C_{m_\alpha}\hat{\alpha_t}}{C_{m_{\delta_E}}} \tag{3.2}$$

Only the trim thrust settings still needs to be calculated. This is done by equating the force along the x_b-axis to zero, $X = 0$. This leads to the following expression,

$$T_t = \bar{q}_t S C_{Dt} \cos\alpha_t - \bar{q}_t S C_{Lt} \sin\alpha_t + mg\sin\theta_t, \tag{3.3}$$

where the only remaining unknown is the trim thrust setting, and can thus be solved.

3.1.2 Trailing Airliner Trim Solution

With a solution to the trim states and settings for isolated flight found, Eqs. 2.11 is solved taking this isolated flight trim into account. The remaining forces and moments are only due to formation flight interactions, and the additional control surface deflections required to counter these interactions. This superposition is possible due to the linearity of the model used in Eqs. 2.11, though the trim thrust setting needs to be recalculated. Eqs. 3.4 use Cramer's rule to yield a solution to the trim control surface deflections and states required to negate formation flight induced forces and moments, which will later be superimposed onto the conventional trim states and settings. Refer to Appendix B for a brief introduction to Cramer's Rule – though any alternative method

for solving systems of simultaneous equations may be used as well. Note that a 0° bank angle is maintained for the chosen trim configuration.

$$\theta_{t,f'} = \frac{\begin{vmatrix} -C_{Lf'}\langle\eta,\zeta\rangle & C_{L_{\delta_e}} \\ -C_{mf'}\langle\eta,\zeta\rangle & C_{m_{\delta_e}} \end{vmatrix}}{\begin{vmatrix} C_{L_\alpha} & C_{L_{\delta_e}} \\ C_{m_\alpha} & C_{m_{\delta_e}} \end{vmatrix}} \quad \delta_{e_{t,f'}} = \frac{\begin{vmatrix} C_{L_\alpha} & -C_{Lf'}\langle\eta,\zeta\rangle \\ C_{m_\alpha} & -C_{mf'}\langle\eta,\zeta\rangle \end{vmatrix}}{\begin{vmatrix} C_{L_\alpha} & C_{L_{\delta_e}} \\ C_{m_\alpha} & C_{m_{\delta_e}} \end{vmatrix}} \quad \psi_{t,f'} = \frac{\begin{vmatrix} -C_{Yf'}\langle\eta,\zeta\rangle & C_{Y_{\delta_a}} & C_{Y_{\delta_r}} \\ -C_{lf'}\langle\eta,\zeta\rangle & C_{l_{\delta_a}} & C_{l_{\delta_r}} \\ -C_{nf'}\langle\eta,\zeta\rangle & C_{n_{\delta_a}} & C_{n_{\delta_r}} \end{vmatrix}}{\begin{vmatrix} -C_{Y_\beta} & C_{Y_{\delta_a}} & C_{Y_{\delta_r}} \\ -C_{l_\beta} & C_{l_{\delta_a}} & C_{l_{\delta_r}} \\ -C_{n_\beta} & C_{n_{\delta_a}} & C_{n_{\delta_r}} \end{vmatrix}}$$

$$\delta_{a_{t,f'}} = \frac{\begin{vmatrix} -C_{Y_\beta} & -C_{Yf'}\langle\eta,\zeta\rangle & C_{Y_{\delta_r}} \\ -C_{l_\beta} & -C_{lf'}\langle\eta,\zeta\rangle & C_{l_{\delta_r}} \\ -C_{n_\beta} & -C_{nf'}\langle\eta,\zeta\rangle & C_{n_{\delta_r}} \end{vmatrix}}{\begin{vmatrix} -C_{Y_\beta} & C_{Y_{\delta_a}} & C_{Y_{\delta_r}} \\ -C_{l_\beta} & C_{l_{\delta_a}} & C_{l_{\delta_r}} \\ -C_{n_\beta} & C_{n_{\delta_a}} & C_{n_{\delta_r}} \end{vmatrix}} \quad \delta_{r_{t,f'}} = \frac{\begin{vmatrix} -C_{Y_\beta} & C_{Y_{\delta_a}} & -C_{Yf'}\langle\eta,\zeta\rangle \\ -C_{l_\beta} & C_{l_{\delta_a}} & -C_{lf'}\langle\eta,\zeta\rangle \\ -C_{n_\beta} & C_{n_{\delta_a}} & -C_{nf'}\langle\eta,\zeta\rangle \end{vmatrix}}{\begin{vmatrix} -C_{Y_\beta} & C_{Y_{\delta_a}} & C_{Y_{\delta_r}} \\ -C_{l_\beta} & C_{l_{\delta_a}} & C_{l_{\delta_r}} \\ -C_{n_\beta} & C_{n_{\delta_a}} & C_{n_{\delta_r}} \end{vmatrix}} \tag{3.4}$$

Following the superposition of the formation flight trim onto the conventional trim, the total throttle setting is recalculated using Eq. 3.3. Fig. 3.1 shows the resulting trim actuator settings, angle of attack and sideslip angle for zero vertical separation. Note that the plot of the required aileron trim on Fig. 3.1b passes through values of nonsensically large magnitude. This is mathematically allowed by the linearity of the aerodynamics model, and is thus simply an indication that the ailerons are completely insufficient at countering the induced rolling moment at certain trailing regions.

3.1.3 Resulting Feasible Regions

Feasible regions for formation flight appear as a result of the required trim. A feasible region is defined as adhering to the following requirements: all actuators must be unsaturated and within defined limits; furthermore, the required throttle setting must be below the trim throttle setting of the conventional airliner. The consequence of exceeding maximum aileron deflection is that the trailing airliner will not be capable of countering the induced rolling moments, even at maximum aileron deflection. It will thus be forcibly banked out of the wake – or possibly, and dangerously so, deeper into the wake. The consequence of flying in a region with an increased throttle setting, is that the airliner will have greater fuel-consumption, which is undesirable.

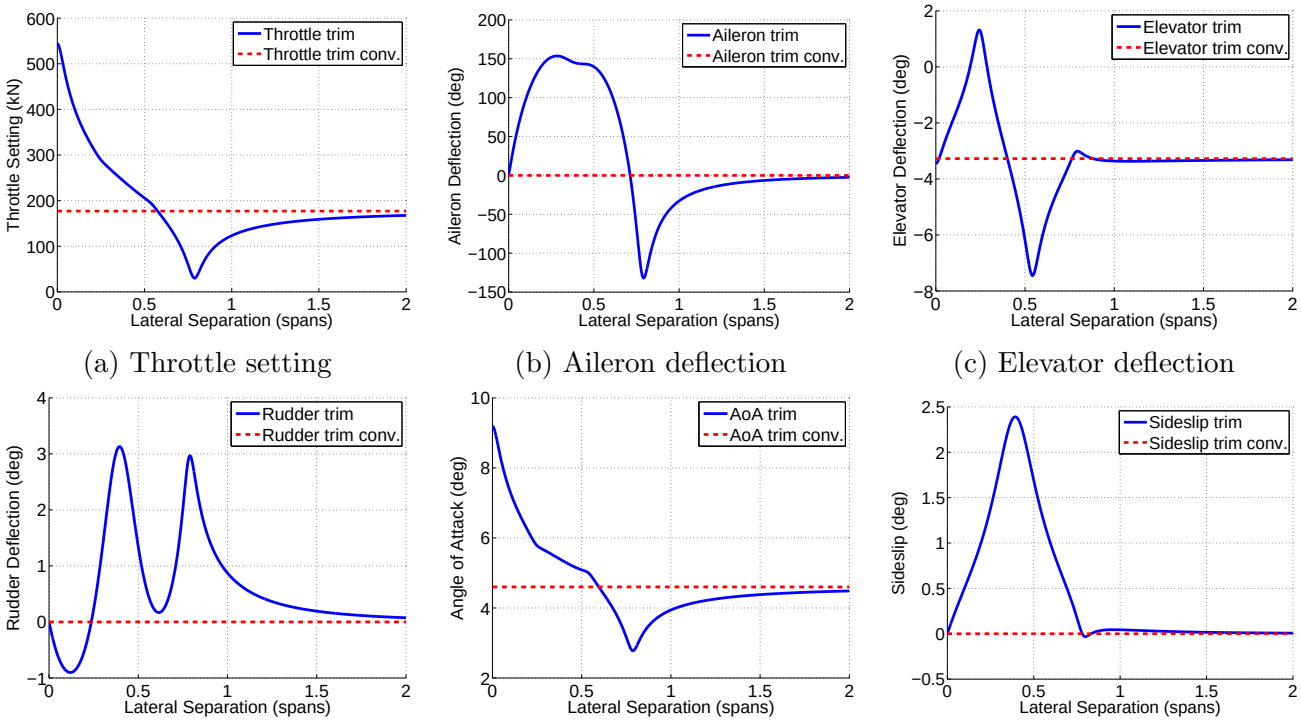

(a) Throttle setting (b) Aileron deflection (c) Elevator deflection

(d) Rudder deflection (e) Angle of attack (f) Sideslip

Figure 3.1: Trim actuators settings, angle of attack and sideslip over lateral separation.

With the knowledge that these requirements do not hold for all vertical and lateral separations, an analysis is required to determine which regions are feasible, and which are not. Fig. 3.2 shows the required trim plots for aileron deflection and throttle setting. On top of these, the maximum aileron deflections and the conventional airliner's trim throttle setting are plotted as dashed lines. From this, it can be visually deduced which regions are feasible, by identifying regions where both the aileron deflection and throttle setting trim plots are within their defined bounds.

As shown on Fig. 3.3, the analysis yields 2 trimmable, desirable regions over a lateral separation range. This result is symmetrical for positive and negative lateral separation, and only the positive half is shown. The first feasible region is situated around approximately 0.71 wingspans lateral separation in a narrow region between two untrimmable bounds – and is hence coined the "sandwich" region. The second region has only one untrimmable bound inboard at approximately 1.1 wingspans – and is coined the "outer" region.

It is noteworthy – and unfortunate – that the optimal fuel consumption location is not inside either of the feasible trim regions. Consequently, the trailing airliner cannot be trimmed at the optimal region using the current wings-level trim configuration. Trimming closer to the optimal region would require a more complex trim configuration, such as a non-zero bank angle trim; or alternatively, more powerful ailerons and accompanying structural reinforcements, designed to handle the induced rolling moments.

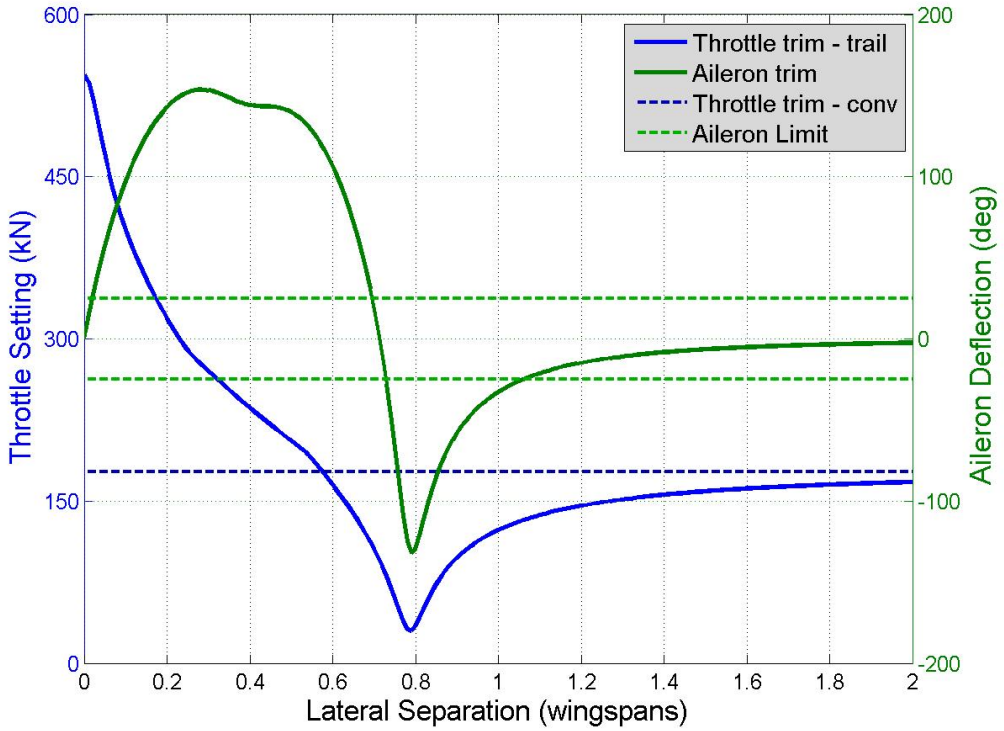

Figure 3.2: Trim comparison of aileron deflection and throttle setting over lateral separation, with constraints applied.

3.1.3.1 Sandwich Region

The sandwich region is the region with the greatest potential for fuel-consumption reduction. Theoretically, as shown on Fig. 3.3, the required throttle setting at the centre of the sandwich region is reduced by approximately 46% compared to the required throttle setting of the conventional airliner in isolated flight. This is evidently a much greater throttle setting reduction than what is achievable in the outer region. It is also possible to avoid unmodelled drag effects due to nonzero aileron deflection, as the trailing airliner can be trimmed with 0° aileron deflection in the centre of the sandwich region.

The width of the sandwich region may however make it impractical or risky to track in real atmospheric conditions. Furthermore, the region presents divergent behaviour, in that the induced rolling moments and induced rolling moment gradients in this region are always of the same sign. Thus, the trailing airliner will naturally be rolled and banked into regions with induced rolling moment of larger magnitude. As a result, any disturbance from trim will cause the trailing airliner to leave the sandwich region and enter an untrimmable zone, in the absence of a pilot or auto-pilot to intervene. This behaviour continues throughout the surrounding untrimmable zones, and it would be impossible for the airliner to recover after reaching this point.

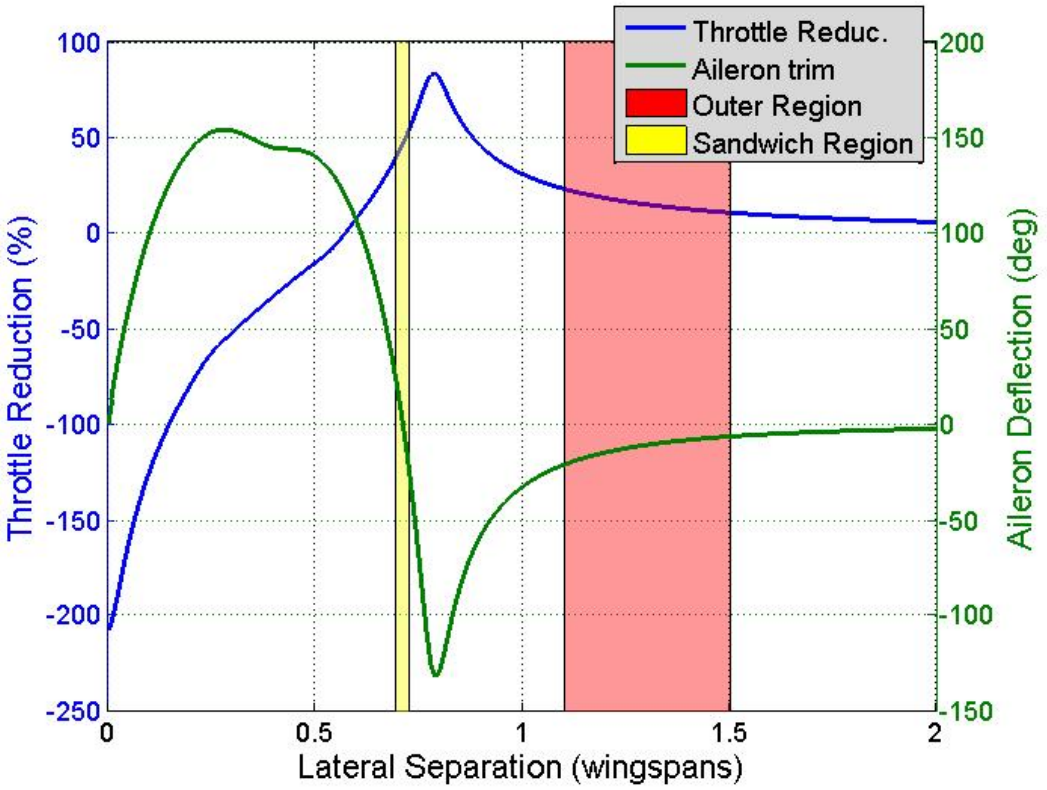

Figure 3.3: Trim comparison reveals "sandwich" region and "outer" trim regions. Throttle reduction to conventional trim given as percentage, with negative throttle reduction corresponding to an increase in throttle setting.

Additional practical complications arise when determining the initiation and break-away procedures for formation flight in the sandwich region. As the region is bounded both outboard and inboard, it is not possible to initiate the formation and enter the vortex laterally. Additionally, the initiation procedure is complicated by the large aileron deflection of approximately 32° required for trim at a vertical separation of approximately 0.4 wingspans, as indicated on Fig. 3.4b. It may be undesirable to pass through a region where such large deflections are required at trim, and therefore initiation and break-away procedures from below the wake – corresponding to positive, but decreasing vertical separation – may need to be avoided. This leaves initiation and break-away from above the wake as the only remaining option, and will require a peak aileron deflection of approximately 15°, as shown on Fig. 3.4b.

3.1.3.2 Outer Region

In the outer region, an average throttle setting reduction of approximately 14% is theoretically achievable. Though this percentage is significant, it is much less compared to the 46% achievable in

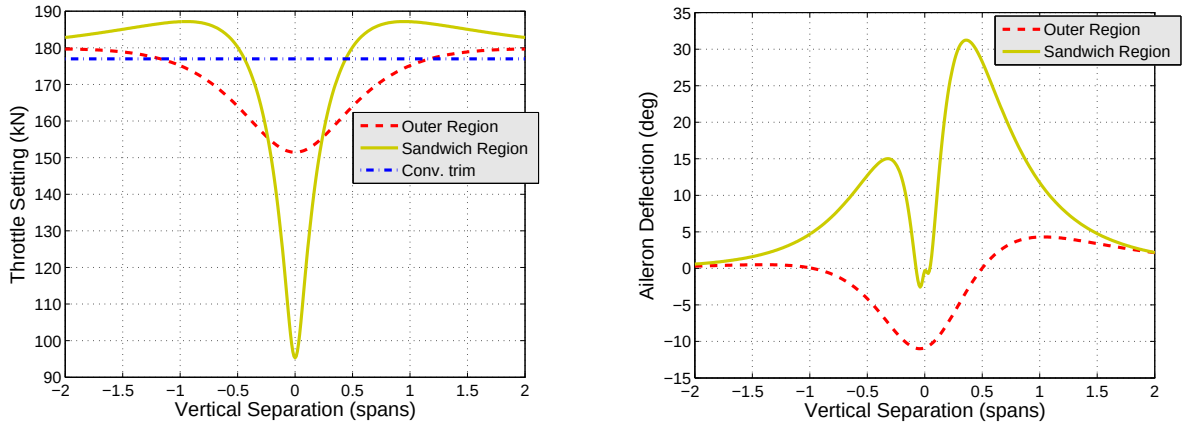

(a) Throttle trim comparison

(b) Aileron trim comparison

Figure 3.4: Trim comparison of sandwich and outer regions over vertical separation range.

the sandwich region. Furthermore, to maintain position at zero vertical separation in this region, a nonzero aileron deflection of approximately 10° is required. Thus, additional unmodelled drag effects will exist due to the trim aileron deflection, which further reduces potential savings on fuel-consumption. However, the induced rolling moment in the outer region is in the direction that would cause the airliner to bank further away from the vortex. Consequently, if the airliner entered the untrimmable region due to disturbance, the airliner would naturally bank towards the trimmable outer region, making it safer compared to the sandwich region.

It is practically feasible to consider the outer region for formation flight. Firstly, as the outer region is only bounded inboard due to excessive trim requirements, the width of the region stretches as far outboard as required, yet still tends to minimise performance degradation in terms of fuel-consumption reduction for larger separations. Consequently, the outer region is large enough to feasibly maintain formation in the presence of real atmospheric conditions and disturbances, as verified by simulations in Chapter 6. Secondly, entering the wake in the outer region would be a much simpler task than entering into the sandwich region. As there are fewer physical constraints with respect to trim in the outer region than in the sandwich region, there are more – and safer – options available for entering the wake.

3.1.3.3 Further Considerations

Fig. 3.1-3.3 show the trim settings in formation flight over ranges of lateral separation with zero vertical separation. This is due to the lift gain and drag reduction peaking at zero vertical separation. Fig. 3.4a verifies that, for both the sandwich and outer regions, the throttle reduction peaks at zero vertical separation. A peculiar result is encountered for both increasing and decreasing vertical separation values, diverging from the zero vertical separation position. The required throttle setting for both trim regions increase to values larger than the trim throttle setting for

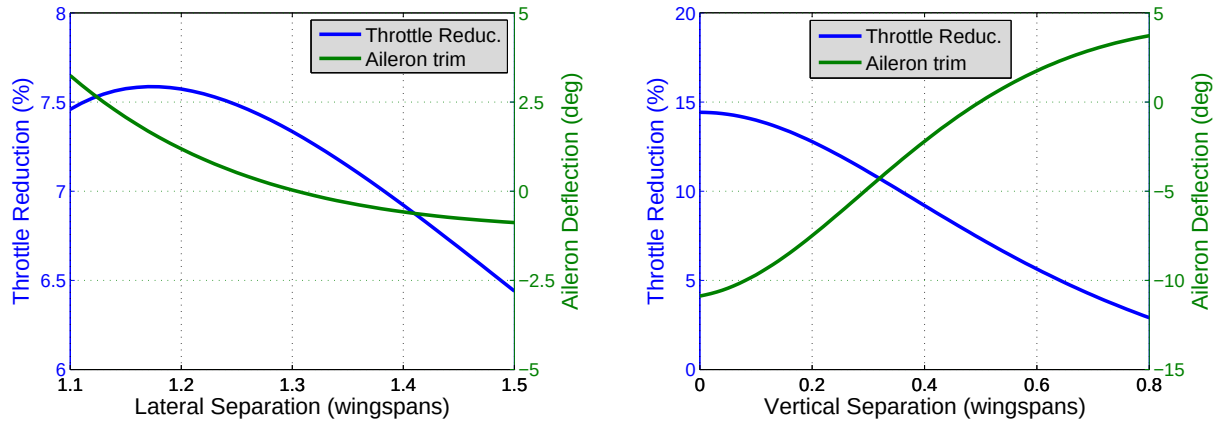

(a) Lateral separation range

(b) Vertical separation range

Figure 3.5: Aileron trim, and trim throttle reduction, measured from alternative trim position ($\eta = 1.3$, $\zeta = 0.5$)

the isolated airliner as the vertical separation magnitude increases, before eventually returning to the conventional trim setting. The effect of this is that entering the wake vertically will require more work from the airliner's engines.

When considering required aileron deflection for vertical separations, zero deflection can be achieved in the outer region at a vertical separation of 0.5 wingspans, as illustrated on Fig. 3.5b. At this position, a positive throttle setting reduction of about 7% is still achieved, resulting in a fairly good trade-off between reducing the trim aileron deflection magnitude and increasing the trim throttle setting. A similar trade-off exists for lateral separation in the outer region as well: as the trailing airliner increases lateral separation, there is a decrease in aileron deflection, but also a decrease in throttle setting. The trade-off for vertical separation however, is much better and much more efficient for fuel-consumption reduction. This efficiency benefit stems from the ratio of the gradient of the aileron setting to the throttle setting being larger over vertical separation than over lateral separation, perhaps more clearly expressed in Eq. 3.5. Note that this is only applicable for the outer region.

$$\frac{\partial}{\partial \zeta}\left(\frac{\delta_a(\eta,\zeta)}{\delta_t(\eta,\zeta)}\right) > \frac{\partial}{\partial \eta}\left(\frac{\delta_a(\eta,\zeta)}{\delta_t(\eta,\zeta)}\right) \tag{3.5}$$

Additionally, at this position ($\eta = 1.3$, $\zeta = 0.5$) in the outer region, the change in trim for both throttle setting and aileron deflection, and in fact all control surfaces, is less than the change in trim at the position of zero vertical separation.

3.2 Linear Dynamics Analysis

The linear dynamics analysis will determine the natural stability of the trailing airliner in formation flight. The approach is to first derive a linear state space representation, and then to plot the poles over ranges of lateral and vertical separation, corresponding to the trim regions defined in Sect. 3.1. However, the dynamics of the conventional airliner will first be determined, as this will be used as a benchmark for comparison with the dynamics of the trailing airliner.

3.2.1 Linearised Model for the Conventional Aircraft

A linear model for the conventional airliner in isolated flight will now be derived, based on the methodology commonly used in literature [28, 29]. The model assumes decoupling between the longitudinal and lateral states, which allows the model to be divided into separate state space representations, as follows:

$$\begin{bmatrix} \dot{\mathbf{x}}_{\text{long}} \\ \dot{\mathbf{x}}_{\text{lat}} \end{bmatrix} = \begin{bmatrix} \mathbf{A}_{\text{long}} & \mathbf{A}_{\text{long-lat}} \\ \mathbf{A}_{\text{lat-long}} & \mathbf{A}_{\text{lat}} \end{bmatrix} \begin{bmatrix} \mathbf{x}_{\text{long}} \\ \mathbf{x}_{\text{lat}} \end{bmatrix} + \begin{bmatrix} \mathbf{B}_{\text{long}} \\ \mathbf{B}_{\text{lat}} \end{bmatrix} \begin{bmatrix} \mathbf{u}_{\text{long}} & \mathbf{u}_{\text{lat}} \end{bmatrix} \tag{3.6}$$

$\mathbf{A}_{\text{long-lat}}$ and $\mathbf{A}_{\text{lat-long}}$ in Eq. 3.6 are assumed to be zero matrices. The design makes the assumption that lateral and longitudinal states are decoupled, and any coupling that exists will be handled as disturbances. Eqs. 3.7 and 3.8 show the longitudinal and lateral states for conventional flight respectively, and Eqs. 3.9 and 3.10 show the longitudinal and lateral input vectors respectively.

$$\mathbf{x}_{\text{long}} = \begin{bmatrix} \overline{V} & \alpha & q & \theta \end{bmatrix}^T \tag{3.7}$$

$$\mathbf{x}_{\text{lat}} = \begin{bmatrix} \beta & p & r & \phi \end{bmatrix}^T \tag{3.8}$$

$$\mathbf{u}_{\text{long}} = \begin{bmatrix} \delta_T & \delta_e \end{bmatrix} \tag{3.9}$$

$$\mathbf{u}_{\text{lat}} = \begin{bmatrix} \delta_a & \delta_r \end{bmatrix} \tag{3.10}$$

This state space representation is derived by constructing differential equations describing each variable in the state vector, then linearising the equation to each of the states. This will result in an $n \times n$ matrix, where the coefficients correspond to the n linearisations of each of the n differential equations. The differential equations are based on the models of Chapter 2, including the 6-DOF, aerodynamic, thrust and gravity models and are given by,

$$
\begin{aligned}
\dot{\bar{v}} &\approx \dot{U} = \frac{X}{m} + VR - WQ \\
\dot{\alpha} &\approx \frac{\dot{W}}{V_t} = \frac{1}{V_t}\left(\frac{Z}{m} + UQ - VP\right) \\
\dot{q} &= \frac{M}{I_{yy}} - PR\frac{I_{xx} - I_{zz}}{I_{yy}} \\
\dot{\theta} &= Q\cos\phi - R\sin\phi \\
\dot{\beta} &\approx \frac{\dot{V}}{\bar{V}_t} = \frac{1}{\bar{V}_t}\left(\frac{Y}{m} - UR + WP\right) \\
\dot{p} &= \frac{L}{I_{xx}} - QR\frac{I_{zz} - I_{yy}}{I_{xx}} \\
\dot{r} &= \frac{N}{I_{zz}} - PQ\frac{I_{yy} - I_{xx}}{I_{zz}} \\
\dot{\phi} &= P + Q\sin\phi\tan\theta + R\cos\phi\tan\theta
\end{aligned}
\tag{3.11}
$$

Note that all the states and inputs in this state space representation are small perturbations from the operating trim point about which the linearisation was done. Eqs. 3.12 and 3.13 show the longitudinal and lateral models, with partial derivative terms that result from the linearisation.

$$
\mathbf{A}_{\text{long}} = \begin{bmatrix}
\frac{\partial\dot{\bar{v}}}{\partial\bar{v}} & \frac{\partial\dot{\bar{v}}}{\partial\alpha} & \frac{\partial\dot{\bar{v}}}{\partial q} & \frac{\partial\dot{\bar{v}}}{\partial\theta} \\
\frac{\partial\dot{\alpha}}{\partial\bar{v}} & \frac{\partial\dot{\alpha}}{\partial\alpha} & \frac{\partial\dot{\alpha}}{\partial q} & \frac{\partial\dot{\alpha}}{\partial\theta} \\
\frac{\partial\dot{q}}{\partial\bar{v}} & \frac{\partial\dot{q}}{\partial\alpha} & \frac{\partial\dot{q}}{\partial q} & \frac{\partial\dot{q}}{\partial\theta} \\
\frac{\partial\dot{\theta}}{\partial\bar{v}} & \frac{\partial\dot{\theta}}{\partial\alpha} & \frac{\partial\dot{\theta}}{\partial q} & \frac{\partial\dot{\theta}}{\partial\theta}
\end{bmatrix}, \qquad
\mathbf{B}_{\text{long}} = \begin{bmatrix}
\frac{\partial\dot{\bar{v}}}{\partial\delta_e} & \frac{\partial\dot{\bar{v}}}{\partial\delta_T} \\
\frac{\partial\dot{\alpha}}{\partial\delta_e} & \frac{\partial\dot{\alpha}}{\partial\delta_T} \\
\frac{\partial\dot{q}}{\partial\delta_e} & \frac{\partial\dot{q}}{\partial\delta_T} \\
\frac{\partial\dot{\theta}}{\partial\delta_e} & \frac{\partial\dot{\theta}}{\partial\delta_T}
\end{bmatrix}
\tag{3.12}
$$

$$
\mathbf{A}_{\text{lat}} = \begin{bmatrix}
\frac{\partial\dot{\beta}}{\partial\beta} & \frac{\partial\dot{\beta}}{\partial p} & \frac{\partial\dot{\beta}}{\partial r} & \frac{\partial\dot{\beta}}{\partial\phi} \\
\frac{\partial\dot{p}}{\partial\beta} & \frac{\partial\dot{p}}{\partial p} & \frac{\partial\dot{p}}{\partial r} & \frac{\partial\dot{p}}{\partial\phi} \\
\frac{\partial\dot{r}}{\partial\beta} & \frac{\partial\dot{r}}{\partial p} & \frac{\partial\dot{r}}{\partial r} & \frac{\partial\dot{r}}{\partial\phi} \\
\frac{\partial\dot{\phi}}{\partial\beta} & \frac{\partial\dot{\phi}}{\partial p} & \frac{\partial\dot{\phi}}{\partial r} & \frac{\partial\dot{\phi}}{\partial\phi}
\end{bmatrix}, \qquad
\mathbf{B}_{\text{lat}} = \begin{bmatrix}
\frac{\partial\dot{\beta}}{\partial\delta_a} & \frac{\partial\dot{\beta}}{\partial\delta_r} \\
\frac{\partial\dot{p}}{\partial\delta_a} & \frac{\partial\dot{p}}{\partial\delta_r} \\
\frac{\partial\dot{r}}{\partial\delta_a} & \frac{\partial\dot{r}}{\partial\delta_r} \\
\frac{\partial\dot{\phi}}{\partial\delta_a} & \frac{\partial\dot{\phi}}{\partial\delta_r}
\end{bmatrix}
\tag{3.13}
$$

The approximate resulting partial derivatives are given by Eqs. 3.14 and 3.15. Note that some terms are left out due to assumptions and approximations that were made, such as the small angle approximation. The terms not listed are zero, or assumed to be zero.

Longitudinal State Matrix Elements

$$
\begin{aligned}
\frac{\partial \dot{\overline{v}}}{\partial \overline{v}} &= \frac{\rho \overline{V}_t S C_{X_t}}{m} + \frac{q_t S}{m V_s}\left(C_{L_M}\alpha_t - C_{D_M}\right) & \frac{\partial \dot{\overline{v}}}{\partial \alpha} &= \frac{q_t S}{m}\left(C_{L_t} + C_{L_\alpha}\alpha_t - C_{D_\alpha}\right) \\
\frac{\partial \dot{\overline{v}}}{\partial q} &= -\overline{V}_t \sin\alpha_t & \frac{\partial \dot{\overline{v}}}{\partial \theta} &= -g \\
\frac{\partial \dot{\alpha}}{\partial \overline{v}} &= -\frac{\rho S C_{Lt}}{m} - \frac{q_t S C_{L_M}}{\overline{V}_t m V_s} & \frac{\partial \dot{\alpha}}{\partial \alpha} &= -\frac{\bar{q}_t S C_{L_\alpha}}{m \overline{V}_t} \\
\frac{\partial \dot{\alpha}}{\partial q} &= 1 - \frac{\bar{q}_t S \bar{c} C_{LQ}}{2\overline{V}_t^2 m} & \frac{\partial \dot{\alpha}}{\partial \theta} &= -\frac{g}{\overline{V}_t}\sin\theta_t \\
\frac{\partial \dot{q}}{\partial \overline{v}} &= \frac{\bar{q}_t S \bar{c} C_{m_M}}{I_{yy} V_s} & \frac{\partial \dot{q}}{\partial \alpha} &= \frac{\bar{q}_t S \bar{c}}{I_{yy}} C_{m_\alpha} \\
\frac{\partial \dot{q}}{\partial q} &= \frac{\bar{q}_t S \bar{c}^2}{2 I_{yy} \overline{V}_t} C_{m_Q} & \frac{\partial \dot{\theta}}{\partial q} &= 1
\end{aligned}
\tag{3.14}
$$

The following longitudinal state matrix elements are zero: $\frac{\partial \dot{q}}{\partial \theta}, \frac{\partial \dot{\theta}}{\partial \overline{v}}, \frac{\partial \dot{\theta}}{\partial \alpha}, \frac{\partial \dot{\theta}}{\partial \theta}$

Lateral State Matrix Elements

$$
\begin{aligned}
\frac{\partial \dot{\beta}}{\partial \beta} &= \frac{\bar{q}_t S}{m \overline{V}_t}\left(C_{Y_\beta} + C_{Dt} - C_{Lt}\alpha_t\right) & \frac{\partial \dot{\beta}}{\partial p} &= \frac{\bar{q}_t S b}{2 m \overline{V}_t^2} C_{Y_P} \\
\frac{\partial \dot{\beta}}{\partial r} &= \frac{\bar{q}_t S}{m \overline{V}_t} C_{Y_R} - 1 & \frac{\partial \dot{\beta}}{\partial \phi} &= \frac{g}{\overline{V}_t}\cos\Theta_t \\
\frac{\partial \dot{p}}{\partial \beta} &= \frac{\bar{q}_t S b}{I_{xx}} C_{l_\beta} & \frac{\partial \dot{p}}{\partial p} &= \frac{\bar{q}_t S b^2}{2 I_{xx} \overline{V}_t} C_{l_P} \\
\frac{\partial \dot{p}}{\partial r} &= \frac{\bar{q}_t S b^2}{2 I_{xx} \overline{V}_t} C_{l_R} & \frac{\partial \dot{r}}{\partial \beta} &= \frac{\bar{q}_t S b}{I_{zz}} C_{n_\beta} \\
\frac{\partial \dot{r}}{\partial p} &= \frac{\bar{q}_t S b^2}{2 \overline{V}_t I_{zz}} C_{n_P} & \frac{\partial \dot{r}}{\partial r} &= \frac{\bar{q}_t S b^2}{2 \overline{V}_t I_{zz}} C_{n_R} \\
\frac{\partial \dot{\phi}}{\partial \beta} &= 1 & \frac{\partial \dot{\phi}}{\partial p} &= \tan\Theta_t
\end{aligned}
\tag{3.15}
$$

The following lateral state matrix elements are zero: $\frac{\partial \dot{p}}{\partial \phi}, \frac{\partial \dot{r}}{\partial \phi}, \frac{\partial \dot{\phi}}{\partial \beta}, \frac{\partial \dot{\phi}}{\partial \phi}$

Input Matrices

$$\mathbf{B}_{\text{long}} = \begin{bmatrix} 0 & \frac{1}{m} \\ -\frac{q_T S}{m\overline{V}_t} C_{L_{\delta_e}} & 0 \\ \frac{q_T S \bar{c}}{I_{yy}} C_{m_{\delta_e}} & 0 \\ 0 & 0 \end{bmatrix}, \qquad \mathbf{B}_{\text{lat}} = \begin{bmatrix} \frac{q_T S}{m\overline{V}_t} C_{y_{\delta_a}} & \frac{q_T S}{m\overline{V}_t} C_{y_{\delta_r}} \\ \frac{q_T S b}{I_{xx}} C_{l_{\delta_a}} & \frac{q_T S b}{I_{xx}} C_{l_{\delta_r}} \\ \frac{q_T S b}{I_{zz}} C_{n_{\delta_a}} & \frac{q_T S b}{I_{zz}} C_{n_{\delta_r}} \\ 0 & 0 \end{bmatrix} \tag{3.16}$$

Conventional Flight Mode Poles

To determine the dynamic mode poles for the conventional airliner, the actual values for the constants, and physical and aerodynamic properties for the Boeing-747 [23, 24] are substituted into the system matrices given by Eqs. 3.12 and 3.13, and the eigenvalues are calculated. This results in 2 complex pairs of longitudinal poles, namely the *phugoid* and *short-period* mode, and 2 real and a set of complex lateral poles, namely the *spiral* mode, *roll* mode and *Dutch roll* mode. The poles are listed in Table 3.1. It is noteworthy, but not unexpected, that the conventional airliner system is stable for the states of interest in isolated flight.

Longitudinal Poles		**Lateral Poles**	
Phugoid mode	$-0.0019 \pm 0.0707j$	Dutch roll mode	$-0.0705 \pm 1.006j$
Short period mode	$-0.324 \pm 0.911j$	Roll mode	-0.506
		Spiral mode	-0.0106

Table 3.1: Conventional flight mode poles

3.2.2 Linearised Model for the Trailing Airliner

Subsequent to the derivation of the model and dynamic modes for the conventional airliner, the same can be done for the trailing aircraft in a formation flight scenario. The resulting poles however, will include functions of lateral and vertical separation.

The derivation for the trailing airliner follows a similar approach as for the conventional airliner, but with additional longitudinal and lateral states. The state vectors are expanded to include η, $\dot{\eta}$ and ζ, which are lateral separation, lateral separation rate and vertical separation respectively. The lateral separation rate is required for the description of the lateral separation state. Note that the lateral separation rate is assumed to be relative to an ideal lead airliner flying a straight and level track (i.e. $V_{lead} = 0$, $\dot{V}_{lead} = 0$ and $\dot{\psi}_{lead} = 0$).

$$\mathbf{x}_{\text{long}_{f'}} = \begin{bmatrix} \mathbf{x}_{\text{long}}^T & \zeta \end{bmatrix}^T = \begin{bmatrix} \overline{V} & \alpha & q & \theta & \zeta \end{bmatrix}^T \tag{3.17}$$

$$\mathbf{x}_{\text{lat}_{f'}} = \begin{bmatrix} \mathbf{x}_{\text{lat}}^T & \dot{\eta} & \eta \end{bmatrix}^T = \begin{bmatrix} \beta & p & r & \phi & \dot{\eta} & \eta \end{bmatrix}^T \tag{3.18}$$

$$\begin{aligned} \dot{\zeta} &= -\frac{\overline{V}_t}{b} \sin(\theta - \alpha) \approx -\frac{\overline{V}_t}{b} (\theta - \alpha) \\ \dot{\psi} &= q \sin\phi \sec\theta + r \cos\phi \sec\theta \\ \ddot{\eta} &= \frac{\overline{V}_t}{b} \dot{\psi}_{trail} \approx \frac{\overline{V}_t}{b} r \sec\theta_t \end{aligned} \tag{3.19}$$

The full aerodynamic equations with aerodynamic interactions are used. The system is thus augmented to include η and ζ derivative terms. Also note that trim lift and drag terms in the conventional model need to be recalculated for the particular trim in the chosen formation scenario. There is potentially significant coupling that exists between the longitudinal and lateral states through the wake vortex interactions, as all the interaction equations are functions of lateral and vertical separation, with large gradients in both dimensions. The coupling will be investigated in following subsections.

The full state space representation for the trailing airliner is given by Eq. 3.20. For readability, the model is subdivided in longitudinal, lateral and coupling components. Note that even though coupling between lateral and longitudinal states exist through the aerodynamic interactions, any coupling that exists within the conventional model is still neglected as is done traditionally.

$$\begin{bmatrix} \dot{\mathbf{x}}_{\text{long}_{f'}} \\ \dot{\mathbf{x}}_{\text{lat}_{f'}} \end{bmatrix} = \begin{bmatrix} \mathbf{A}_{\text{long}_{f'}} & \mathbf{A}_{\text{long-lat}_{f'}} \\ \mathbf{A}_{\text{lat-long}_{f'}} & \mathbf{A}_{\text{lat}_{f'}} \end{bmatrix} \begin{bmatrix} \mathbf{x}_{\text{long}_{f'}} \\ \mathbf{x}_{\text{lat}_{f'}} \end{bmatrix} + \begin{bmatrix} \mathbf{B}_{\text{long}_{f'}} \\ \mathbf{B}_{\text{lat}_{f'}} \end{bmatrix} \begin{bmatrix} \mathbf{u}_{\text{long}} & \mathbf{u}_{\text{lat}} \end{bmatrix} \tag{3.20}$$

$$\mathbf{A}_{\text{long}_{f'}} = \begin{bmatrix} & & \frac{\partial \dot{\bar{v}}}{\partial \zeta} \\ & \mathbf{A}_{\text{long}} & \frac{\partial \dot{\alpha}}{\partial \zeta} \\ & & \frac{\partial \dot{q}}{\partial \zeta} \\ & & \frac{\partial \dot{\theta}}{\partial \zeta} \\ 0 & \frac{\bar{V}_t}{b} \; 0 \; -\frac{\bar{V}_t}{b} & 0 \end{bmatrix}, \qquad \mathbf{A}_{\text{lat}_{f'}} = \begin{bmatrix} & & \frac{\partial \dot{\beta}}{\partial \dot{\eta}} & \frac{\partial \dot{\beta}}{\partial \eta} \\ & \mathbf{A}_{\text{lat}} & \frac{\partial \dot{p}}{\partial \dot{\eta}} & \frac{\partial \dot{p}}{\partial \eta} \\ & & \frac{\partial \dot{r}}{\partial \dot{\eta}} & \frac{\partial \dot{r}}{\partial \eta} \\ & & \frac{\partial \dot{\phi}}{\partial \dot{\eta}} & \frac{\partial \dot{\phi}}{\partial \eta} \\ 0 \; 0 & \frac{\bar{V}_t}{b} \sec\theta_t \; 0 & 0 \; 0 & \\ 0 \; 0 & 0 \quad 0 & 1 \; 0 & \end{bmatrix} \tag{3.21}$$

$$\mathbf{A}_{\text{long-lat}_{f'}} = \begin{bmatrix} 0 \; 0 \; 0 \; 0 & \frac{\partial \dot{\bar{v}}}{\partial \dot{\eta}} & \frac{\partial \dot{\bar{v}}}{\partial \eta} \\ 0 \; 0 \; 0 \; 0 & \frac{\partial \dot{\alpha}}{\partial \dot{\eta}} & \frac{\partial \dot{\alpha}}{\partial \eta} \\ 0 \; 0 \; 0 \; 0 & \frac{\partial \dot{q}}{\partial \dot{\eta}} & \frac{\partial \dot{q}}{\partial \eta} \\ 0 \; 0 \; 0 \; 0 & \frac{\partial \dot{\theta}}{\partial \dot{\eta}} & \frac{\partial \dot{\theta}}{\partial \eta} \\ 0 \; 0 \; 0 \; 0 & \frac{\partial \dot{\zeta}}{\partial \dot{\eta}} & \frac{\partial \dot{\zeta}}{\partial \eta} \end{bmatrix}, \qquad \mathbf{A}_{\text{lat-long}_{f'}} = \begin{bmatrix} 0 \; 0 \; 0 \; 0 \; 0 & \frac{\partial \dot{\beta}}{\partial \zeta} \\ 0 \; 0 \; 0 \; 0 \; 0 & \frac{\partial \dot{p}}{\partial \zeta} \\ 0 \; 0 \; 0 \; 0 \; 0 & \frac{\partial \dot{r}}{\partial \zeta} \\ 0 \; 0 \; 0 \; 0 \; 0 & \frac{\partial \dot{\phi}}{\partial \zeta} \\ 0 \; 0 \; 0 \; 0 \; 0 & \frac{\partial \ddot{\eta}}{\partial \zeta} \\ 0 \; 0 \; 0 \; 0 \; 0 & \frac{\partial \dot{\eta}}{\partial \zeta} \end{bmatrix} \tag{3.22}$$

The derivatives of the influence factors σ_{jk}, σ_{jkf}, τ_{jk} and $\sigma_{jk\omega_h}$ were calculated using Matlab, and are too bulky to reasonably be presented in this thesis.

Extended Longitudinal State Matrix Elements

$$\begin{aligned} \frac{\partial \dot{\bar{v}}}{\partial \zeta} &= -\frac{\bar{q}_t S C_{L,j}}{m\pi^2 AR}\left(\frac{2C_{L,k}}{\pi} + \frac{c_{l\alpha}\alpha_t}{2}\right)\left.\frac{\partial \sigma_{j,k}}{\partial \zeta}\right|_t \\ \frac{\partial \dot{\alpha}}{\partial \zeta} &= \frac{\bar{q}_t S C_{L,j}}{m\overline{V}_t\pi^2 AR}\left(\frac{c_{l\alpha}}{2} - \frac{2C_{L,k}\alpha_t}{\pi}\right)\left.\frac{\partial \sigma_{j,k}}{\partial \zeta}\right|_t \\ \frac{\partial \dot{q}}{\partial \zeta} &= \frac{\bar{q}_t S \bar{c} C_{L,j}}{I_{yy}\pi^2 AR}\left[\frac{-c_{l\alpha}}{2}\left(\left.\frac{\partial \sigma_{j,k}}{\partial \zeta}\right|_t\right)(h-h_0) + \overline{V}_T\left(1-\frac{d\epsilon}{d\alpha}\right)\left(\frac{2a_1}{\pi\eta_h}\left.\frac{\partial \sigma_{jkw_h}}{\partial \zeta}\right|_t\right)\right] \\ \frac{\partial \dot{\theta}}{\partial \zeta} &= 0 \end{aligned} \tag{3.23}$$

Extended Lateral State Matrix Elements

$$\begin{aligned}
\frac{\partial\dot{\beta}}{\partial\eta} &= \frac{2S_f\bar{q}_tC_{L,j}}{\overline{V}_tm\pi AR\zeta_f}\left(\left.\frac{\partial\sigma_{jkf}}{\partial\eta}\right|_t\right) & \frac{\partial\dot{p}}{\partial\eta} &= \frac{\bar{q}_tSbc_{l_\alpha}C_{L,j}}{2I_{xx}\pi^2AR}\left(\left.\frac{\delta\tau_{jk}}{\delta\eta}\right|_t\right)\\
\frac{\partial\dot{r}}{\partial\eta} &= \frac{2\bar{q}_tSbC_{L,j}}{I_{zz}\pi AR}\left(\left.\frac{C_{L,k}}{\pi^2}\frac{\partial\tau_{jk}}{\partial\eta}\right|_t-\frac{\bar{V}_f}{\zeta_f}\left.\frac{\partial\sigma_{jkf}}{\partial\eta}\right|_t\right) & \frac{\partial\dot{\phi}}{\partial\eta} &= 0
\end{aligned} \tag{3.24}$$

Note: The $\dot{\eta}$ derivatives are all zero.

Coupling State Matrix Elements

$$\begin{aligned}
\frac{\partial\dot{\bar{v}}}{\partial\eta} &= -\frac{\bar{q}_tSC_{L,j}}{m\pi^2AR}\left(\frac{2C_{L,k}}{\pi}+\frac{c_{l\alpha}\alpha_t}{2}\right)\left.\frac{\partial\sigma_{j,k}}{\partial\eta}\right|_t\\
\frac{\partial\dot{\alpha}}{\partial\eta} &= \frac{\bar{q}_tSC_{L,j}}{m\overline{V}_t\pi^2AR}\left(\frac{c_{l\alpha}}{2}-\frac{2C_{L,k}\alpha_t}{\pi}\right)\left.\frac{\partial\sigma_{j,k}}{\partial\eta}\right|_t\\
\frac{\partial\dot{q}}{\partial\eta} &= \frac{\bar{q}_tS\bar{c}C_{L,j}}{I_{yy}\pi^2AR}\left[\frac{-c_{l\alpha}}{2}\left(\left.\frac{\partial\sigma_{j,k}}{\partial\eta}\right|_t\right)(h-h_0)+\overline{V}_T\left(1-\frac{d\epsilon}{d\alpha}\right)\left(\frac{2a_1}{\pi\eta_h}\left.\frac{\partial\sigma_{jkw_h}}{\partial\eta}\right|_t\right)\right]\\
\frac{\partial\dot{\beta}}{\partial\zeta} &= \frac{2S_f\bar{q}_tC_{L,j}}{\overline{V}_tm\pi AR\zeta_f}\left(\left.\frac{\partial\sigma_{jkf}}{\partial\zeta}\right|_t\right)\\
\frac{\partial\dot{p}}{\partial\zeta} &= \frac{\bar{q}_tSbc_{l_\alpha}C_{L,j}}{2I_{xx}\pi^2AR}\left(\left.\frac{\delta\tau_{jk}}{\delta\zeta}\right|_t\right)\\
\frac{\partial\dot{r}}{\partial\zeta} &= \frac{2\bar{q}_tSbC_{L,j}}{I_{zz}\pi AR}\left(\left.\frac{C_{L,k}}{\pi^2}\frac{\partial\tau_{jk}}{\partial\zeta}\right|_t-\frac{\bar{V}_f}{\zeta_f}\left.\frac{\partial\sigma_{jkf}}{\partial\zeta}\right|_t\right)
\end{aligned} \tag{3.25}$$

Note: The omitted coupling terms are zero.

Extended Input Matrices

$$\mathbf{B}_{\text{long}_f} = \begin{bmatrix}\mathbf{B}_{\text{long}}\\ 0\ \ 0\end{bmatrix}, \qquad \mathbf{B}_{\text{lat}_f} = \begin{bmatrix}\mathbf{B}_{\text{lat}}\\ 0\ \ 0\\ 0\ \ 0\end{bmatrix} \tag{3.26}$$

3.2.3 Eigenvalue Analysis

The open-loop linear model for the trailing airliner, derived in Section 3.2.2, was used to find the poles for both the sandwich and outer trim regions. The movements of these poles are plotted over ranges of lateral and longitudinal separation in the form of root loci. This is initially done for the longitudinal-lateral decoupled system, and then for the full system. Comparisons are

made between the coupled and decoupled systems, to draw conclusions about the validity of the decoupling assumption; and then between the 2 trim regions, to uncover the differences in dynamics between the trim regions.

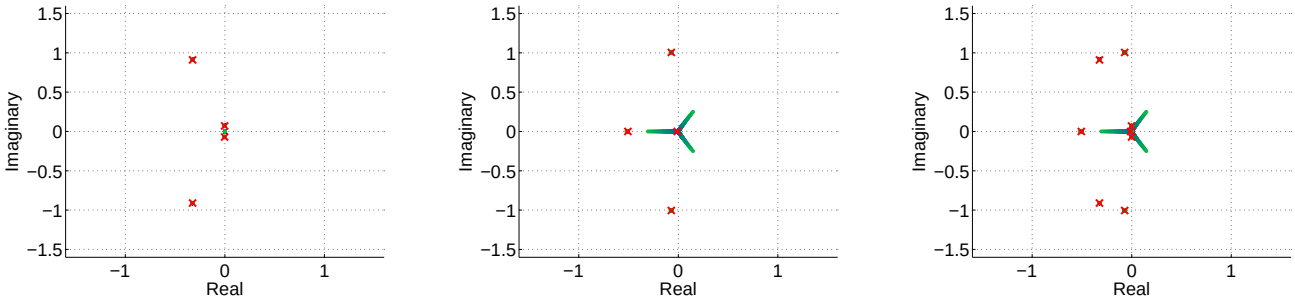

(a) Longitudinal state model (b) Lateral state model (c) Full state model

Figure 3.6: Root loci from outer trim region to conventional position for lateral separation variation.

Fig. 3.6 shows root loci of the decoupled longitudinal and lateral models, as well as the full state model. The green/blue branches indicate the movement of the poles from the outer region trim position to conventional, isolated flight. The red crosses indicate the poles for conventional isolated flight, and as expected, the branches of the loci end on these poles. It is evident from these plots that the decoupling assumption is valid for the outer region, as the superposition of the longitudinal and lateral systems yields a system very similar to the full system. Fig. 3.7 shows a similar analysis done for the sandwich region, though for a smaller range; also reaching the conclusion that the decoupling assumption is valid for this region. Note that slight differences are visible in this case, though they are relatively small.

Fig. 3.8 reveals that the conventional poles stay effectively stationary, and thus the conventional dynamics stay unchanged, for lateral and vertical separation variation within the outer region; with the exception of the spiral mode pole, which experiences an increase in speed as it approaches the roll mode pole. The pair of branches that move into the right-hand plane, seen in Figs. 3.6b and 3.6c, are due to the additional poles associated with the additional lateral separation states. Fig. 3.6a indicate that the additional pole associated with vertical separation (situated between the phugoid mode poles) stays unchanged for lateral separation variation, which is expected for the decoupled system. As there is no additional branch for this pole on Fig. 3.6c, the conclusion is that the decoupling assumption holds true.

The sandwich region is different in this regard however, as the dynamics in this region do not closely match the dynamics of conventional flight, as can be seen in Fig. 3.7. By inspecting Figs. 3.7a and 3.7b, it is possible to infer relationships between the branches and the corresponding modes, but an eigenvector analysis is required to be certain.

Figs. 3.8 and 3.9 show the lateral and vertical separation loci, for the outer and sandwich regions

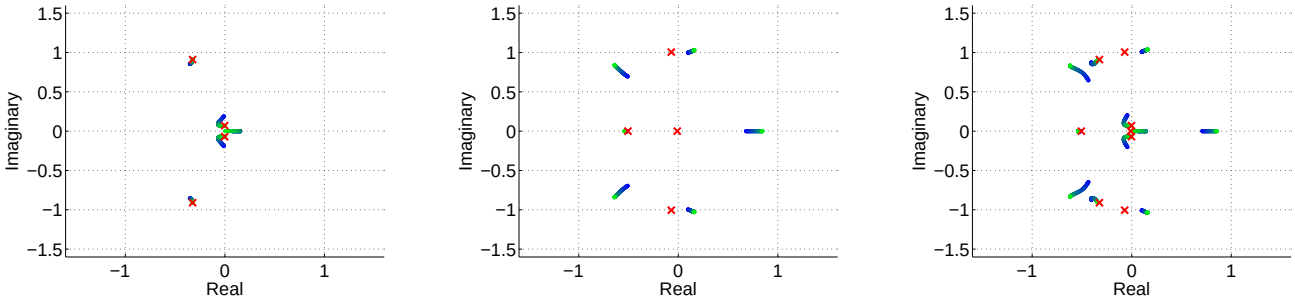

(a) Longitudinal state model (b) Lateral state model (c) Full state model

Figure 3.7: Root loci from sandwich trim region to 0.1 wingspans below this trim region for vertical separation variation.

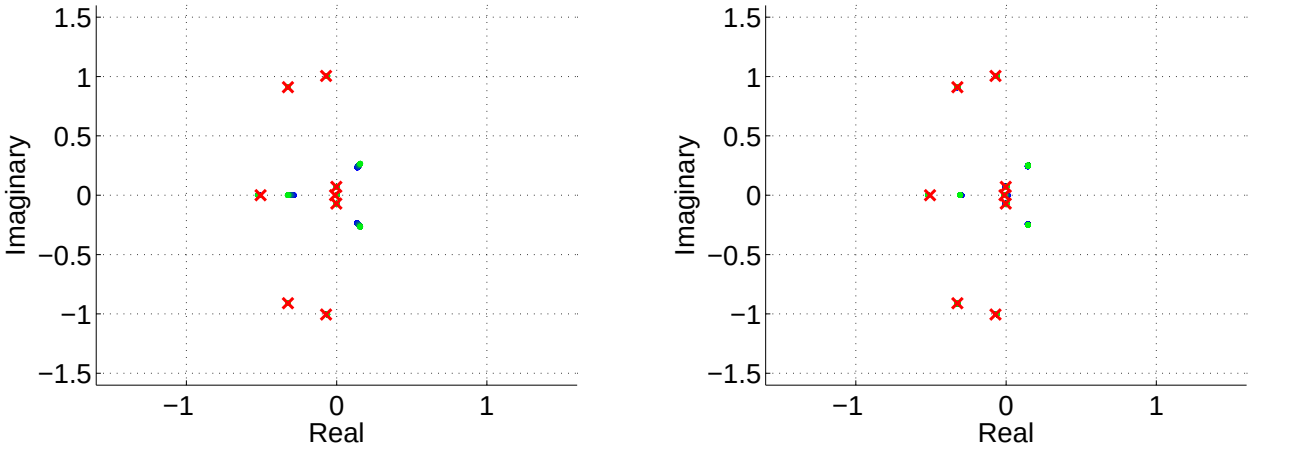

(a) Lateral separation variation ($\Delta\eta = \pm 0.05b$) (b) Vertical separation variation ($\Delta\zeta = \pm 0.05b$)

Figure 3.8: Outer region root loci ($\zeta = 0$, $\eta = 1.3$)

respectively. All cases are plotted over comparable ranges of 0.1 wingspans. Moving from smaller or more negative separation values to larger separation values, correspond to a green to blue change in colour gradient. By comparing Fig. 3.8a to Fig. 3.8b, the conclusion can be drawn that there is approximately equal change in dynamics for both lateral and vertical separation variation. A similar result is found within the sandwich region by comparing Figs. 3.9a and 3.9b. Furthermore, by comparing the loci of Fig. 3.8 to those of Fig. 3.9, it is evident that there is a much greater change in dynamics for separation variation in the sandwich region than in the outer region.

Finally, we consider the dynamics around an alternative trim position within the outer region, at half a wingspan vertical separation ($\zeta = 0.5$). This point is of interest as it corresponds to an aileron deflection of approximately 0°. Fig. 3.10 shows the loci for lateral and vertical separation about this point; just as the zero vertical separation outer region position, this region resembles isolated

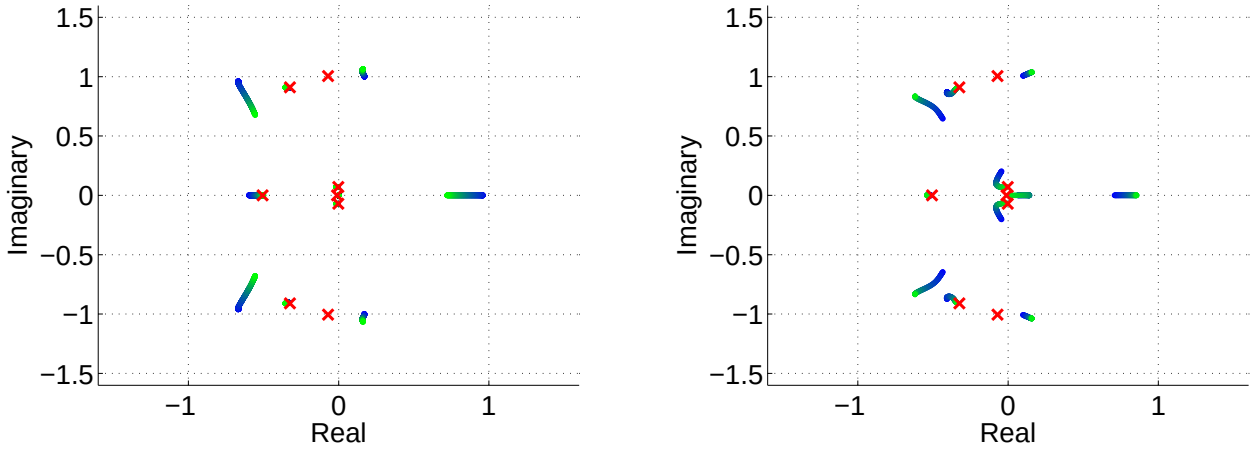

(a) Lateral separation variation ($\Delta\eta = \pm 0.05b$) (b) Vertical separation variation ($\Delta\zeta = \pm 0.05b$)

Figure 3.9: Sandwich region root loci ($\zeta = 0$, $\eta = 0.713$)

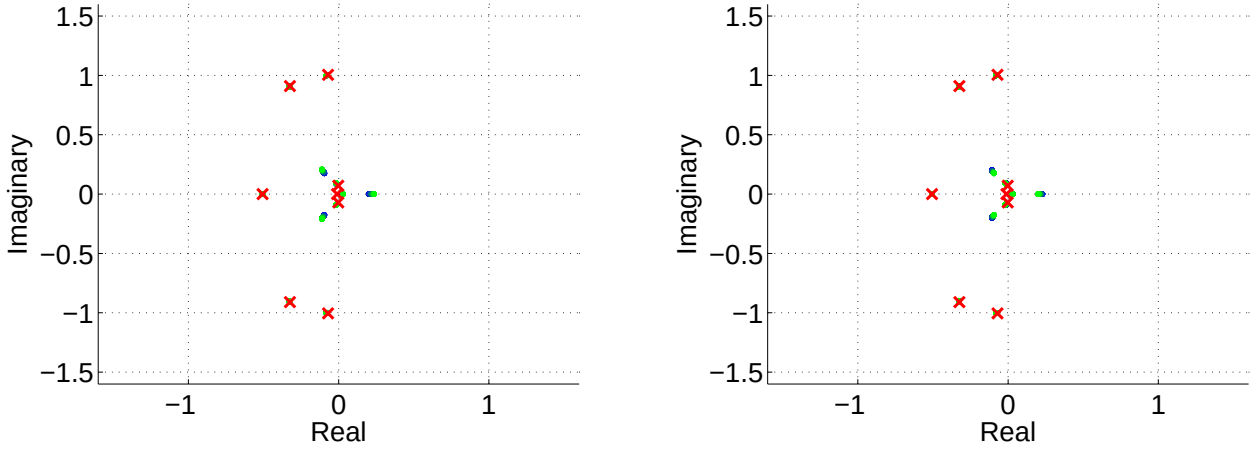

(a) Lateral separation variation ($\Delta\eta = \pm 0.05b$) (b) Vertical separation variation ($\Delta\zeta = \pm 0.05b$)

Figure 3.10: Outer region root loci; alternative trim position ($\zeta = 0.5$, $\eta = 1.3$)

flight for all modes, except for the spiral mode and the additional states' mode. Compared to the dynamics of the zero vertical separation outer region position of Fig.3.8, the interesting observation is made that the additional states' mode is now stable, whereas the spiral mode pole has become unstable.

3.2.4 Linear Model Validation

The linear model was fully cross-checked and validated against the non-linear model. The corresponding trimmed non-linear equation of each state variable derivative is varied for each relevant

state variable, over a operating range determined by non-linear simulations in turbulent conditions. The result is then superimposed on the linearisation of the non-linear equation on a plot, across the same range for the given state variable. It then becomes clear which variables are sufficiently described by the linearisation for the given trim, and which variables could potentially prove problematic or cause discrepancies between the linear and non-linear models.

This was done for the full linear model, but only the most significant comparisons to vertical and lateral separation are shown here. Note that the validation was done assuming full decoupling between longitudinal and lateral models, including the formation flight interactions.

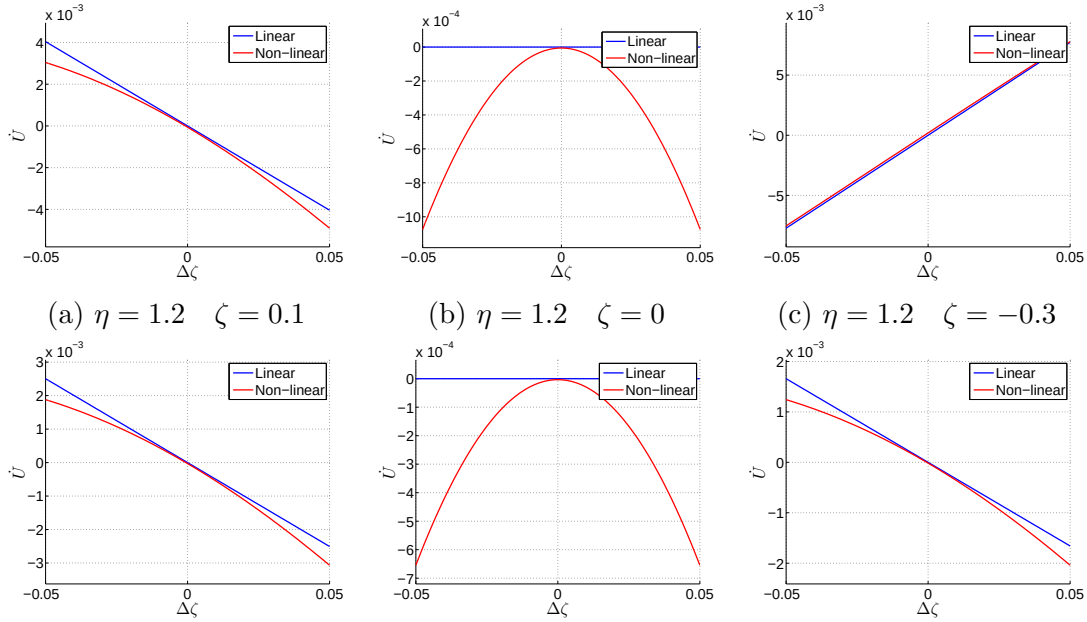

(a) $\eta = 1.2 \quad \zeta = 0.1$ (b) $\eta = 1.2 \quad \zeta = 0$ (c) $\eta = 1.2 \quad \zeta = -0.3$

(d) $\eta = 1.3 \quad \zeta = 0.1$ (e) $\eta = 1.3 \quad \zeta = 0$ (f) $\eta = 1.4 \quad \zeta = 0.1$

Figure 3.11: $\dot{U}$ linearisation validation for ζ operating range

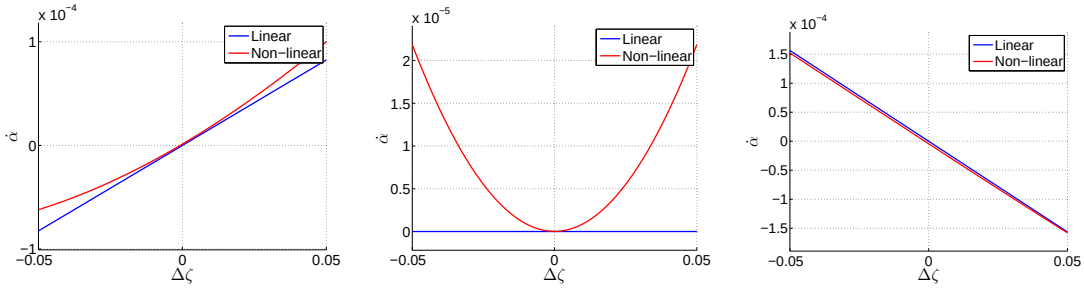

(a) $\eta = 1.2 \quad \zeta = 0.1$ (b) $\eta = 1.2 \quad \zeta = 0$ (c) $\eta = 1.2 \quad \zeta = -0.3$

(d) $\eta = 1.3 \quad \zeta = 0.1$ (e) $\eta = 1.3 \quad \zeta = 0$ (f) $\eta = 1.4 \quad \zeta = 0.1$

Figure 3.12: $\dot{\alpha}$ linearisation validation for ζ operating range

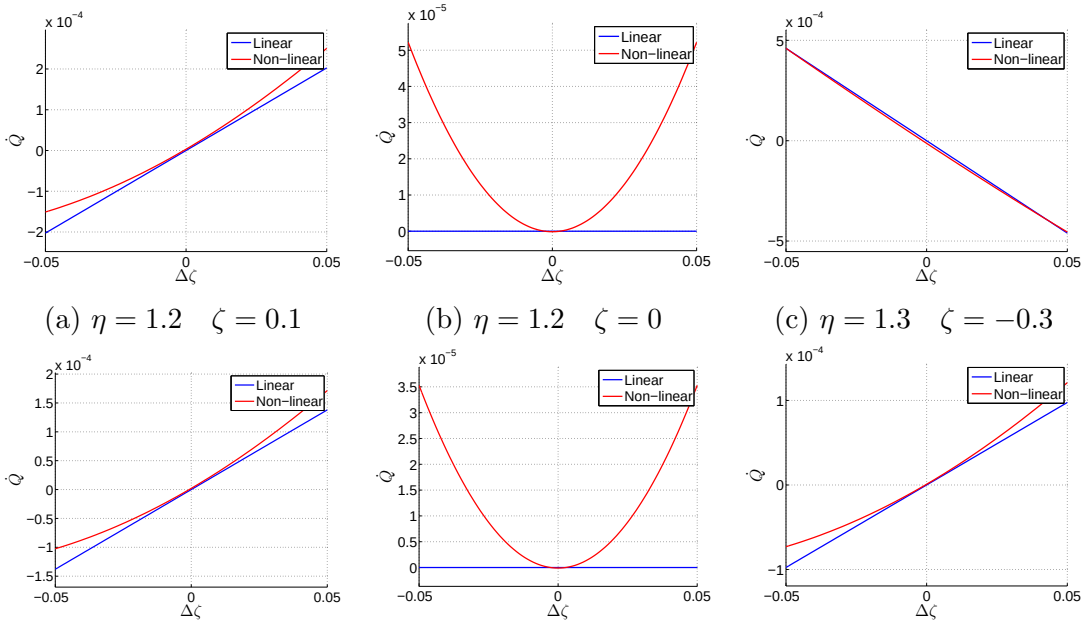

(a) $\eta = 1.2 \quad \zeta = 0.1$ (b) $\eta = 1.2 \quad \zeta = 0$ (c) $\eta = 1.3 \quad \zeta = -0.3$

(d) $\eta = 1.3 \quad \zeta = 0.1$ (e) $\eta = 1.3 \quad \zeta = 0$ (f) $\eta = 1.4 \quad \zeta = 0.1$

Figure 3.13: $\dot{Q}$ linearisation validation for ζ operating range

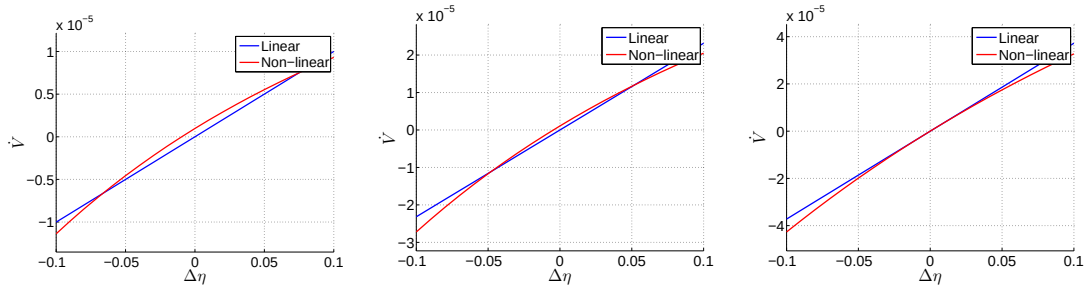

(a) $\eta = 1.2 \quad \zeta = 0.1$ (b) $\eta = 1.2 \quad \zeta = 0$ (c) $\eta = 1.3 \quad \zeta = -0.3$

(d) $\eta = 1.3 \quad \zeta = 0.1$ (e) $\eta = 1.3 \quad \zeta = 0$ (f) $\eta = 1.4 \quad \zeta = 0.1$

Figure 3.14: $\dot{V}$ linearisation validation for η operating range

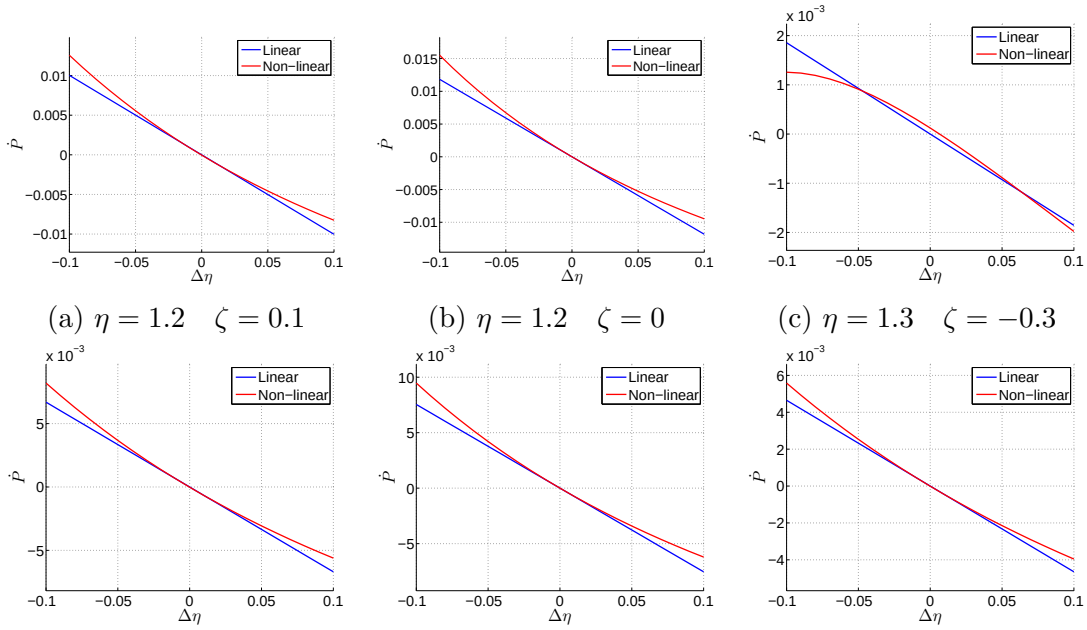

(a) $\eta = 1.2 \quad \zeta = 0.1$ (b) $\eta = 1.2 \quad \zeta = 0$ (c) $\eta = 1.3 \quad \zeta = -0.3$

(d) $\eta = 1.3 \quad \zeta = 0.1$ (e) $\eta = 1.3 \quad \zeta = 0$ (f) $\eta = 1.4 \quad \zeta = 0.1$

Figure 3.15: $\dot{P}$ linearisation validation for η operating range

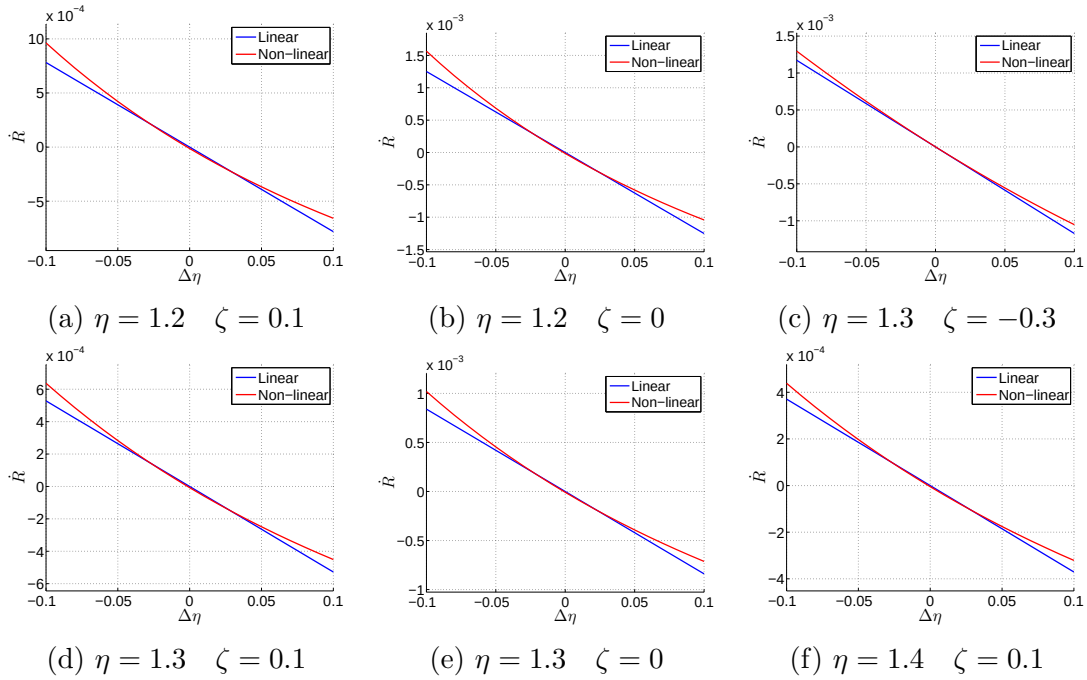

(a) $\eta = 1.2 \quad \zeta = 0.1$ (b) $\eta = 1.2 \quad \zeta = 0$ (c) $\eta = 1.3 \quad \zeta = -0.3$

(d) $\eta = 1.3 \quad \zeta = 0.1$ (e) $\eta = 1.3 \quad \zeta = 0$ (f) $\eta = 1.4 \quad \zeta = 0.1$

Figure 3.16: $\dot{R}$ linearisation validation for η operating range

The general trend of these comparisons indicate that the linearisation is valid. The apparent discrepancies on Figs. 3.11b, 3.11e, 3.12b, 3.12e, 3.13b and 3.13e are as a result of the scaling of the plots, though the actual magnitudes are small.

3.3 Conclusion

The analysis of the flight mechanics of the trailing airliner yielded a wealth of interesting information, pertaining to both trim and dynamics. The trim and dynamics analyses addresses research objectives (2) and (3) respectively. It was shown that challenges exist in trimming the trailing airliner at certain positions within the leader-generated wake vortices. In particular, the induced rolling moments on the trailing airliner, due to aerodynamic interactions with the wake vortices, are too large to be countered by the conventional airliner's ailerons – even at full deflection. Specifically, the trailing airliner is not trimmable at the optimum position for fuel-consumption reduction, as this position corresponds closely to a peak in induced rolling moment.

Two trimmable regions of benefit exist, however. The first is the sandwich region, which grants a massive fuel-consumption benefit, but large practical obstacles and risk. The second is the outer region, with lesser fuel-consumption reduction, but far greater practical feasibility and safety aspects. Trim and linear dynamics analyses revealed interesting, often contrasting, transient and steady-state behaviours for these two regions, as summarised in Table 3.2. In both the sandwich and outer regions, there is more variation in dynamics for vertical separation variation than for

lateral separation variation of the same magnitude.

Sandwich Region	**Outer Region**
Trimmable with zero aileron deflection	Aileron deflection vs fuel consumption reduction trade-off
Greater throttle setting reduction of approximately 45%	Lower throttle setting reduction of approximately 7% - 14%
Narrow trailing envelope; practically challenging	Large trailing region; practically feasible
Non-recoverable failure mode	Natural failure mode recovery
Initiation procedure complications	Simpler, standard initiation procedure
Greater change in trim for separation variation	Lesser change in trim for separation variation
Greater change in dynamics for separation variation	Lesser change in dynamics for separation variation

Table 3.2: Trim region comparison main points

The extreme non-linearity of the induced forces and moments presents challenges with the trailing airliner's dynamics varying greatly as a function of spatial separation. As discussed, this is more of a problem in the sandwich region than in the outer region, though it will also be an important consideration for large changes in trim position in the wake. The flight controllers will thus need to be robust to large variations in the system's characteristics, and should be able to initiate and exit formation without endangering the airliner.

The basis required for the design of the flight controllers for the conventional and the trailing airliners has been established. The next step is to evaluate the performance of conventional fly-by-wire systems in a formation flight scenario. Subsequent to this, the controllers can be adapted for better performance or stability if necessary. The validity of the decoupling assumption, along with the fact that the dynamics in the outer region are similar to that of isolated flight, are promising; it will likely allow the standard methodology and design for conventional control systems for fixed-wing aircraft [28, 29].

Chapter 4

Conventional Flight Control Systems

Subsequent to the trim and dynamics analysis, a flight control system will be developed to maintain a formation strategy for the convoy. The first step towards this goal is to design a conventional flight controller for isolated flight. Its performance will then be measured in both linear and non-linear formation flight simulations. The criteria for acceptable performance has not been defined in this thesis, but will be measured relative to the airliner in isolated flight with a similar flight control system architecture. The performance criteria will primarily consist of factors that influence control effort, fuel consumption and passenger comfort. It is likely that a compromise will have to be reached in a final design, and that all these factors will not be optimally addressed. It is not the goal for this design to produce a controller that is optimal for one or more of these criteria. Rather, the intention is to yield a design that is successful in maintaining formation with arguably acceptable performance according to theory and simulation. Furthermore, the design should be practically viable and implementable, and should be representative of current fly-by-wire systems [23, 31].

Specifically, in this chapter a set of conventional controllers for isolated flight will be designed, partially based on the available knowledge of the fly-by-wire architecture used by modern airliners. Eq. 3.6 shows the state space model used in the design of these controllers, assuming decoupling between longitudinal and lateral states, and therefore essentially 2 separate state space models. A set of controllers will be designed for both the longitudinal and lateral models separately. The longitudinal model controllers comprise of longitudinal and vertical controllers, as the system will be augmented to include vertical states, and there is strong coupling between the longitudinal and vertical states. The lateral model controllers will deviate from conventional fly-by-wire systems, particularly in the outer-loops, as the application and requirements of formation flight is very different to isolated flight concerning lateral control.

When deriving the lateral controllers, 2 different strategies will be investigated, namely: aileron-actuated, bank-to-turn strategy; and rudder-actuated, skid-to-turn strategy. The bank-to-turn strategy will most closely resemble fly-by-wire systems in the inner-loops, as it is standard procedure for airliners to bank when performing turning manoeuvres.

Linear and non-linear simulations will be used to validate the design, and measure the performance of the controllers, for isolated flight only. An analysis and discussion of the requirements for the controllers for the trailing airliner in formation flight will proceed thereafter in Chapter 5.

4.1 Longitudinal & Vertical Control

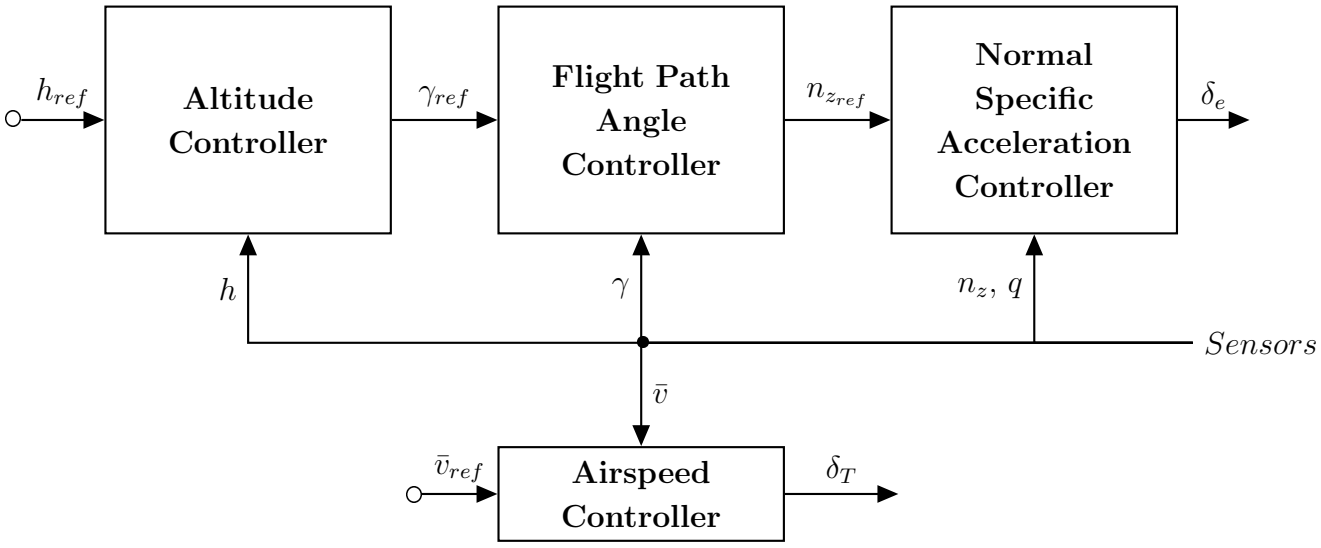

Figure 4.1: Longitudinal controllers architecture

The longitudinal controllers consist of an airspeed controller and a set of successive controllers: the normal specific acceleration (NSA) controller, enclosed by a flight path angle (FPA) controller, which is in turn enclosed by an altitude controller. For the sake of conciseness, the vertical controllers and states are encapsulated within longitudinal states and controllers, as there exists strong coupling between them. These controllers allow the airliner to maintain reference airspeed and altitude according to sensor readings, by ultimately generating elevator deflection and engine thrust references. Fig. 4.1 illustrates a high-level overview of this architecture.

4.1.1 Normal Specific Acceleration Controller

The NSA controller is the innermost vertical state controller. It regulates the downward acceleration in body-axis, approximated by Eq. 4.1, by commanding elevator deflection to change the angle of attack. Furthermore, it utilises pitch rate feedback to regulate pitch rate to zero. The design of the NSA controller is based on a design by Peddle in his PhD dissertation pertaining to an acceleration based flight control system [32]. It is in essence an integral controller with proportional pitch rate and normal specific acceleration feedback. The design entails a modern control pole placement strategy, thus requiring the selection of the desired pole positions for the

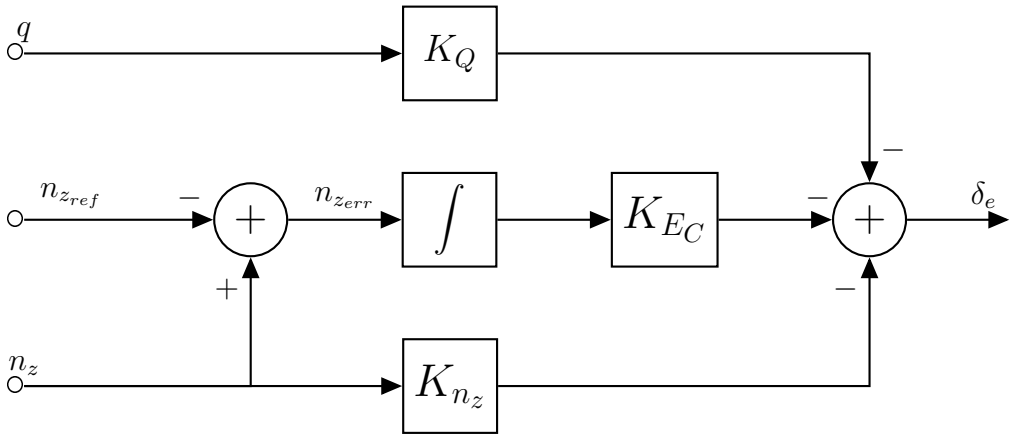

Figure 4.2: Normal specific acceleration controller architecture

closed loop NSA system. Peddle provides criteria for upper and lower frequency bounds for the desired closed loop poles. The upper frequency bound is given by Eq. 4.2, and the lower frequency bound is such that time-scale separation with airspeed is ensured. It should be noted however, that Peddle's design is based on a fixed-wing model aircraft, and that the requirements for the airliner may differ.

$$n_z = -\frac{L_\alpha}{m}\alpha = -\frac{qSC_{L_\alpha}}{m}\alpha \tag{4.1}$$

$$\omega_n < \frac{1}{3}\left|\sqrt{\frac{L_\alpha}{I_{yy}}\left(l_T - l_N\right)}\right| \tag{4.2}$$

As shown in Eq. 4.4, the longitudinal model is reduced and augmented to comprise of states: NSA, pitch rate and integrated NSA-error, described in Eq. 4.3. Using the upper frequency bound as a starting point, a first set of poles were found. Eventually, through an iterative design process, it was determined that the performance could be improved by choosing faster poles, which however breaks the upper frequency bound condition given by Eq. 4.2. This was verified in both linear and non-linear simulations.

$$E_C = n_z - n_{z_{ref}} \tag{4.3}$$

$$\begin{bmatrix} \dot{n_z} \\ \dot{q} \\ \dot{E_C} \end{bmatrix} = \begin{bmatrix} \mathbf{A}_{\text{long}_{22}} & -\frac{L_\alpha}{m}\mathbf{A}_{\text{long}_{23}} & 0 \\ -\frac{m}{L_\alpha}\mathbf{A}_{\text{long}_{32}} & \mathbf{A}_{\text{long}_{33}} & 0 \\ 1 & 0 & 0 \end{bmatrix} \begin{bmatrix} n_z \\ q \\ E_C \end{bmatrix} + \begin{bmatrix} -\frac{L_\alpha}{m}\mathbf{B}_{\text{long}_{21}} \\ \mathbf{B}_{\text{long}_{31}} \\ 0 \end{bmatrix} \delta_e \tag{4.4}$$

Subsequent to the selection of the desired poles, the feedback gains (K_{n_z}, K_{E_C}, K_Q) are calculated using the augmented model of Eq. 4.4 by means of a pole placement strategy. Next, the original longitudinal system is augmented to include integrated NSA-error, as well as feedback with the calculated gains. The resulting system matrix is given by Eq. 4.5, and the full augmented system by Eq. 4.6.

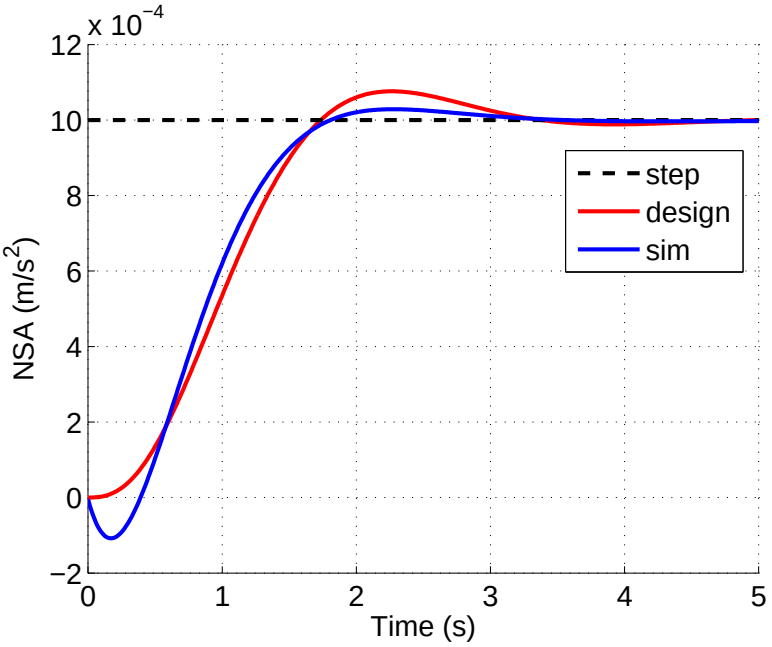

Figure 4.3: NSA controller: design vs simulation comparison

$$\mathbf{A_{NSA}} = \begin{bmatrix} \mathbf{A}_{\text{long}_{11}} & -\frac{m}{L_\alpha}\mathbf{A}_{\text{long}_{12}} & \mathbf{A}_{\text{long}_{13}} & \mathbf{A}_{\text{long}_{14}} & 0 \\ -\frac{L_\alpha}{m}\mathbf{A}_{\text{long}_{21}} & \mathbf{A}_{\text{long}_{22}} & -\frac{L_\alpha}{m}\mathbf{A}_{\text{long}_{23}} & -\frac{L_\alpha}{m}\mathbf{A}_{\text{long}_{24}} & 0 \\ \mathbf{A}_{\text{long}_{31}} & -\frac{m}{L_\alpha}\mathbf{A}_{\text{long}_{32}} & \mathbf{A}_{\text{long}_{33}} & \mathbf{A}_{\text{long}_{34}} & 0 \\ \mathbf{A}_{\text{long}_{41}} & -\frac{m}{L_\alpha}\mathbf{A}_{\text{long}_{42}} & \mathbf{A}_{\text{long}_{43}} & \mathbf{A}_{\text{long}_{44}} & 0 \\ 0 & 1 & 0 & 0 & 0 \end{bmatrix} - \begin{bmatrix} \mathbf{B}_{\text{long}_{11}} \\ -\frac{L_\alpha}{m}\mathbf{B}_{\text{long}_{21}} \\ \mathbf{B}_{\text{long}_{31}} \\ \mathbf{B}_{\text{long}_{41}} \\ 0 \end{bmatrix} \begin{bmatrix} 0 \\ K_{n_z} \\ K_Q \\ 0 \\ K_{E_C} \end{bmatrix}^T \tag{4.5}$$

$$\dot{\mathbf{x}}_{\mathbf{NSA}} = \mathbf{A_{NSA}} \cdot \mathbf{x_{NSA}} + \mathbf{B_{NSA}} \cdot n_{z_{ref}} \tag{4.6}$$

$$\mathbf{B_{NSA}} = \begin{bmatrix} 0 & 0 & 0 & 0 & -1 \end{bmatrix}^T \tag{4.7}$$

$$\mathbf{x_{NSA}} = \begin{bmatrix} \bar{v} & n_z & q & \theta & E_C \end{bmatrix}^T \tag{4.8}$$

Fig. 4.3 shows a comparison of the step response of the linear model according to the design, and the output of a full non-linear simulation. The overall profile and speed of response corresponds well, though the non-linear simulation reveals that there is an unmodelled non-minimum phase zero.

4.1.2 Airspeed Controller

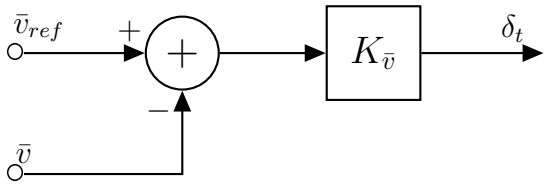

Figure 4.4: Airspeed controller architecture

Following the design of the NSA controller, it was deemed necessary to design an airspeed controller to regulate the airspeed dynamics. The airspeed couples strongly into the vertical dynamics, and a non-zero positive flight path angle cannot be maintained without regulating the airspeed. The airspeed controller is a simple proportional controller; the architecture is given by Fig. 4.4.

The design was approached by simplifying the airspeed dynamics to a first order equation, shown in Eq. 4.9, with time constant τ_{aspd}, given by Eq. 4.10. The full state model cannot easily be used for the design of airspeed controller, as the system is not yet stable in vertical dynamics. The design of the airspeed controller however needs to be done at this stage, as the design of the flight path angle controller will require stable airspeed dynamics. The feedback gain $K_{\bar{v}}$ is then calculated by means of root locus, shown by Fig. 4.5.

$$G_{aspd_{OL}}(s) \approx \frac{1}{m\left(s - A_{long_{11}}\right)} = \frac{1/m}{s - \tau_{aspd}} \tag{4.9}$$

$$\tau_{aspd} = \frac{\left(C_{L_M}\alpha_t + C_{D_M}\right)\left(q_t S + \rho \overline{V}_t V_s S C_{X_t}\right)}{m V_s} \tag{4.10}$$

Fig. 4.6a shows the expected step response of the linear closed-loop system, comparing it to the results of a non-linear simulation. Note that the engine dynamics have been excluded in both the linear and non-linear models for the initial design. The responses match very well with one another, thereby validating the approximation made in Eq. 4.9.

Fig. 4.6b shows the same comparison, but with a first order engine model included in the non-linear model for this simulation case. The effect of the engine dynamics is visible as under-damped

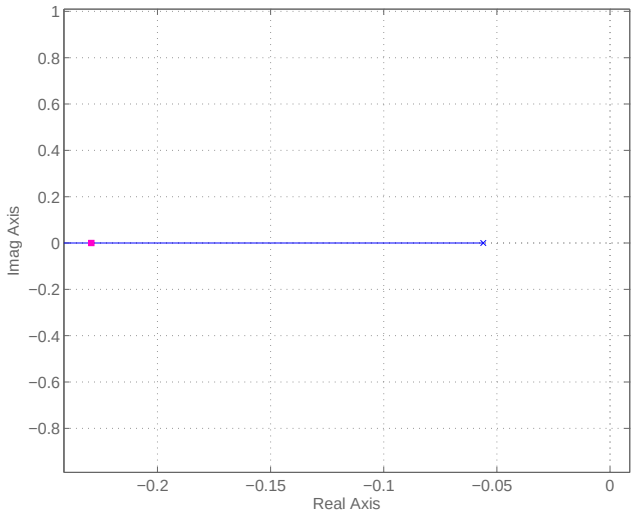

Figure 4.5: Airspeed controller root locus design

oscillations on the step response. It was deemed that the response matches well enough, and that the dynamics could be completely excluded from the linear design. This would allow for the linear model to be of a reduced order, which would make it more manageable. The airspeed controller would only be redesigned with engine dynamics included, in the case that dynamic throttling or longitudinal separation tracking becomes a significant problem; or if the flight-path angle controller design deviates significantly from the non-linear simulations.

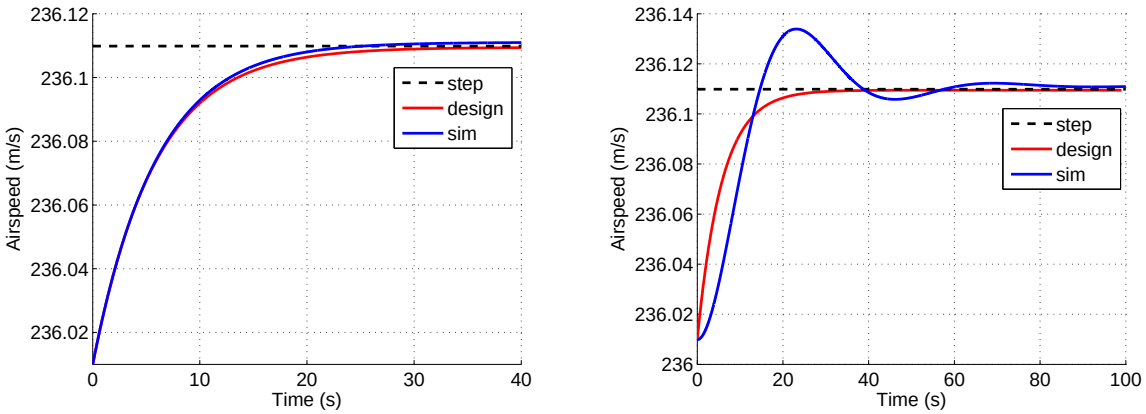

(a) Engine dynamics excluded in linear and non-linear models

(b) First order engine dynamics ($\tau = 7.5s$) included in non-linear model

Figure 4.6: Airspeed controller: design vs simulation

The airspeed controller feedback gain $K_{\bar{v}}$ was conservatively chosen, to limit the effect of the engine dynamics and decrease dynamic throttling of the engines. The NSA-augmented longitudinal system

is then further augmented to include the airspeed controller dynamics, done in Eq. 4.11.

$$\mathbf{A_{aspd}} = \mathbf{A_{NSA}} - \begin{bmatrix} \frac{1}{m} & 0 & 0 & 0 & 0 \end{bmatrix}^T \begin{bmatrix} K_{\bar{v}} & 0 & 0 & 0 & 0 \end{bmatrix} \tag{4.11}$$

4.1.3 Flight Path Angle Controller

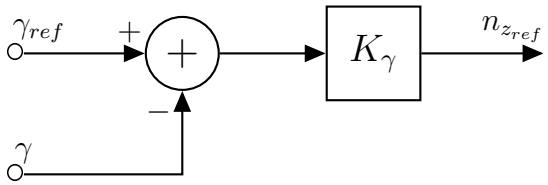

Figure 4.7: Flight path angle controller architecture

The FPA controller, illustrated by Fig. 4.7, is the next vertical controller and encloses the NSA controller. It is responsible for regulating the flight path angle, as is defined by Eq. 4.12, by supplying the NSA controller with a reference. The open-loop flight path angle model is the airspeed-augmented closed-loop model A_{aspd}, with an output vector defined by Eq. 4.13, and input vector B_{NSA}.

$$\gamma = \theta - \alpha \tag{4.12}$$

$$C_\gamma = \begin{bmatrix} 0 & \frac{m}{L_\alpha} & 0 & 1 & 0 \end{bmatrix} \tag{4.13}$$

The design of the closed-loop feedback gain K_γ constitutes a classical root-locus design, as shown in Fig. 4.8. The gain was chosen to give a fast, but well-damped response, while ensuring stability. The FPA controller was included in the Simulink model, and a non-linear simulation was run with a small FPA step reference. The output is compared to the expected step response according to the linear model of the design in Fig. 4.9. They compare well, further indicating that the exclusion of the engine dynamics from the linear model, as was done in the airspeed controller design, is acceptable.

The flight path angle controller is then augmented into the airspeed-augmented system, done in Eq. 4.14.

$$\begin{aligned} \mathbf{A}_\gamma &= \mathbf{A_{aspd}} - \mathbf{B_{NSA}} K_\gamma \mathbf{C}_\gamma \\ \mathbf{B}_\gamma &= K_\gamma \mathbf{B_{NSA}} \end{aligned} \tag{4.14}$$

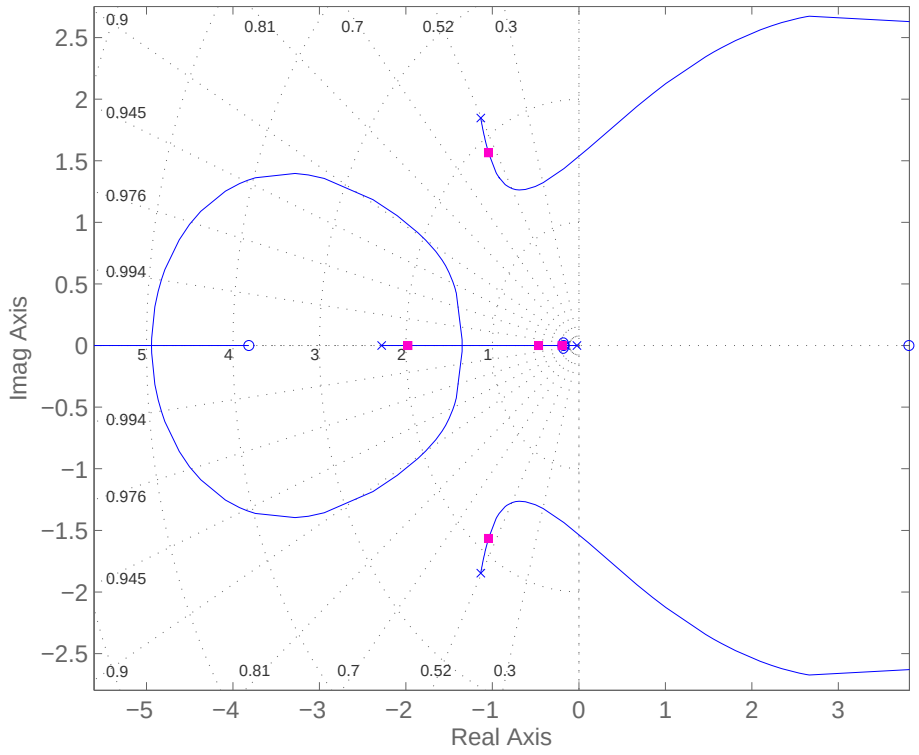

Figure 4.8: FPA controller design root-locus

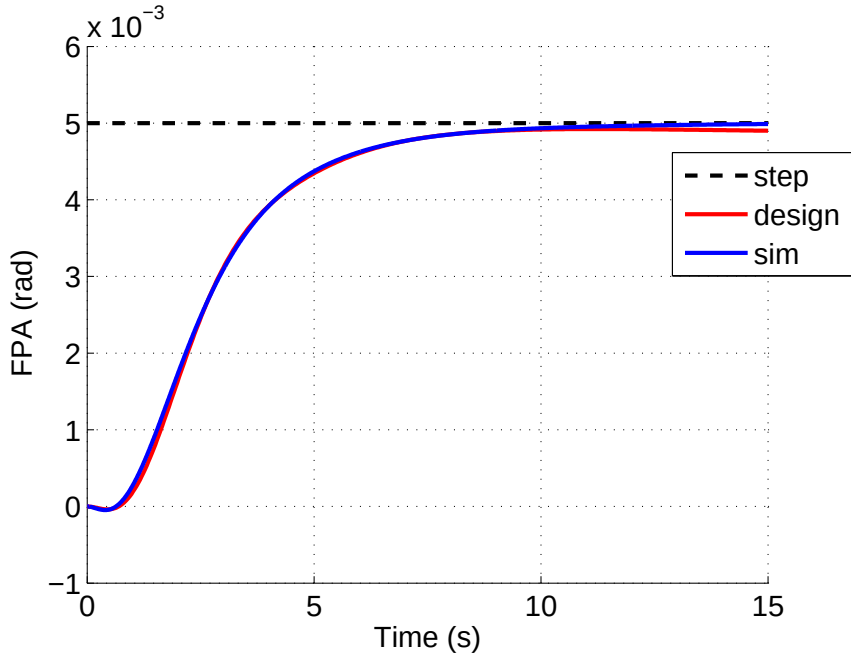

Figure 4.9: FPA controller: design vs simulation comparison

4.1.4 Altitude Controller

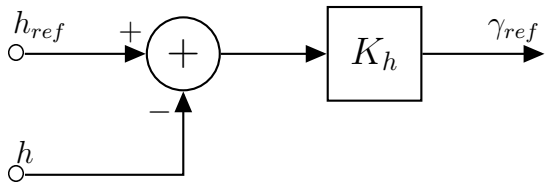

Figure 4.10: Altitude controller architecture

The outermost vertical controller is the altitude controller; its architecture is shown in Fig. 4.10. The altitude controller regulates the altitude by commanding a reference to the FPA controller. The first step towards designing the altitude controller is the augmentation of the closed-loop FPA system with an altitude state. This requires a differential equation to describe the altitude, for which the approximation given by Eq. 4.15 is sufficient. Next, the state vector and state matrix are augmented to include the altitude state, as demonstrated in Eq. 4.16 and Eq. 4.17 respectively, taking into account that the original angle of attack state had been replaced with a NSA state.

$$\dot{h} = -\gamma \bar{V}_t \tag{4.15}$$

$$\mathbf{x_h} = \begin{bmatrix} \bar{v} & n_z & q & \theta & E_C & h \end{bmatrix}^T \tag{4.16}$$

$$\mathbf{A}_{h_{OL}} = \begin{bmatrix} \mathbf{A}_\gamma & \mathbf{0} \\ \mathbf{C}_{\dot{h}} & \end{bmatrix} \tag{4.17}$$

$$\mathbf{C}_{\dot{h}} = \begin{bmatrix} 0 & -\dfrac{m}{L_\alpha}\bar{V}_t & 0 & -\bar{V}_t & 0 & 0 \end{bmatrix} \tag{4.18}$$

The feedback gain K_h is then calculated by root locus method, as shown in Fig. 4.11. Next, the feedback is augmented into the state space representation, as done in Eq. 4.19. The augmented state space representation is then used to generate a step response, as shown in Fig. 4.12. The expected output according to the linear model compares very well to that of a non-linear simulation, also shown in Fig. 4.12.

$$\begin{aligned} \mathbf{B}_h &= K_h \begin{bmatrix} \mathbf{B}_\gamma^T & 0 \end{bmatrix}^T \\ \mathbf{C}_h &= \begin{bmatrix} 0 & 0 & 0 & 0 & 0 & 1 \end{bmatrix} \\ \mathbf{A}_h &= \mathbf{A}_\gamma - \mathbf{B}_h \mathbf{C}_h \end{aligned} \tag{4.19}$$

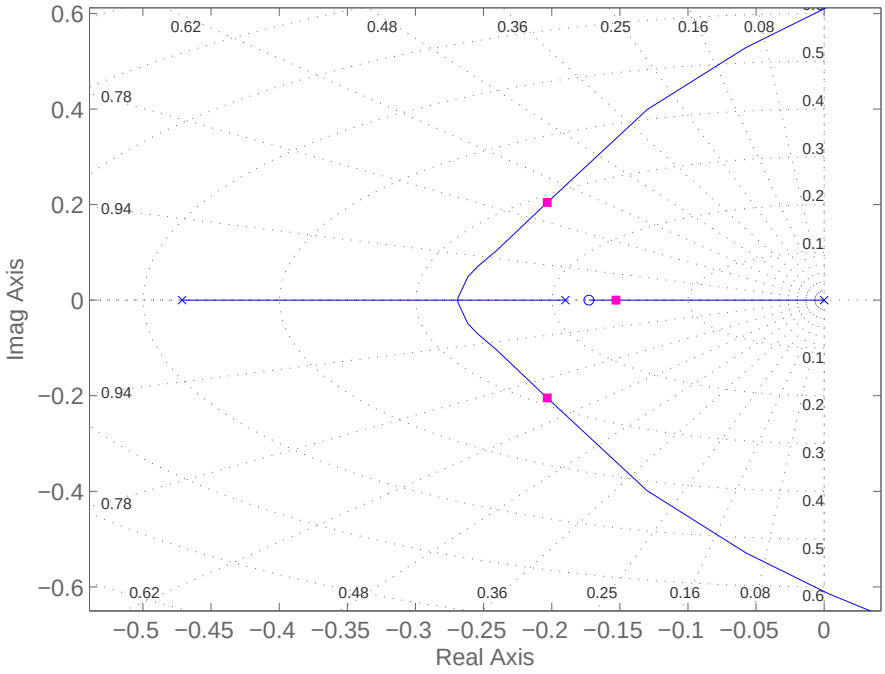

Figure 4.11: Altitude controller design root-locus

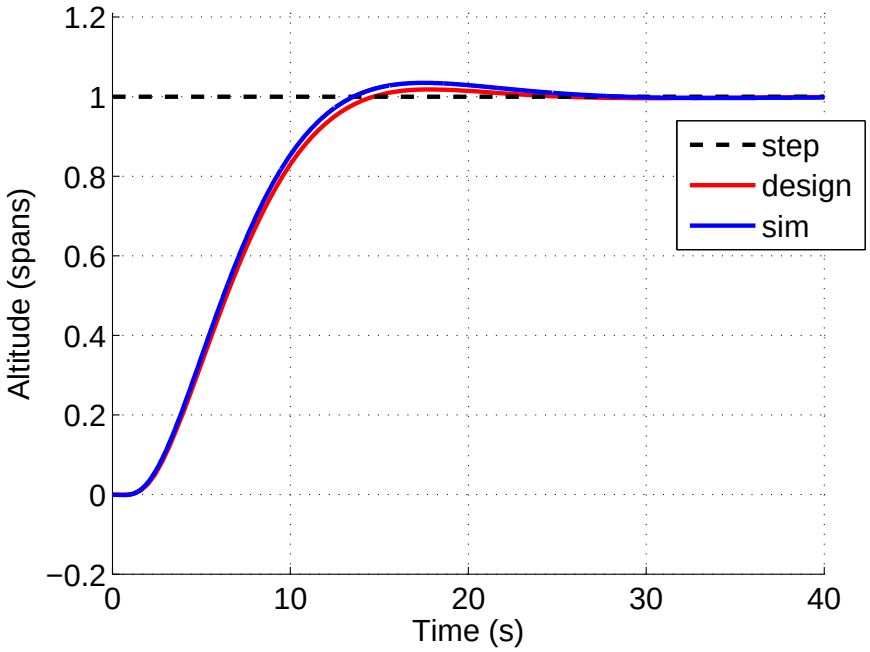

Figure 4.12: Altitude controller: design vs simulation comparison

4.2 Lateral Control: Bank-to-turn Strategy

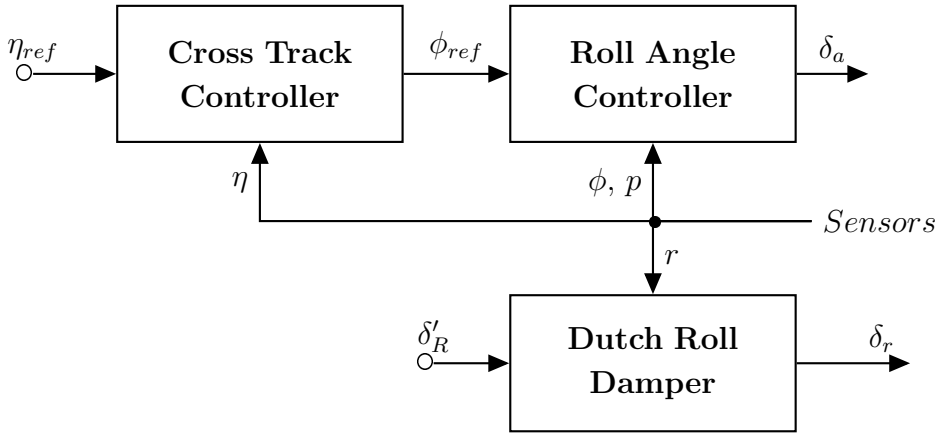

Figure 4.13: Lateral controllers architecture

The bank-to-turn strategy lateral controllers aim to ultimately regulate lateral separation, or cross-track, through aileron-actuation. This is done by inducing a roll-rate, and thus a roll angle by actuating the ailerons. If this regulated roll angle is non-zero, it causes the airliner to bank and thus accelerate laterally. Furthermore, the lateral control architecture includes a Dutch roll damper, which actuates the rudder to damp out the Dutch roll mode.

4.2.1 Dutch Roll Damper

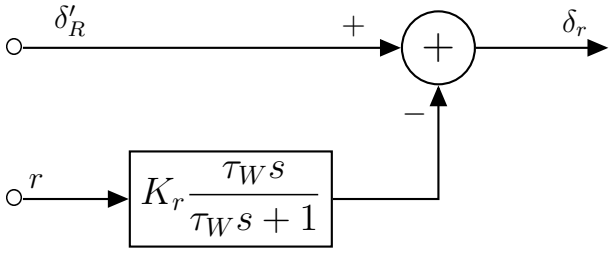

Figure 4.14: Dutch roll damper architecture

The Dutch roll damper (DRD) is a typical component of the flight control system with the purpose of damping the Dutch roll mode oscillations. Under-damped Dutch roll oscillations are expected for the Boeing 747 model used, as the dihedral effects are large. Fig. 4.15a shows the under-damped Dutch roll response with a period of approximately $6.32s$, generated by means of a non-linear simulation initialised with a sideslip angle of $0.1°$.

Subsequently, a washout filter is designed with a time constant $\tau_W = 12.6s$. The filter is augmented into the system, and a root locus design follows to find a suitable value for feedback gain K_r, as shown in Fig. 4.16. The resulting damped Dutch roll response is given by Fig. 4.15b.

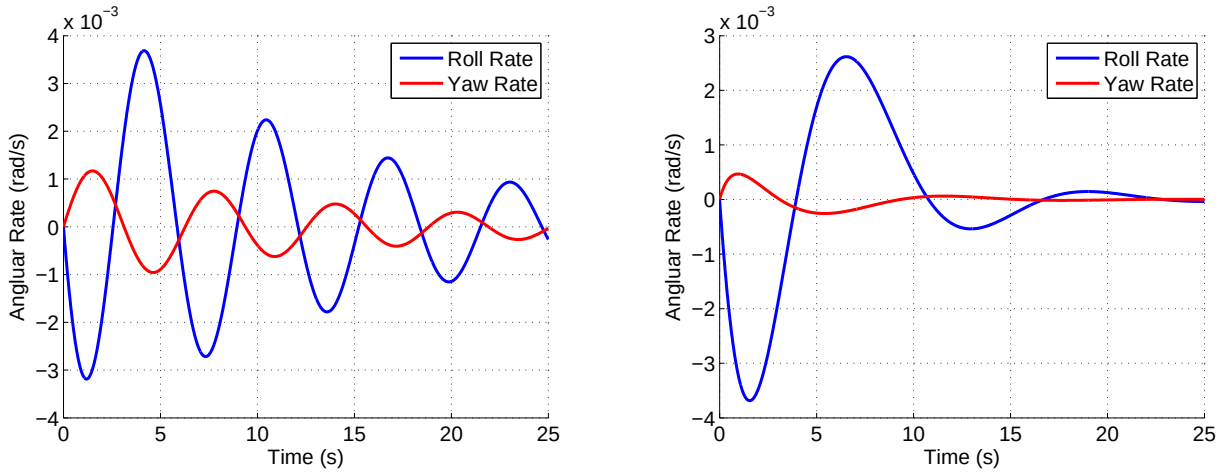

(a) Dutch roll response

(b) Damped Dutch roll response

Figure 4.15: Comparison of natural Dutch roll oscillations vs damped Dutch roll oscillations due to DRD; Non-linear simulations initialised with $\beta = 0.1^{\circ}$

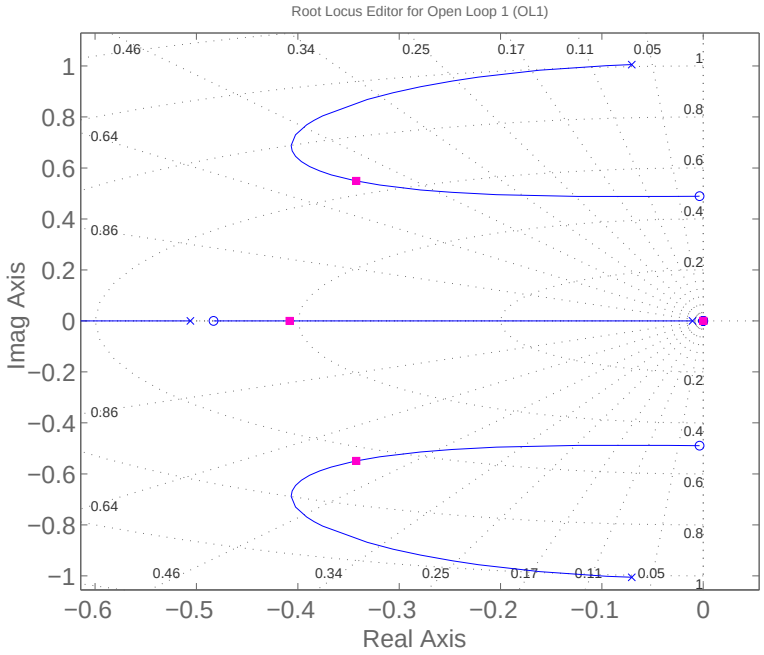

Figure 4.16: DRD root locus design

Following the design of the DRD feedback gain K_r, the open-loop lateral system is augmented to include the feedback dynamics, as is done in Eq. 4.20. The washout filter is left out during the augmentation to reduce the order of the linear model. This would only be added in the case where the linear and non-linear simulations begin to deviate significantly.

$$\mathbf{A_{drd}} = \mathbf{A_{lat}} - \mathbf{B}_{\delta_r} K_r \mathbf{C_r} \tag{4.20}$$

4.2.2 Roll Angle Controller

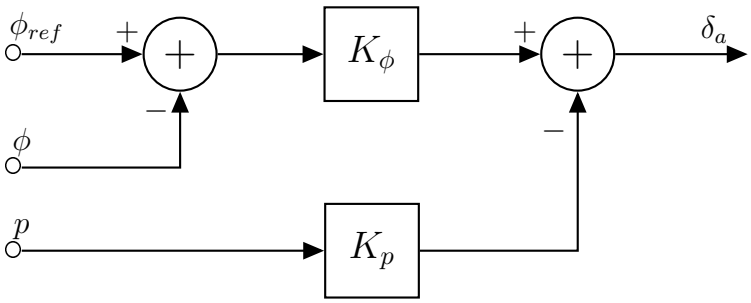

Figure 4.17: Roll angle controller architecture

The roll angle controller illustrated by Fig. 4.17, regulates roll angle directly by commanding aileron deflection. It utilises roll rate feedback to regulate the roll rate to zero, and thus provides damping to the system by removing energy. The design is done with the aid of a classical root locus method to find an initial set of gains, with the assumption that the roll angle feedback gain can be approximated as the derivative gain in a PD-controller. This approximation makes the assumptions that $p \approx \dot{\phi}$, and that the reference signal is not differentiated. In practice however, it is undesirable to differentiate the reference signal, as this can cause large overshoot for step inputs, or inputs with large derivatives. The initial gains are thus tweaked until the system's performance is satisfactory, according to the augmented model, derived in Eq. 4.21.

$$\begin{aligned} \mathbf{A}_\phi &= \mathbf{A_{drd}} - \mathbf{B}_{\delta_a} \begin{bmatrix} 0 & K_p & 0 & K_\phi \end{bmatrix} \\ \mathbf{B}_\phi &= \mathbf{B}_{\delta_a} K_\phi \end{aligned} \tag{4.21}$$

The step response of the final roll angle controller is shown in Fig. 4.19, comparing the expected output of the design with that of a non-linear simulation. The response is very quick and damped, and matches well even for the non-linear case. Note however, that the input step size is unrealistically small. In fact, for such a small step, the controller could be made even more aggressive and fast without affecting the system's apparent damping.

An extremely aggressive controller is not practically realisable however, as for larger input magnitudes, the step responses of the non-linear simulations begin to deviate from what is expected according to the linear design; visualised in Fig. 4.20. It can thus be deduced that for larger input magnitudes, non-linearities such as the responsiveness of the ailerons – approximated by a slew rate limiter – and saturation, come into effect. On Fig. 4.20 it can be seen that the initial responses for such large inputs are slower than what is predicted by the design, and some overshoot is visible.

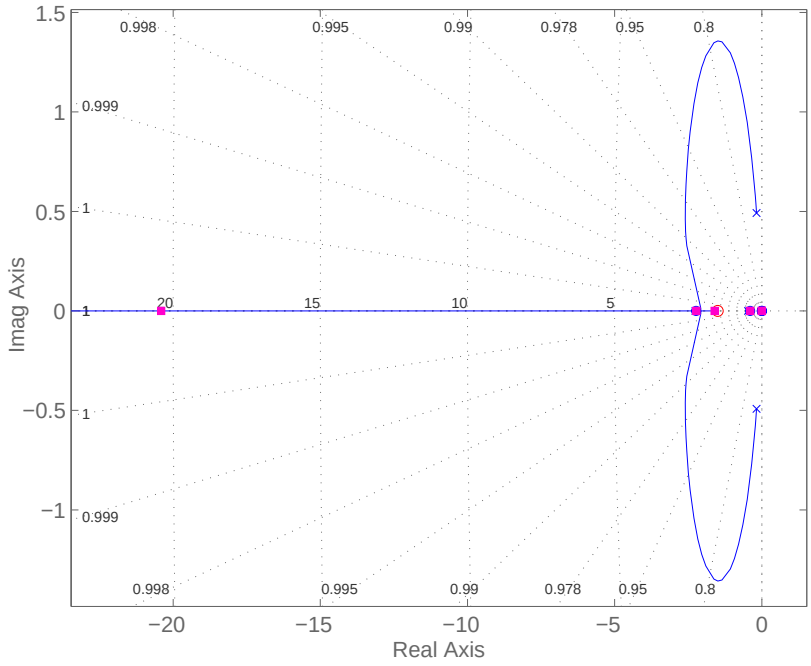

Figure 4.18: ϕ-controller root locus design

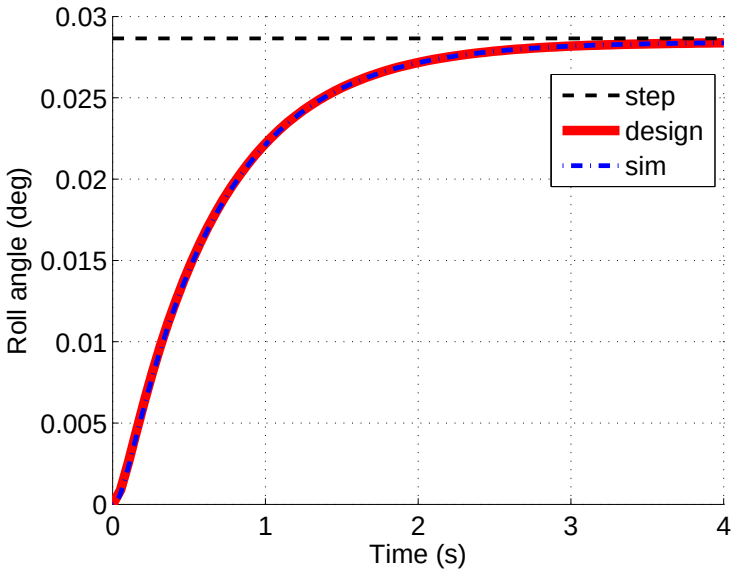

Figure 4.19: Roll angle controller: design vs simulation comparison

This effect is amplified greatly by making the controller more aggressive, as illustrated in Fig. 4.21, resulting in a system that appears under-damped.

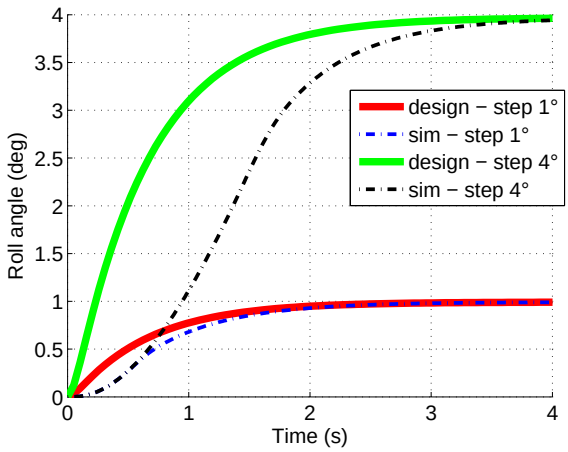

Figure 4.20: Roll angle step responses for varying step sizes uncover slew rate limitations

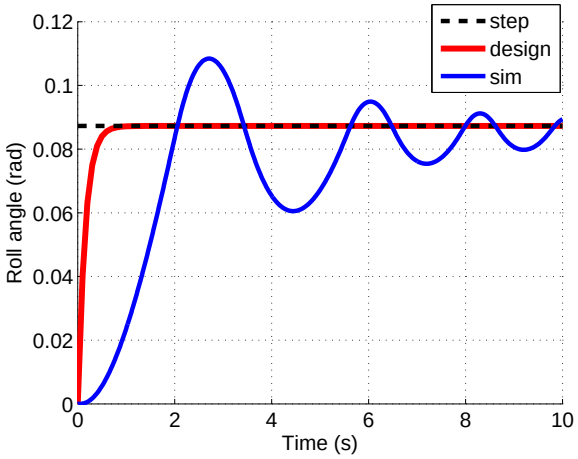

Figure 4.21: Bad performance of high gain system due to slew rate limit

4.2.3 Cross Track Controller

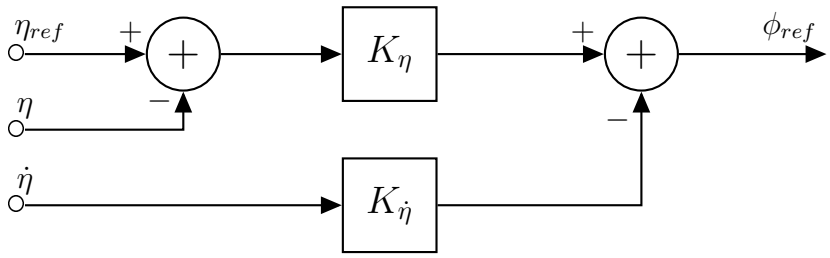

Figure 4.22: Cross track controller architecture

The cross track controller is responsible for regulating the cross track separation to a reference value. This will be required for formation flight to regulate lateral separation η, and will hence be referred to as the η-controller. The following design however, is for the airliner in isolation, and is required so that comparisons can be drawn between isolated and formation flight performance. The η-controller is thus not part of conventional fly-by-wire systems, but is essential for formation flight. The architecture of the η-controller is given by Fig. 4.22, and is in essence a proportional controller with lateral separation rate $\dot{\eta}$ feedback.

The initial gains were designed by means of root locus, illustrated in Fig. 4.23, where the lateral separation rate feedback gain is approximated as the derivative term of the PD-design. The root locus however, required that the state space model be augmented to include a η and $\dot{\eta}$ state, as was done in Eq. 4.22.

$$\mathbf{A}_{\eta_{OL}} = \begin{bmatrix} \mathbf{A}_\phi & \mathbf{0} & \mathbf{0} \\ \mathbf{C}_{\ddot{\eta}} & & \\ \mathbf{C}_{\dot{\eta}} & & \end{bmatrix} \qquad \begin{aligned} \mathbf{C}_\eta &= \begin{bmatrix} 0 & 0 & 0 & 0 & 0 & 1 \end{bmatrix} \\ \mathbf{C}_{\dot{\eta}} &= \begin{bmatrix} 0 & 0 & 0 & 0 & 1 & 0 \end{bmatrix} \\ \mathbf{C}_{\ddot{\eta}} &= \begin{bmatrix} 0 & 0 & \dfrac{V_t \sec\theta_t}{b} & 0 & 0 & 0 \end{bmatrix} \end{aligned} \tag{4.22}$$

The gains were iteratively refined, continually evaluating the step response according to the linear, augmented model, until satisfactory performance was achieved. The process was repeated using non-linear simulations until the aileron command was within reasonable saturation and rate limits. Subsequently, the resulting feedback is augmented into the lateral model, done in Eq. 4.23, yielding a closed-loop system capable of tracking CT-references.

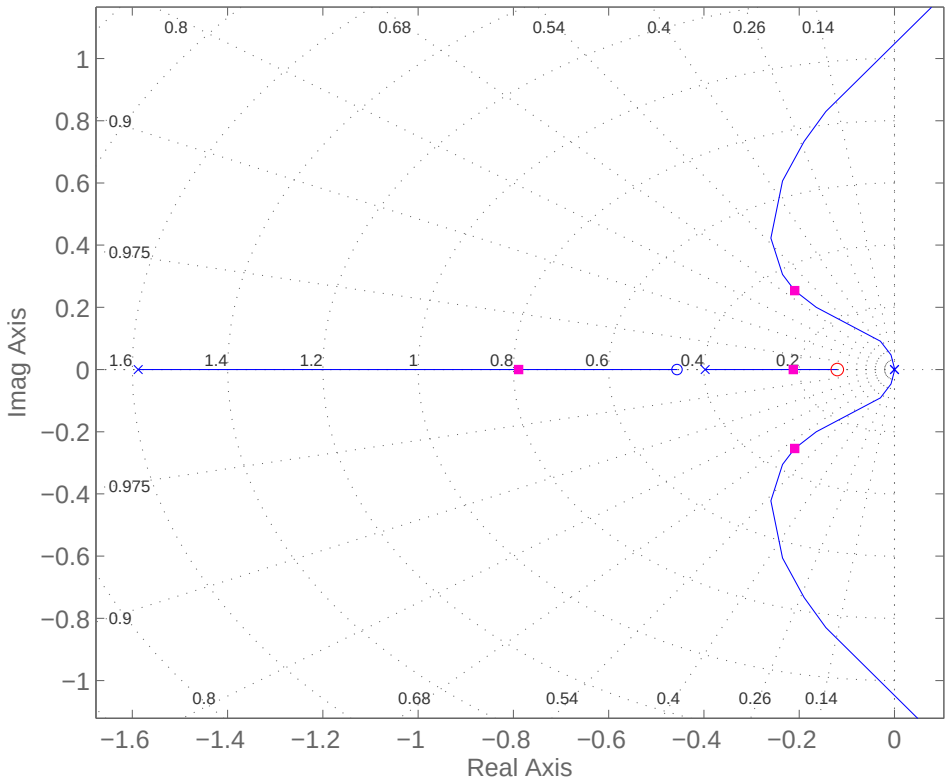

Figure 4.23: CT-controller root locus design

$$\mathbf{A}_\eta = \mathbf{A}_\phi - \begin{bmatrix} \mathbf{B}_\phi \\ 0 \end{bmatrix} \begin{bmatrix} 0 & 0 & 0 & 0 & K_{\dot{\eta}} & K_\eta \end{bmatrix}$$
$$\mathbf{B}_\eta = K_\eta \begin{bmatrix} \mathbf{B}_\phi \\ 0 \end{bmatrix} \tag{4.23}$$

Fig. 4.24a shows the step response for the final η-controller design, comparing the expected response of the linear design to that of a non-linear simulation. Though a clear, albeit small discrepancy exists, the profile and rate of the response of the linear and non-linear systems are similar. This discrepancy is likely due to the simplifying approximation made for the description of $\ddot{\eta}$ in Eq. 3.19. It is shown in Fig. 4.24b that the linear and non-linear systems match equally well for a different set of gains, indicating that the error is unrelated to the controller design.

Finally, Fig. 4.25 shows that the system performs consistently and acceptably well for inputs much larger than what is required for maintaining formation. However, the rate limiters and saturation effects are visible in the output, and limit the speed at which the system responds.

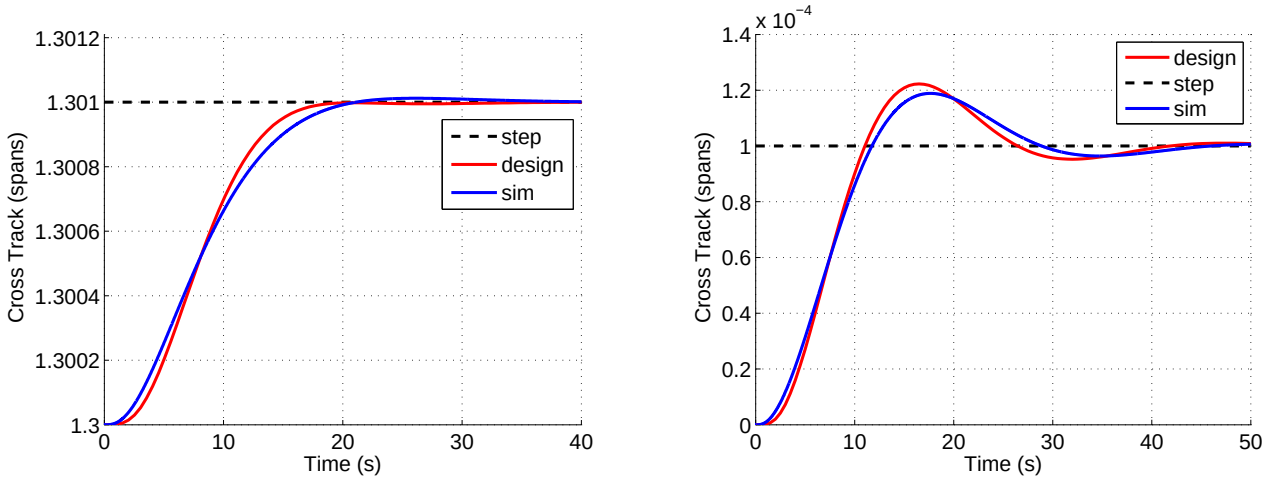

(a) Final gains

(b) Alternative gains

Figure 4.24: η-controller: design vs simulation comparison

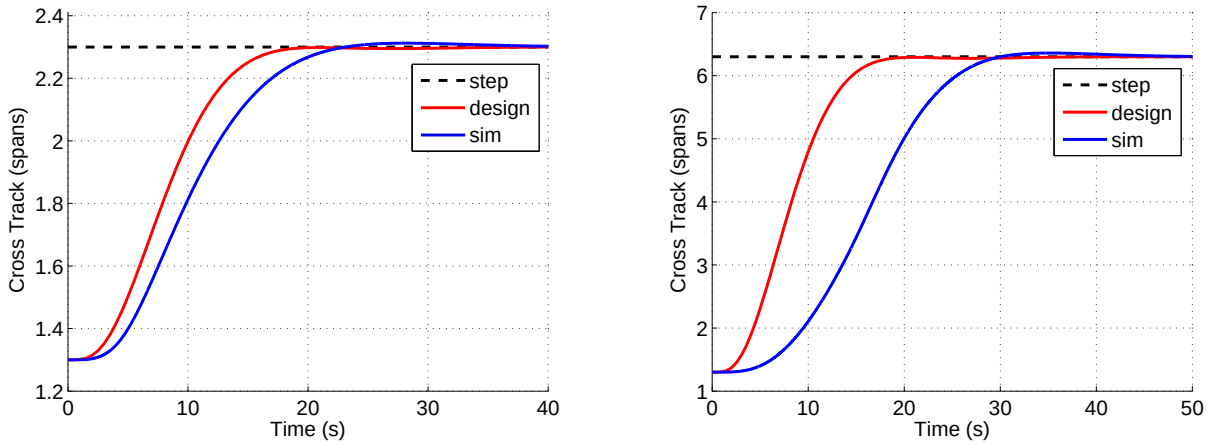

(a) Large η-step response

(b) Very large η-step response; slew rate limiters and saturation effects visible

Figure 4.25: η-controller performance for large step inputs; design vs. simulation

4.3 Lateral Control: Skid-to-Turn Strategy

The skid-to-turn strategy ultimately utilises rudder-actuated control, to induce a change in yaw angle, and thus a lateral separation rate, to effectively regulate lateral separation. The architecture of the skid-to-turn strategy is presented by Fig. 4.26. This architecture has two major structural differences compared to that of the bank-to-turn strategy:

1. The DRD is completely removed and replaced by a heading difference controller. The heading difference is defined as the difference in heading of the trailing airliner, and the track of the

formation leader. The heading-difference controller ($\Delta\psi$-controller), contains yaw rate $\dot{\psi}$ feedback, which removes energy from the system to aid in the stability and damping of the lateral separation response.

2. The ϕ-controller is reconfigured to regulate the roll angle to zero, and lateral separation regulations is handled via rudder-actuation. The reasoning behind this idea is that there are large roll and roll rate dynamics associated with formation flight, and this strategy will attempt to avoid exciting these dynamics as much as possible. The roll angle controller will not be redesigned however, and will instead use the controller designed in Section 4.2.2, but will instead receive a zero roll angle reference.

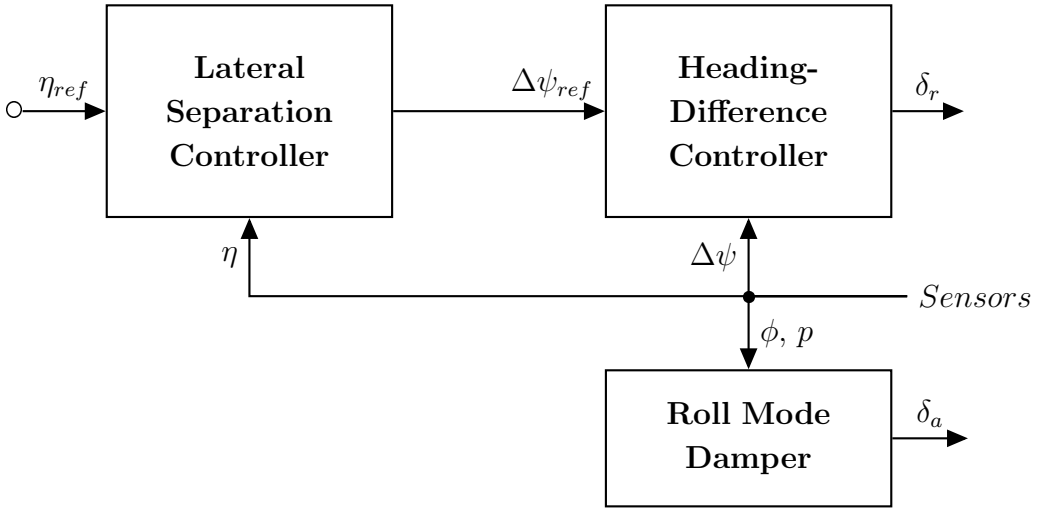

Figure 4.26: Rudder-actuated, skid-to-turn lateral controllers architecture.

4.3.1 Heading-Difference Controller

The heading-difference $\Delta\psi$-controller regulates the difference in heading between the leading and trailing airliners. It completely replaces the Dutch roll damper found in the standard fly-by-wire control system. A non-zero heading difference causes a non-zero lateral separation rate between the two airliners, with the function $\dot{\eta} = \Delta\psi\frac{V_t}{b}$. It is a proportional controller, with yaw rate feedback; and will thus still damp out the Dutch roll mode. It is designed as a PD-controller, with the assumption that the derivative gain of the PD-controller is approximately equal to the yaw rate feedback gain K_r.

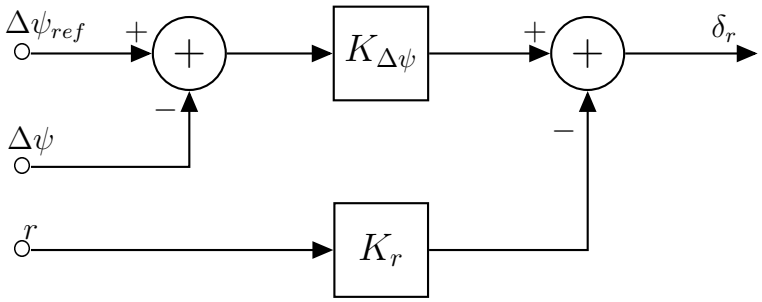

Figure 4.27: $\Delta\psi$-controller architecture

4.3.2 Cross Track Controller

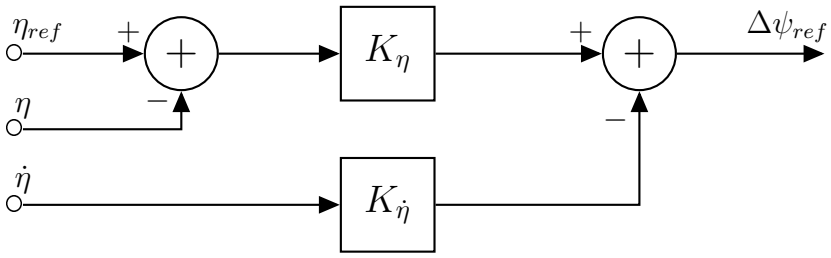

Figure 4.28: Skid-to-turn strategy cross-track controller architecture

The design of the skid-to-turn cross track controller is very similar to that of the bank-to-turn cross track controller, which was discussed in Section 4.2.3. It however generates a reference signal for the $\Delta\psi$-controller, as opposed to the ϕ-controller as done for the bank-to-turn strategy. The root locus design for this controller is shown in Fig. 4.30. Note that the focus of the root locus diagram shown is the dominant poles near the origin. With the controller augmented into the lateral system, the linear and non-linear simulations match well, as shown in Fig. 4.29a. Furthermore, the system responds well for large step inputs with the inclusion of a saturation element after the output of the η-controller, as shown in Fig. 4.29b.

The response of the skid-to-turn controller is slower than that of the bank-to-turn controller, though it avoids exciting roll dynamics. Furthermore, it deviates significantly from the conventional lateral control model, which is the bank-to-turn architecture – and as such is less likely to viable in practical airliner applications. It may yield interesting results in a formation flight scenario however, and will therefore be investigated.

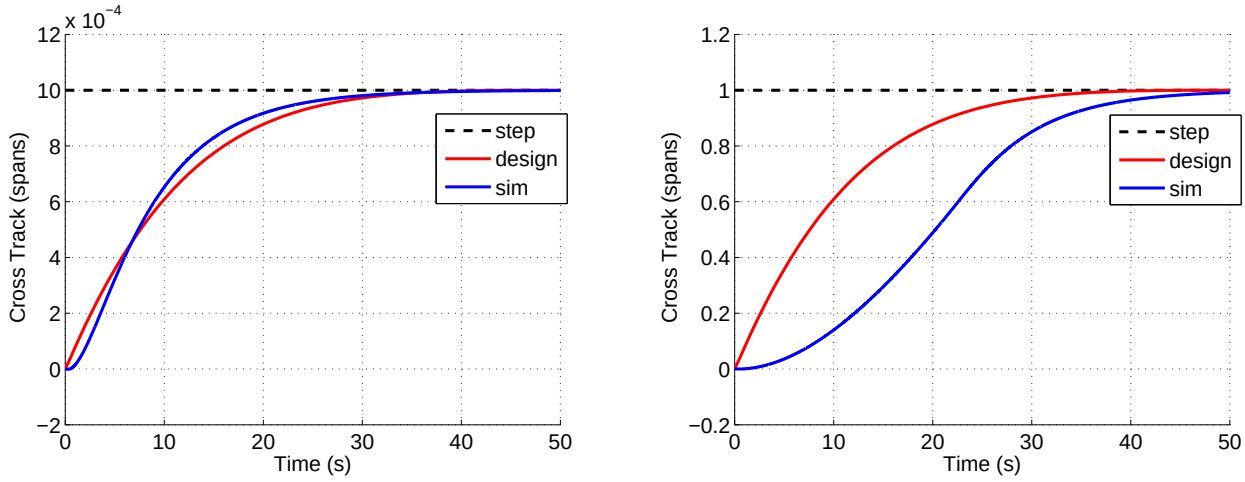

(a) Small step input

(b) Large step input

Figure 4.29: Skid-to-turn η-controller: design vs simulation comparison

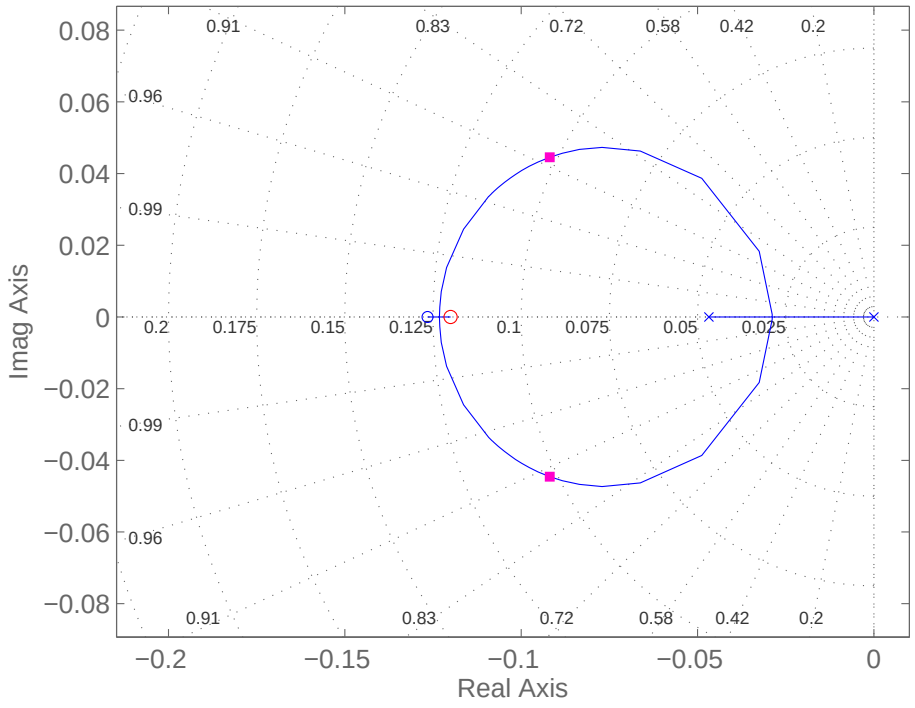

Figure 4.30: Skid-to-turn strategy CT-controller root locus design

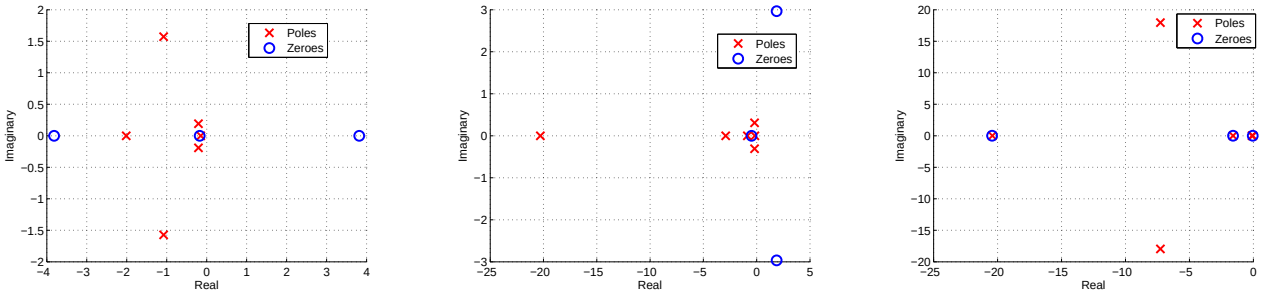

(a) Longitudinal system (b) Bank-to-turn lateral system (c) Skid-to-turn lateral system

Figure 4.31: Pole-zero maps for closed-loop longitudinal and lateral systems

4.4 Closed-Loop Dynamics

With the controllers fully augmented into the state space representations, pole-zero maps are generated for the longitudinal and lateral systems, shown in Fig. 4.31. These will be useful as a baseline for the comparison of the dynamics of the controllers in formation flight to the dynamics of the controllers in isolated flight. The precise locations for the longitudinal and lateral systems are listed in Table 4.1. Note that these will vary depending on the aggressiveness of the controllers. Finally, it is interesting to note that the skid-to-turn strategy lateral controllers naturally cancel out some of the poles with its zeroes, effectively leaving a dominant pole near the origin, and a complex pair of very fast, under-damped poles.

Longitudinal Poles	**Bank-to-turn Poles**	**Skid-to-turn Poles**
-2.014	-0.164	$-0.092 \pm 0.045j$
-0.154	-0.876	$-9.2 \pm 6.25j$
$-1.077 \pm 1.573j$	-2.907	-1.59
$-0.202 \pm 0.206j$	-20.29	-20.39
	$-0.195 \pm 0.309j$	

Table 4.1: Closed-loop longitudinal and lateral poles

4.5 Conclusion

A complete set of longitudinal, vertical and lateral controllers, partially based on representative fly-by-wire systems, for the airliner in isolation have been developed. The designs proved successful in both linear and non-linear simulations, with results matching acceptably. Two different architectures were investigated for lateral control, based on the bank-to-turn and skid-to-turn strategies.

There is no clear benefit of one over the other, though the bank-tot-turn strategy more closely resembles the conventional architecture [31].

The stability and dynamics of the representative fly-by-wire system were then evaluated in isolated flight conditions. With the inclusion of the cross-track controller as a conventional controller, only minor architectural changes are necessary to allow for the analysis of the airliner in controlled formation flight. This chapter partially addresses research objectives (4) - (6).

Chapter 5

Formation Flight Extended Control Systems

A set of conventional flight controllers, partially based on current fly-by-wire systems for the airliner in isolated flight, have been derived. Subsequently, it is necessary to evaluate the performance of these conventional controllers in formation flight, and make adaptations or do complete redesigns where necessary. This was done for each of the individual controllers derived in Chapter 4. The most significant required changes will be discussed in the relevant sections, along with new structures to the control system where applicable.

The redesign and adaptation was done as an iterative process, continually improving the design; which often constituted in tightening the control laws. The results and designs presented here reflect the state of the controllers at the end of this design process. The structures and control laws designed for formation flight were fed back into the conventional system design, and were evaluated for performance in isolated flight. Thereafter, the design was again adapted to find a suitable compromise between both isolated and formation flight scenarios where possible. Certain trade-offs exist, since the mechanics and strategies for formation flight and isolated flight are dissimilar; in particular, the airliners taking part in formation flight need only fly straight and level. This allows for more aggressive control, as the control signals will inherently be smaller, which is less likely to cause passenger discomfort or saturation effects. The goal is therefore to find a suitable level of controller aggressiveness for both formation flight and isolated flight manoeuvres; though formation flight is given preference for the cases where little comprise can be found.

5.1 Longitudinal & Vertical Control

The required longitudinal controllers for the airliner in formation flight are nearly identical to the conventional controllers discussed in Section 4.1. The first adaptation for the vertical controllers is the remapping of the inputs of the altitude controller to vertical separation. That is, h_{ref} and

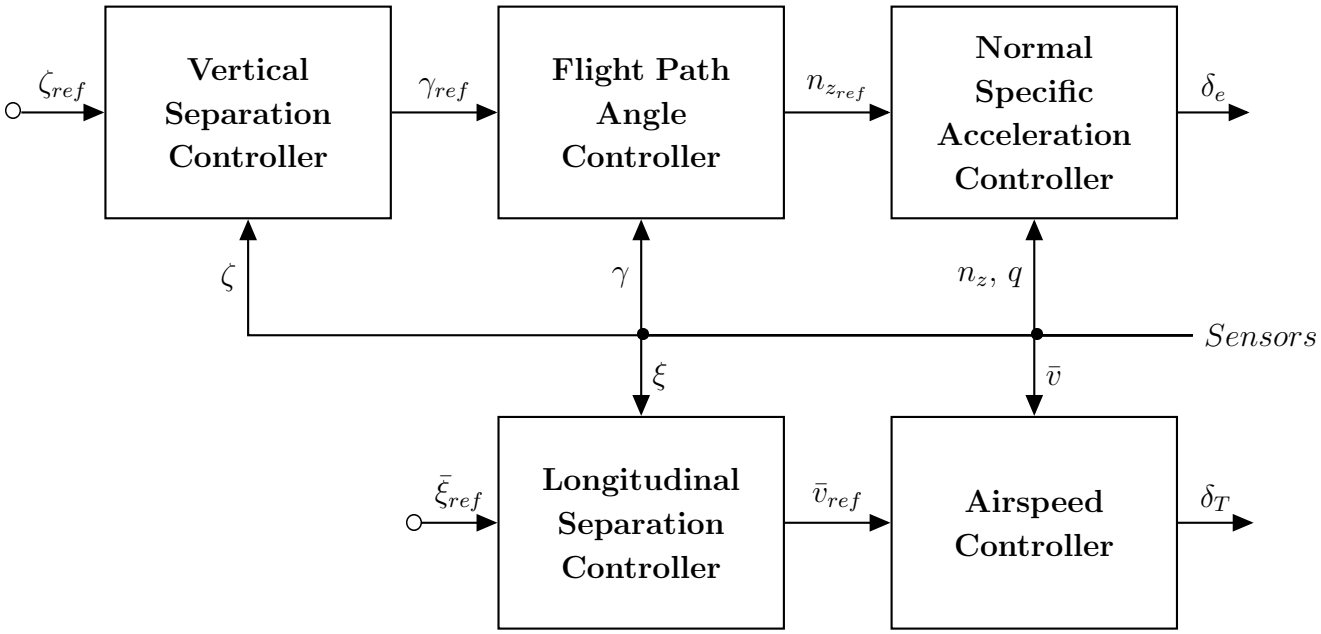

Figure 5.1: Extended longitudinal controllers architecture

h, are remapped to ζ_{ref} and ζ respectively, where ζ_{ref} is the commanded vertical separation to be maintained between the trailing and leading airliners.

In practice, the vertical separation controller will require the knowledge of the differential altitude of the leading and trailing airliners, likely obtained from DGPS data. For the design using the linear model however, this is not required as it is assumed that the leading airliner flies a perfectly straight and level path, and that its altitude will remain constant. The consequence of this is that the design of the vertical separation controller is identical to that of the altitude controller, neglecting interaction forces and moments for the moment. It is necessary to be consistent with units however. Recalling that altitude is measured in meters, and vertical separation in wingspans, it is necessary to adapt the gain of the altitude controller to compensate for this conversion. This is simply done as follows: $K_\zeta = K_h/b$. The new gain K_ζ, replaces K_h, resulting in a new architecture for the vertical controller illustrated in Fig. 5.2, which is now referred to as the vertical separation controller.

Next, a longitudinal separation controller (ξ-controller), was added to enclose the airspeed controller for the purpose of regulating in-track distance. With the remapping and additional ξ-controller in place, the overall architecture is illustrated in Fig. 5.1. Using this adapted architecture, an initial analysis showed that no change is required to the inner-loop controllers – that is the FPA-, NSA- and $\bar{v}$-controllers – to maintain the desired transient and steady-state performance; this is especially true for the outer region. This is expected since the open-loop dynamics analyses in Section 3.2.3 revealed that the conventional flight mode poles were largely unaffected by the formation flight interactions, and that it is the additional formation flight poles that are most affected by the formation flight aerodynamic interactions.

5.1.1 Vertical Separation Controller

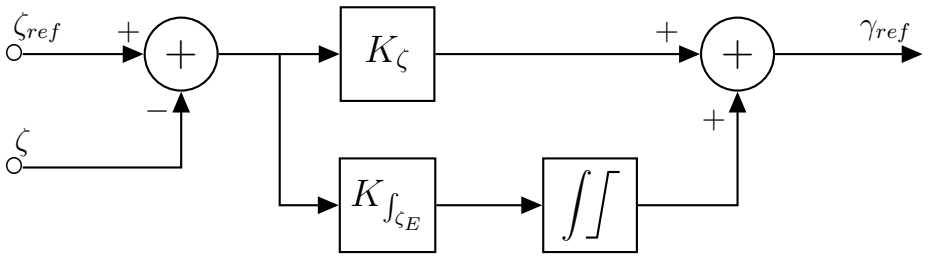

Figure 5.2: Vertical separation controller architecture

Fig. 5.2 shows the ζ-controller with the inputs remapped to vertical separation as previously discussed. Furthermore, an integrator is added to improve vertical separation tracking performance; thus the design becomes a PI-design, unlike the conventional controller. The integrator is limited to prevent wind-up for large steps.

To begin the process of the verification and redesign of the outer-loop longitudinal and vertical controllers for the purpose of formation flight, the relevant linear models need to be established. This involves augmenting the formation flight linear models, developed in Chapter 3 with the inner-loop controllers, developed in Chapter 4.

A short-cut approach is taken, by augmenting the conventional FPA-controlled system of Eq. 4.14, with the formation flight interaction coefficients and vertical separation state. This resembles what was done during the derivation of the formation flight extended linear model in Chapter 3. Furthermore, an integral state is added for the integrator of the vertical separation controller. This results in the following state space representation for the open-loop vertical separation system,

$$\mathbf{A}_{\zeta_{OL}} = \begin{bmatrix} \mathbf{A}_\gamma & \mathbf{F}_{\zeta_{f'}} & \mathbf{0} \\ & \mathbf{C}_{\dot{\zeta}} & \\ & \mathbf{C}_\zeta & \end{bmatrix}$$

$$\mathbf{F}_{\zeta_{f'}} = \begin{bmatrix} \frac{\partial \dot{\bar{v}}}{\partial \zeta} & \frac{\partial \dot{\alpha}}{\partial \zeta} & \frac{\partial \dot{q}}{\partial \zeta} & \frac{\partial \dot{\theta}}{\partial \zeta} & 0 \end{bmatrix}^T \tag{5.1}$$

$$\mathbf{C}_{\dot{\zeta}} = \begin{bmatrix} 0 & -\frac{m\bar{V}_t}{L_\alpha b} & 0 & -\frac{\bar{V}_t}{b} & 0 & 0 & 0 \end{bmatrix}$$

$$\mathbf{C}_\zeta = \begin{bmatrix} 0 & 0 & 0 & 0 & 0 & 1 & 0 \end{bmatrix}$$

In Eqs. 5.1, $\mathbf{F}_{\zeta_{f'}}$ is the column vector of vertical formation flight interaction coefficients, the ele-

ments of which are defined in the derivation of the linear model for the trailing airliner in Chapter 3. $\mathbf{C}_{\dot{\zeta}}$ and $\mathbf{C}_{\zeta}$ are the output matrices for vertical separation rate and vertical separation respectively. The new state vector is given by,

$$\mathbf{x_h} = \begin{bmatrix} \bar{v} & n_z & q & \theta & E_C & \zeta & \int_{\zeta_E} \end{bmatrix}^T \tag{5.2}$$

The feedback gains, K_{ζ} and $K_{\int_{\zeta}}$, for the PI-controller are then determined by means of root locus, for both the outer and sandwich regions. The root loci of Fig. 5.3 shows the dominant poles for both the zero vertical separation outer and sandwich regions remain in approximately the same position as that of the system in isolated flight, without redesigning the ζ-controller gains. The loci are very similar, and it is thus expected that the dynamics are similar.

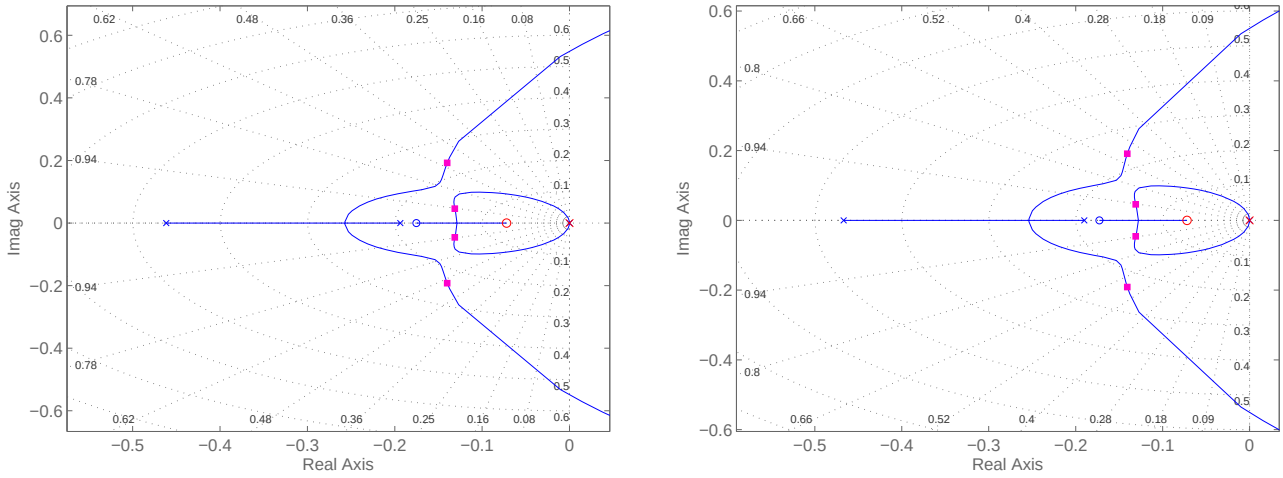

(a) Outer region

(b) Sandwich region

Figure 5.3: Root locus design for ζ-controller in trim trailing positions

The open-loop system is then augmented to incorporate the feedback dynamics of the PI-controller, as follows,

$$\begin{aligned} \mathbf{A}_{\zeta} &= \mathbf{A}_{\zeta_{OL}} - \begin{bmatrix} \mathbf{B}_{\gamma} \\ 0 \\ 0 \end{bmatrix} \begin{bmatrix} 0 & 0 & 0 & 0 & 0 & K_{\zeta} & K_{\int_{\zeta_E}} \end{bmatrix} \\ \mathbf{B}_{\zeta} &= \begin{bmatrix} K_{\zeta}\mathbf{B}_{\gamma}^T & 0 & 1 \end{bmatrix}^T \end{aligned} \tag{5.3}$$

Fig. 5.4 shows the vertical separation step responses for both the non-linear and linearised systems for various trailing positions, for small step inputs. Each plot compares the transients of the design and non-linear simulations. As the design is a PI-controller design, zero steady state error

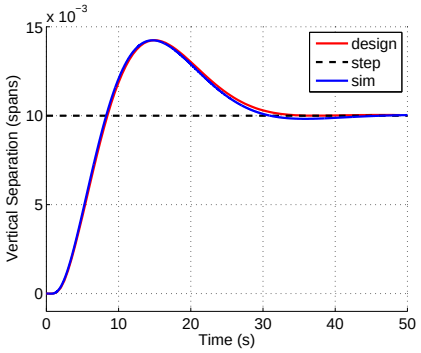

(a) Outer region ($\eta = 1.3$, $\zeta = 0$)

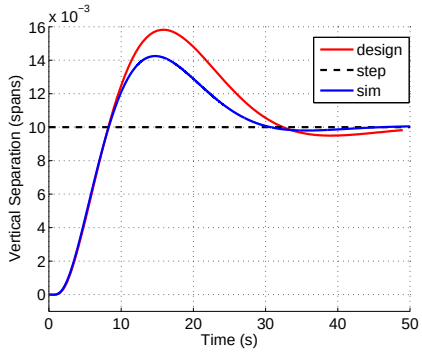

(b) Outer region, alternative ($\eta = 1.3$, $\zeta = 0.5$)

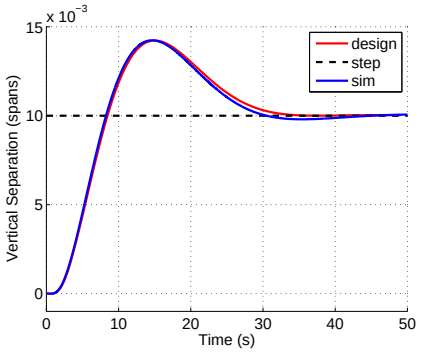

(c) Sandwich region ($\eta = 0.713$, $\zeta = 0$)

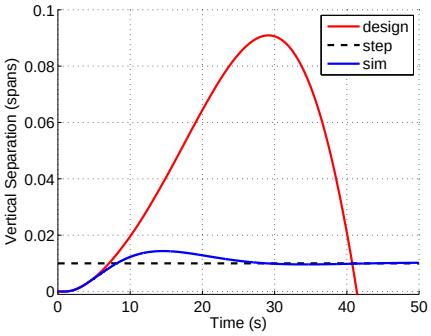

(d) Sandwich region, alternative ($\eta = 0.713$, $\zeta = 0.05$)

Figure 5.4: ζ-controller performance for various trailing positions

is guaranteed, but with large overshoot in the transient response. For zero vertical separation in both the outer and sandwich regions, the non-linear and linear results match very well in both transient response and trim.

However, for non-zero vertical separations, the results begin to differ. This is due to an error of unknown cause in the augmented linear model. Further investigation is required to solve this issue. Fortunately though, significant error is only found in the sandwich region, where the linear model predicts instability at certain vertical separation positions for the same set of feedback gains, as shown in Fig. 5.4d. Note that it is possible to stabilise this linear system with much larger feedback gains, for which greater similarity exists between the linear and non-linear models. However, the sandwich region is not practically feasible for formation flight, and thus the discrepancy is not investigated further in this thesis.

Finally, Fig. 5.5 shows the response for large vertical separation step inputs; this is useful for entering and exiting the wake vertically. For large steps, the integrators hit their limits, and large overshoot and integrator wind-up is prevented, as can be seen in the non-linear step response. The response is very gradual, yet sufficiently fast.

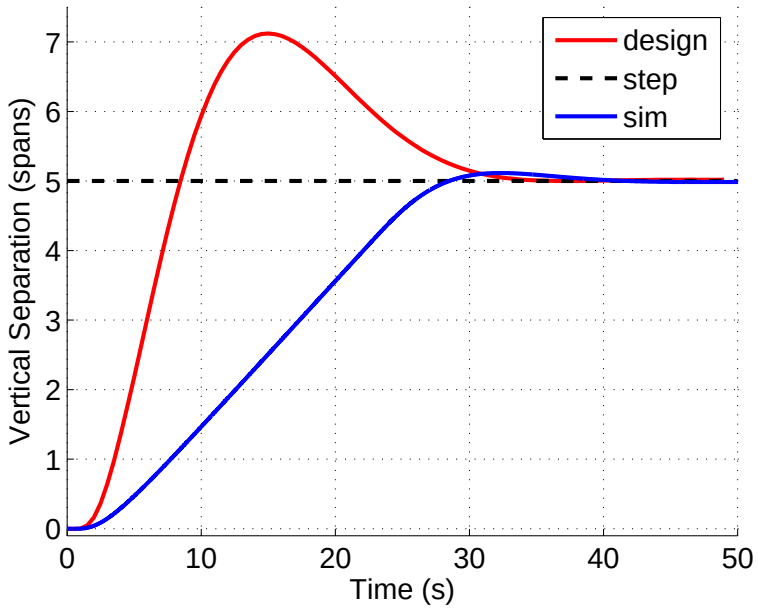

Figure 5.5: Linear vs. non-linear response for large vertical separation step

5.1.2 Longitudinal Separation Controller

The longitudinal separation controller, or ξ-controller is an additional formation flight specific controller, designed to regulate the longitudinal or in-track separation between the leading and trailing airliners. It generates an airspeed reference, and feeds it to the airspeed controller as was designed for conventional case; no adaptations to the conventional airspeed controller is required.

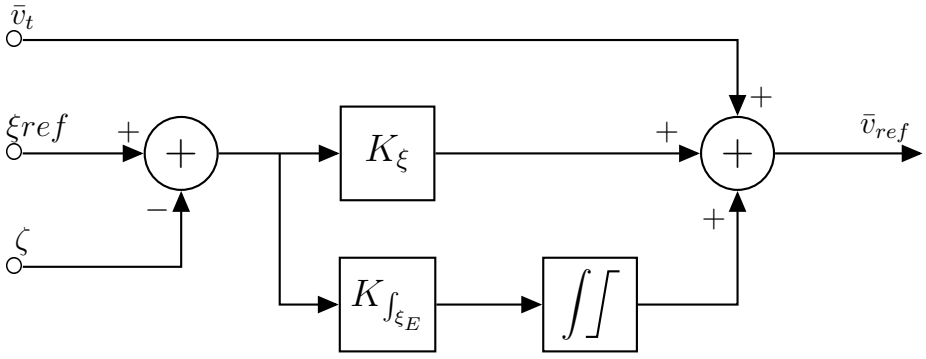

Figure 5.6: Longitudinal separation controller architecture

As shown in Fig. 5.6, the longitudinal separation controller, or ξ-controller, is a simple proportional controller with a limited tracking integrator. Furthermore, it contains trim airspeed feed-forward to limit the reliance on the tracking integrator, and allows a fast response to changes in the

trim airspeed configuration for the formation. Keeping in mind that there are no additional dynamics introduced for longitudinal separation variation in the aerodynamic interaction model, the controller design is kept simple. The gains were designed experimentally through simulation, and the tracking integrator was limited to small outputs of less than $5\,\mathrm{m\,s^{-1}}$, to limit its effects on the system's dynamics.

The ξ-controller would only be of greater interest if its performance was to the detriment of the vertical states, as potential coupling exists between airspeed and vertical states. For this reason, the design priority was not on the ξ-controller, but instead on the ζ- and η-controllers. The airspeed controller however, would need to be sufficiently aggressive to regulate the airspeed tightly, in order to limit coupling with the vertical states. The conventional airspeed controller proved to be sufficient for this purpose.

5.2 Lateral Control

As was done for the vertical controllers, the initial step of the redesign process of the lateral controllers is to adapt the conventional architecture of Fig. 4.13 for formation flight, by remapping the inputs to lateral separation. Both the bank-to-turn and skid-to-turn CT-controllers, designed for isolated flight, are easily adapted to meet the requirements of formation flight. The architectures presented by Figs. 4.22 and 4.28 were designed to regulate cross track distance, normalised to wingspan. The inputs to these controllers would simply be remapped to the desired lateral separation distance η_{ref}, and the measured lateral separation η between the leading and trailing airliners, according to DGPS data. As the decision was made to normalise the conventional cross track measurements to wingspan, unit conversions are not required for the η-controllers.

As was the case for the vertical controllers, the inner-loop controllers need not be redesigned, because the conventional modes are mostly unaffected by the aerodynamic interactions. This was confirmed by initial analyses, that determined that the dynamics were nearly constant without redesigning any of these controllers. The only minor adaptations made were to the outer-loop η-controllers. This will be discussed in more detail in Section 5.2.1. A discussion of the inner-loop controllers is not particularly of interest here, and is omitted from this thesis. Nonetheless, it is worth mentioning that particular DRD designs may conflict with the bank-to-turn strategy controllers. Specifically, DRDs designed with too large gains, or washout filters with too low cut-off frequencies, could undesirably combat the aggressive banking manoeuvres required to maintain formation. This topic is discussed in greater detail in Section 5.2.2.

5.2.1 Lateral Separation Controller

The extended architectures for both the bank-to-turn and skid-to-turn η-controllers are presented in Fig. 5.7; it illustrates an architecture very similar to the conventional CT-controller, but with the addition of a limited tracking integrator to allow for improved tracking performance. The

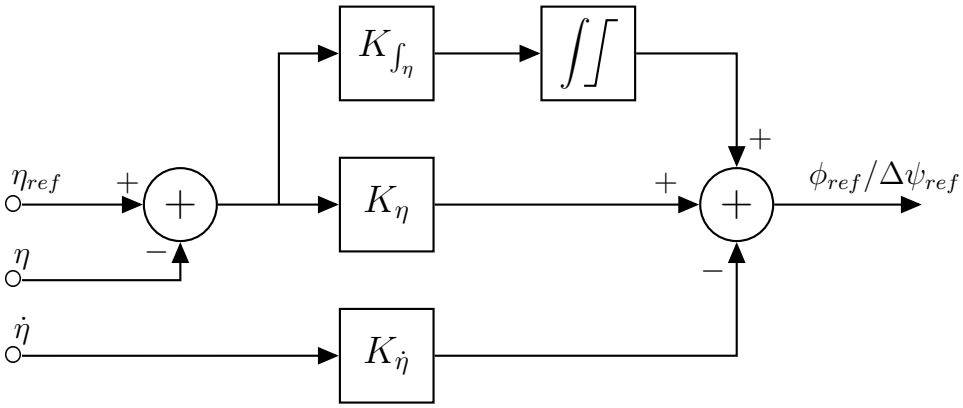

Figure 5.7: Lateral separation controller architecture; bank-to-turn/skid-to-turn strategy

only requirements for this controller to successfully maintain formation, are that the gains are chosen correctly and sufficiently large. Though small gains may be stable according to the linear model, the non-linearity can induce unwanted dynamics. Furthermore, small gains may cause transients and steady-state errors that are too large, allowing the trailing airliner to move into the untrimmable region, causing undesirable behaviour such as limit cycles or instability.

Fig. 5.10a illustrates that there is a steady state error in the lateral separation of formation flying, controlled airliners; and that this is the case for both the conventional- and formation-trimmed trailing airliner – though the error is larger for the conventional-trimmed airliner. This consideration is of concern as it may not be practically feasible or accurate to immediately trim the trailing airliner upon entering the wake vortex, especially considering that this is not an instantaneous manoeuvre. Therefore the tracking integrators will be necessary if finding the exact trim position is of importance.

Furthermore, the integrators could be designed to additionally compensate for large disturbances such as wind and shear, though this is beyond the scope of the current design. The performance of the tracking integrator is captured in Fig. 5.10, where the steady state error is removed by means of the tracking integrator. If finding the trim configuration in order to maintain an exact trim position is not of particular concern however, the integrators may be removed without any significant consequence.

Bank-to-turn strategy

Fig. 5.12a shows the step response for the bank-to-turn strategy controller in the outer region of formation flight. The response of the non-linear simulation matches fairly well with that of the linear design; though as discussed, there is a steady state error in the non-linear simulation without the tracking integrator. Furthermore, when compared to the step response of the system in isolated flight, given by Fig. 4.24a, it is clear that transient response is nearly unchanged, especially in the non-linear simulation.

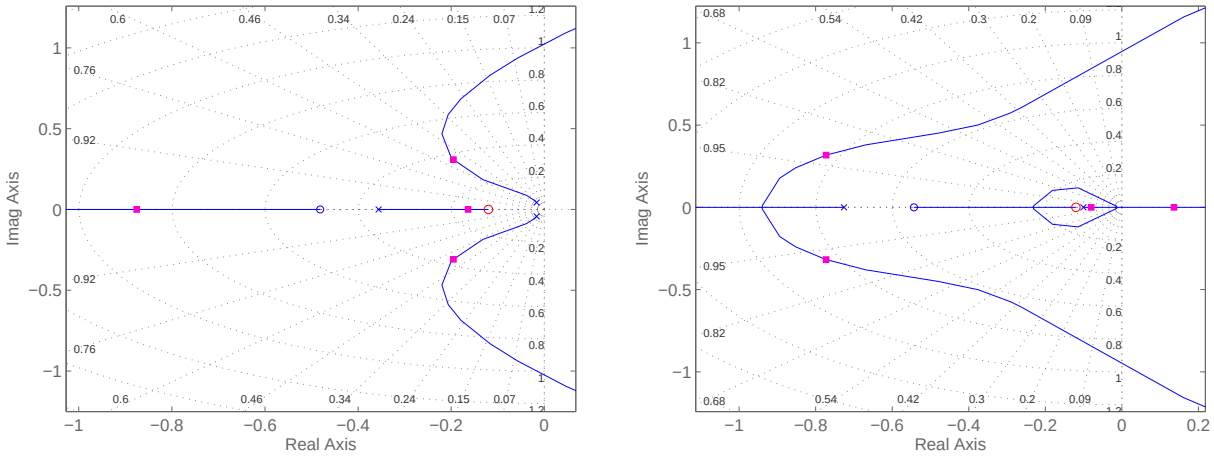

(a) Outer region (b) Sandwich region

Figure 5.8: Root locus design for bank-to-turn η-controller in trim trailing positions

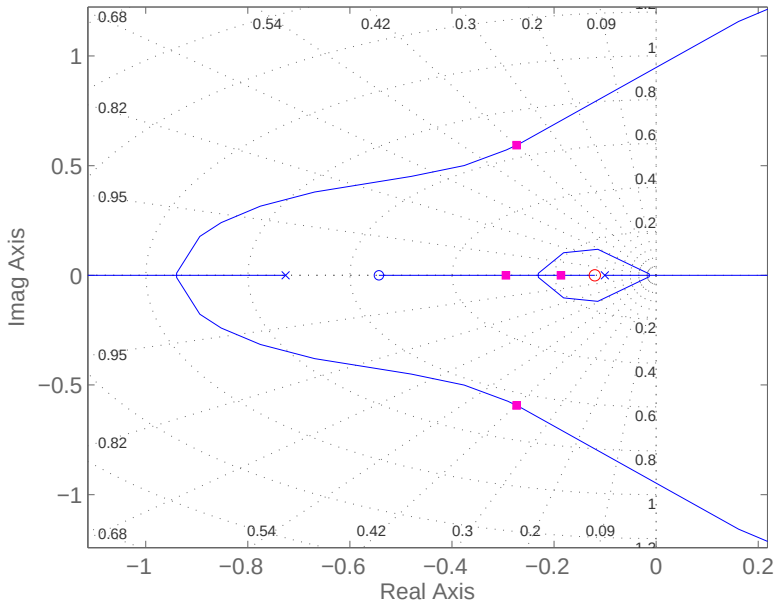

Figure 5.9: Root locus design for bank-to-turn η-controller in sandwich region; redesigned for stability

The consistency in dynamics becomes clear when analysing the root locus design for the bank-to-turn lateral controllers, given by Fig. 5.8. The root locus of Fig. 5.8a shows the positions of the dominant poles in the outer region. For the same feedback gain, these poles, and thus the system dynamics, remain nearly unchanged when compared to the design of the same controller in isolated flight. This is an indication that the controllers need not be redesigned any further for

the purpose of formation flight, and will yield similar dynamics. However, Fig. 5.8b shows that in the sandwich region, the design results in an unstable pole. Nonetheless, it is possible to stabilise the system with larger feedback gains, as is shown in Fig. 5.9. These larger gains are likely too aggressive for the large banking manoeuvres required by conventional flight. Note that these root locus designs for the bank-to-turn lateral controllers were done by augmenting the formation flight extended longitudinal linear model with the inner-loop controllers.

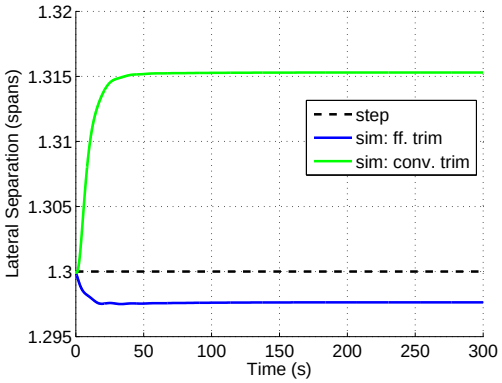

(a) Small steady state error without limited tracking integrator

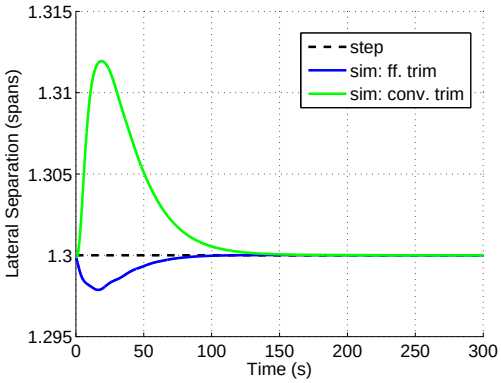

(b) Steady state error cancelled by tracking integrator

Figure 5.10: η-controller steady state tracking performance; bank-to-turn strategy

Skid-to-turn strategy

Next, the process is repeated for the skid-to-turn strategy controllers. Fig. 5.12b shows the step response for this control strategy in the outer region of formation flight. When compared to the step response of the bank-to-turn control strategy, it is clear that the steady state error of the nonlinear system is much smaller; this indicates that there is less of a need for a tracking integrator for the skid-to-turn controller.

As was the case for the bank-to-turn control strategy, the dynamics of the skid-to-turn control strategy remains very similar for isolated flight, and formation flight in the outer region. This is verified by the root loci of Fig. 5.11, showing that the closed-loop dominant poles remain nearly unchanged for both the outer and sandwich regions, compared to that of isolated flight. Further take note that for the sandwich region, the system will become unstable for gains that are too small. This can been seen in Fig. 5.11b, where a branch of the locus crosses into the positive half of the plane.

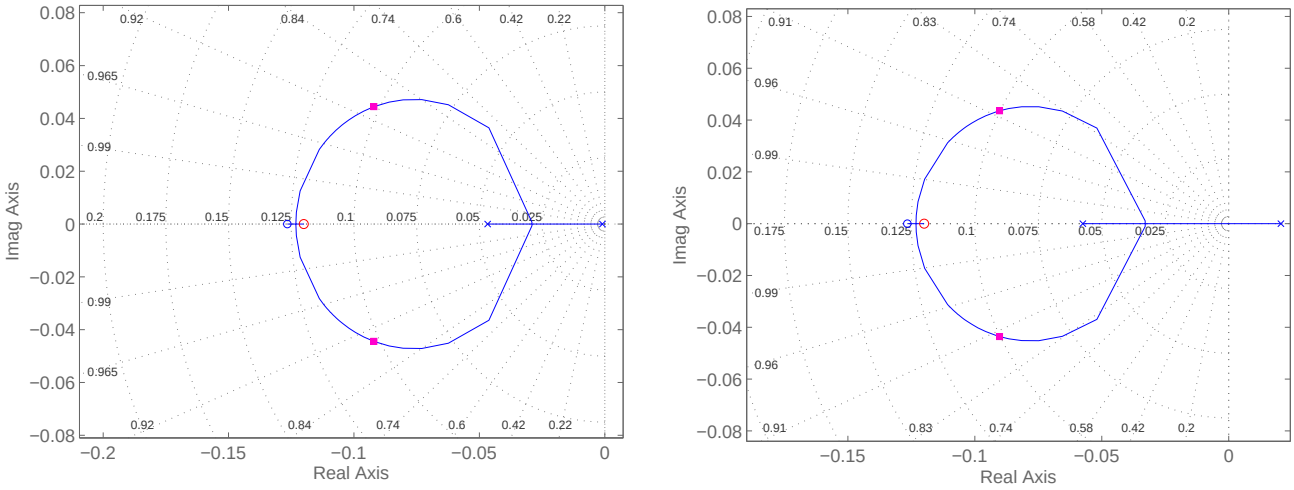

(a) Outer region (b) Sandwich region

Figure 5.11: Root locus design for skid-to-turn η-controller in trim trailing positions

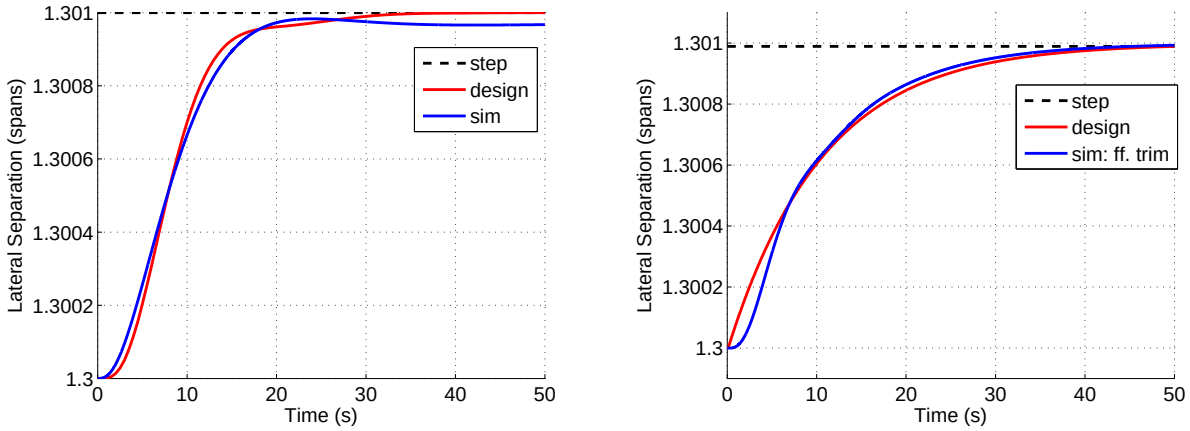

(a) Bank-to-turn strategy (b) Skid-to-turn strategy

Figure 5.12: Step responses of η-controllers in outer region

5.2.2 Effect of Dutch Roll Damper on Station-Keeping Performance

The Dutch roll damper is an essential part of the flight control system, as the interaction between roll and yaw states can cause stability issues in the form of Dutch roll. For the B-747 model used in this thesis, the Dutch roll is naturally stable, thus the DRD is perhaps less essential. As discussed in Section 4.2.1 however, the DRD is still useful for damping highly underdamped Dutch roll oscillations. The $\Delta\psi$-controller of the skid-to-turn control strategy however includes yaw rate feedback, and does thus not have a dedicated DRD. As such, this discussion only concerns the bank-to-turn control strategy.

It was discovered that the DRD can introduce a performance penalty for the trailing airliner in formation flight. A possible reason for this is that the formation flight controllers are aggressive, and operate at a higher frequency than what is required for ordinary flight. Consequently, the washout-filter becomes less effective at preventing the DRD from combating intended banking manoeuvres. Extended non-linear simulations in conditions of severe turbulence showed that the DRD, as was designed in Section 4.2.1, interferes with station-keeping correction manoeuvres too aggressively. Fig. 5.13 compares the station-keeping performance results of the ordinary DRD system, with that of a system where the DRD is completely absent. It is apparent that the system with the ordinary DRD of Fig. 5.13a, performs worse when comparing the maximum deviation from trim tracking position, to that of the DRD-less system. The DRD-less system however contains smaller oscillations of higher frequency that likely corresponds to Dutch roll.

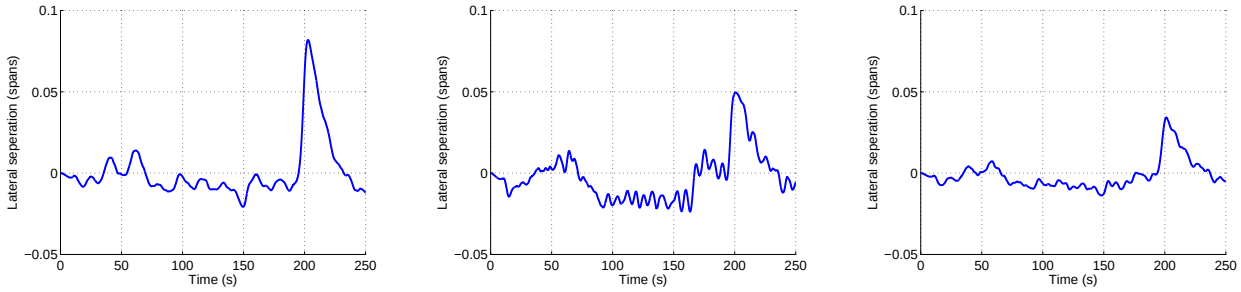

(a) Normal DRD system

(b) DRD-absent system

(c) Formation-flight redesigned DRD system

Figure 5.13: Station-keeping performance comparison for various DRD systems, measured relative to trim.

Nonetheless, it is not ideal to completely remove the Dutch roll damper, as it is a standard component used in industry. It is conceivable that it should in fact aid in combating turbulence, and thus improve station-keeping performance, if designed correctly. The DRD was iteratively tuned to about a quarter of the original gain, which yielded better results as shown in Fig. 5.13c.

5.3 Additional Control Structures for Formation Flight

Subsequent to the design and verification of a set of functioning flight controllers capable of station-keeping in formation flight, additional structures are investigated to further extend functionality and improve safety and performance. The main function of these structures is to aid in preventing the trailing airliner from entering the untrimmable regions of formation flight. Additionally, they should limit the magnitude of aggressive manoeuvres, to aid in ensuring passenger comfort and safety. Finally, a basic state machine architecture is suggested, to aid in scheduling the phases of formation flight, such as entering, maintaining or exiting formation.

5.3.1 Lateral Motion Limiters

The first lateral motion limiting element that will be discussed is the heading difference limiter, or $\Delta\psi$-limiter. The $\Delta\psi$-limiter is a non-linear lateral controller component which attempts to prevent the trailing airliner from exceeding a certain heading difference threshold relative to the leading airliner. The motivation behind the need to limit heading difference, is that an excessive heading difference during a η-step manoeuvre at small lateral separations will necessarily cause overshoot. The airliner executing the η-step requires sufficient time to recover the heading difference to zero as it reaches the end of the η-step. If the heading difference is too large however, it may be impossible for the airliner to do so without overshooting the η-step. For a η-step towards the trailing vortex, overshoot could cause the trailing airliner to enter too deeply into the vortex core, and enter the untrimmable region. This problem exists for both the skid-to-turn and bank-to-turn control strategies, but poses a unique problem for each.

Firstly, the skid-to-turn control strategy faces an additional problem for large η-steps besides the one discussed previously. Specifically, large rudder deflections induce rolling moments, and as such can cause the airliner to bank. For the skid-to-turn controller, this is something that needs to be avoided, as it will conflict with the roll angle controller, and the system may limit cycle or become unstable. The first apparent solution to this problem is to simply limit the rudder deflection command generated by the $\Delta\psi$-controller. However, the rudder deflection command has to be limited to such an extent that it introduces another problem: the effectiveness of the rudder is reduced so much that it cannot effectively regulate heading difference any more. In fact, for large η-steps, overshoot is introduced which may previously not have existed. This overshoot may in fact be so large that the system becomes unstable.

Thus, to overcome this problem effectively, the heading difference command needs to be limited, and not the rudder deflection command. By limiting the reference to the $\Delta\psi$-controller, it is guaranteed that the rudder deflection will not exceed a certain threshold, assuming small yaw rates. Furthermore, as the heading difference is limited, the η-step response for any step size will be guaranteed not to overshoot, and thus will not limit cycle or become unstable, as discussed previously. The $\Delta\psi$-limiter for the skid-to-turn strategy is thus a simple saturation element on the output of the η-controller.

The $\Delta\psi$-limiter of the bank-to-turn control strategy however, is more complex. As there is no $\Delta\psi$-reference generated anywhere in the lateral control loops, it is not straight forward to limit this signal. To overcome this problem, a non-linear, logic component is added at the output of the η-controller to manipulate the ϕ-reference to limit the heading difference. The component works with an algorithm, given by Eq. 5.4, that determines whether the heading difference has exceeded the threshold; and whether the supplied ϕ-reference would reduce the heading difference, or increase it. For the former case, the ϕ-reference is passed through the component unchanged; for the latter, the ϕ-reference is set to 0°. Note that this component is thus not capable of actively correcting excessive heading differences, such as in the case of external disturbances or large initial heading differences; though it is capable of preventing the η-controller from inducing an excessive heading difference.

$$
\begin{aligned}
&\Delta\psi = \psi_{trail} - \psi_{lead} \\
&\phi_{ref,out} = \phi_{ref,in} \\
&if \quad |\Delta\psi| \; > \; \psi_{max} : \\
&\qquad if \quad (\Delta\psi > 0 \;\; \& \;\; \phi_{ref,in} > 0) \;\; | \;\; (\Delta\psi < 0 \;\; \& \;\; \phi_{ref,in} < 0) : \\
&\qquad\qquad \phi_{ref,out} = 0
\end{aligned}
\tag{5.4}
$$

The bank-to-turn strategy controllers have an additional problem: for moderate lateral separation step sizes, the performance degrades with excessive roll angle sizes. As the lateral controllers are very aggressive to allow for good performance around straight and level trim, large roll angles are commanded quickly for moderate and large step sizes. For large step sizes, the roll angle will be commanded to zero by the $\Delta\psi$-limiter to maintain a constant, maximum heading difference. As it approaches the desired lateral separation, it begins to bank in the opposite direction to reduce the lateral separation rate to zero. For moderate step sizes however, the airliner reaches the point where it needs to start banking in the opposite direction, to reduce lateral separation rate, before the $\Delta\psi$-limiter has regulated the roll angle to zero.

Therefore, an extra large bank angle step needs to be executed, which cannot be done sufficiently fast to prevent the lateral step from overshooting, taking into account the rate limiters on the ailerons. To overcome this problem, a saturation element is added to the input of the ϕ-controller, limiting the maximum commanded bank angle command to a reasonably smaller value. The saturation element does not have to be symmetrical, and only needs to significantly limit the bank angle towards the wake vortex. This acts as an additional layer of safety, as the trailing airliner cannot be aggressively banked towards the wake vortices, but can rapidly exit the wake if required.

5.3.2 State Machine Controller

The state machine is a system that guides the trailing airliner through the various stages of formation flight, including initiation, station-keeping at various trailing positions, ordinary formation disengaging, and emergency disengaging. The state machine is a rich topic worth researching for a future projects related to formation flight, however, formation initiation will be focused on in this thesis. Furthermore, the station-keeping state will simply encapsulate the separation-tracking controllers as discussed throughout this chapter.

During the initiation phase, the state machine will safely guide the trailing airliner into a position nearby the leading airliner, assuming non-conflicting paths. In a system where higher bandwidth communication is allowed between the leading and trailing airliners, the leading airliner may execute manoeuvres to facilitate this process. In this thesis however, it is assumed that the leading airliner follows a constant, straight-and-level track, independent of the trailing airliner.

Furthermore, it is possible to initiate formation flight vertically, from either above or below; or laterally, steadily decreasing the lateral separation. Vertical initiation has the benefit that any

overshoot during the initiation manoeuvre will not cause the trailing airliner to move further inboard of the trailing vortices, and thus has no risk of entering the untrimmable region. However, a properly, slow-and-steady executed lateral initiation manoeuvre could also minimise this risk sufficiently. The lateral motion limiters discussed in the Section 5.3.1 aims to aid in this, however, it should ideally still be done through an initiation state.

Fig. 5.14a shows the simulation results for the vertical separation procedure. The airliners were initialised with vertical, lateral and longitudinal separations of 10 wingspans, and aligned heading vectors. During the initiation procedure, the trailing airliner approaches a trailing separation of 3 wingspans below the final trailing separation. Thereafter, once the vertical, lateral and longitudinal separations have settled and have been within reasonable bounds for a certain period of time (approximately 40 seconds for this simulation), the controller enters the station-keeping state, and the separations are regulated to their final station-keeping values. Fig. 5.14b shows the lateral separation initiation procedure; note that the intermediate step of aligning vertical and longitudinal separation was omitted for this simulation, and the trailing airliner had been initiated with final vertical and longitudinal separations, and increased lateral separation.

Lastly, note that these initiation procedures were chosen without significant consideration of factors such as safety, passenger comfort and fuel consumption; but only intend to demonstrate that the initiation of formation flight using the designed controllers is possible. Further study is required to determine which strategy is the most appropriate for formation flight initiation; which may include strategies which are more complex than the procedures presented here.

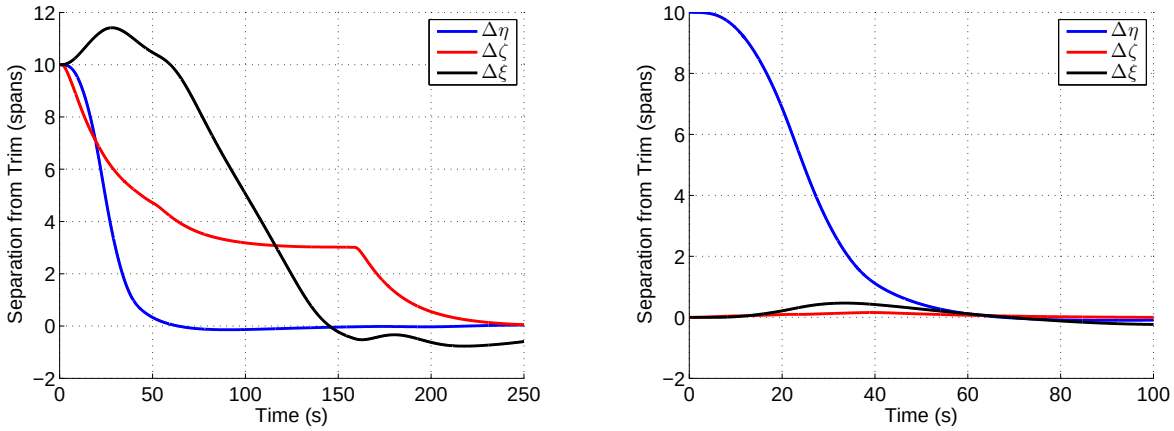

(a) Vertical initiation from below

(b) Direct lateral initiation

Figure 5.14: Initiation procedures simulation results

5.4 Controller Robustness Analysis

An analysis is done to verify that the controller is robust in its stability and dynamics for sensible operating ranges about the discussed trim trailing positions. These ranges correspond to 0.1

wingspans separation about the various trailing positions, which is proven to be sufficient in the non-linear simulations of Chapter 6. The analysis is done by plotting root loci for lateral and vertical separation variations about the analysed trim trailing positions. For the controller to be robust, the branches need to stay on the left-hand side of the plane for stability, but it is also desirable that the dynamics stay fairly constant. Furthermore, the poles for the controlled airliner in isolated flight will also be included in the plots to highlight any differences in dynamics for the controlled airliner in formation flight and isolated flight.

5.4.1 Outer Region

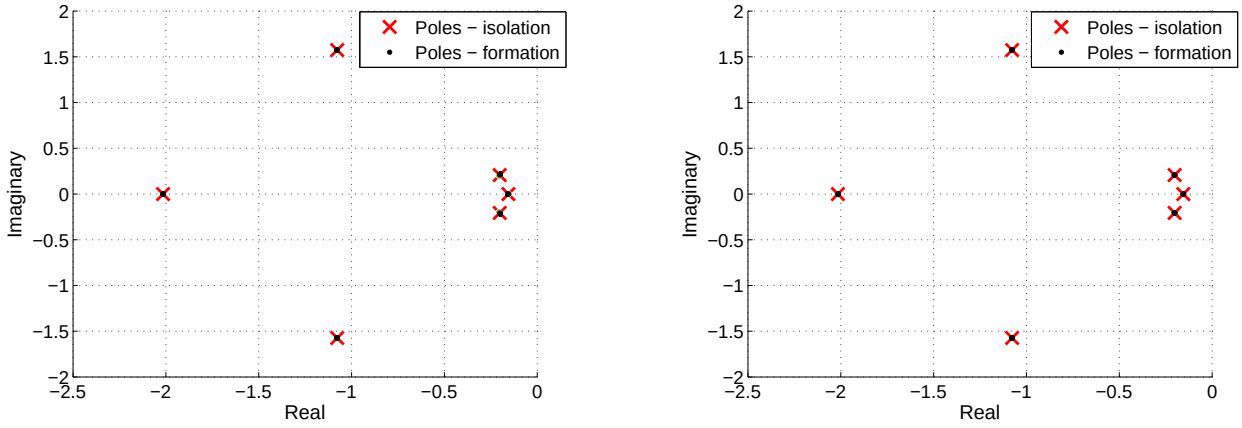

(a) Vertical separation variation

(b) Lateral separation variation

Figure 5.15: Separation variation root loci for closed-loop longitudinal system in outer region

Figs. 5.15-5.17 show the results of the robustness analysis for the closed-loop longitudinal and lateral systems, operating in the outer region, for both vertical and lateral separation variation. It is evident that the change in dynamics is negligible over practical operating separation ranges, and that the systems will remain stable. Furthermore, the dynamics of the closed-loop systems in the outer region resembles the dynamics of the closed-loop systems in isolated flight effectively identically.

5.4.2 Sandwich Region

Figs. 5.18 and 5.19 show the analysis done for the closed-loop system for the trailing airliner flying within the sandwich region. Fig. 5.18a shows that, for certain small vertical separation values, the fully augmented linear model predicts instability of the closed-loop system; though, as previously discussed, this is an error in the linear model, which is not reflected in the full non-linear simulations. The other root loci predict that the stability stays nearly constant for separation variation, which matches with the results of full non-linear simulations. The analysis of

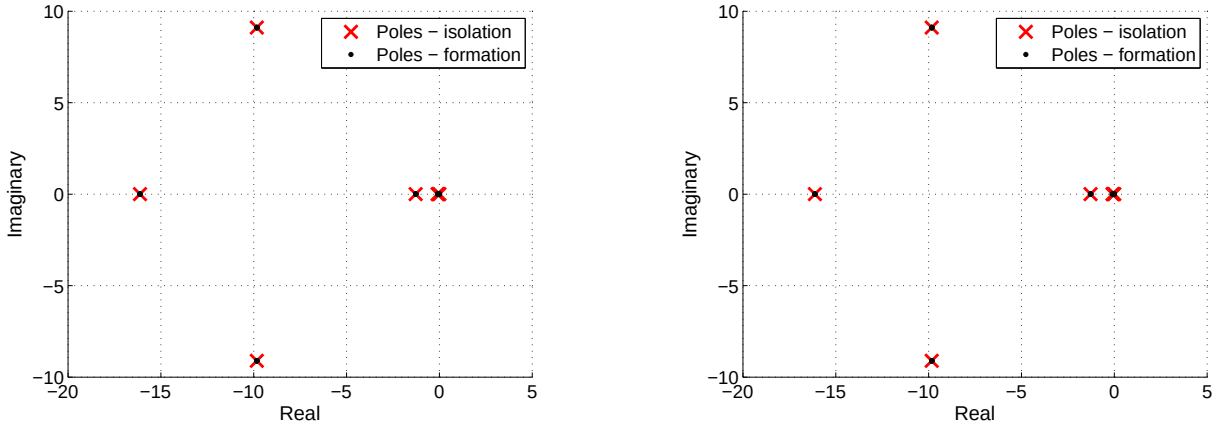

(a) Vertical separation variation

(b) Lateral separation variation

Figure 5.16: Separation variation root loci for closed-loop bank-to-turn lateral system in outer region

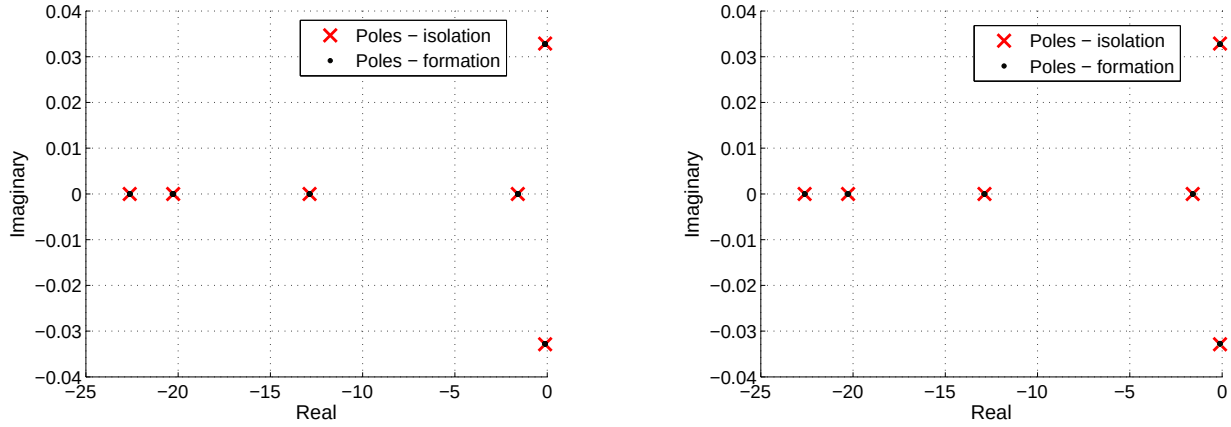

(a) Vertical separation variation

(b) Lateral separation variation

Figure 5.17: Separation variation root loci for closed-loop skid-to-turn lateral system in outer region

the lateral system was done for both the skid-to-turn and bank-to-turn control strategies, though only the results of the analysis using the skid-to-turn strategy is shown in Fig. 5.19.

5.5 Conclusion

Research objective (7) was addressed by extending the conventional controllers, designed in Chapter 4, to allow the trailing airliner to track a position relative to the leading airliner in formation

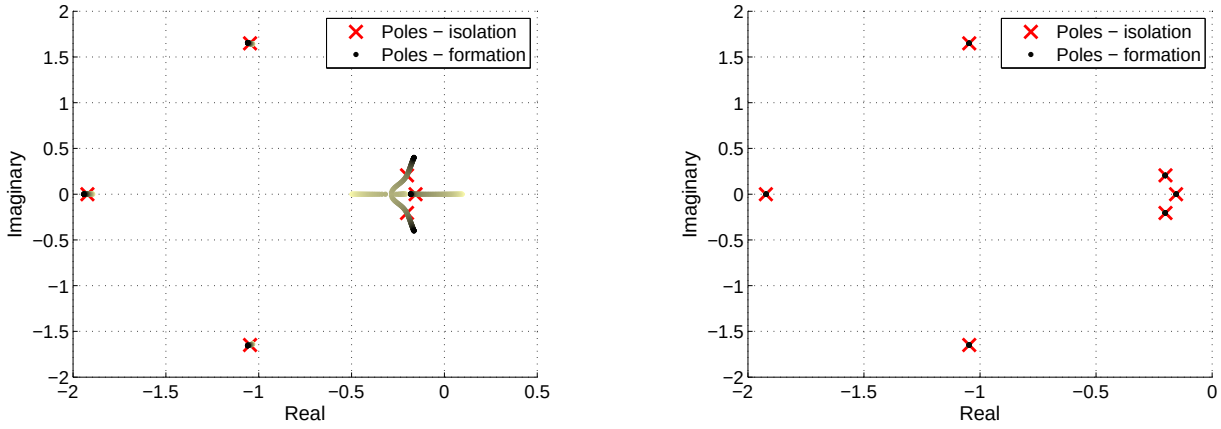

(a) Vertical separation variation

(b) Lateral separation variation

Figure 5.18: Separation variation root loci for closed-loop longitudinal system in sandwich region

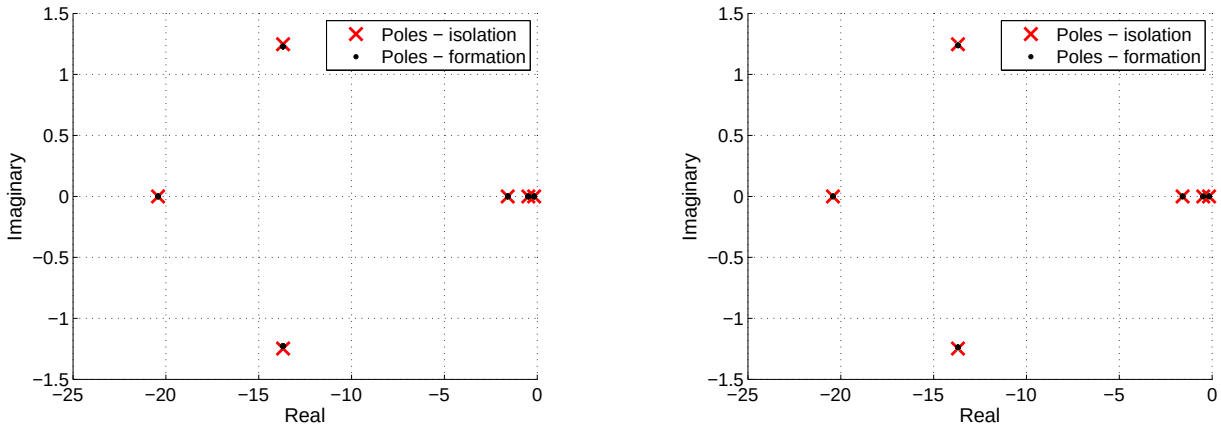

(a) Vertical separation variation

(b) Lateral separation variation

Figure 5.19: Separation variation root loci for closed-loop lateral system in sandwich region

flight. The performance of these controllers were analysed and found to be adequate for station-keeping in the outer region of formation flight, partially addressing research objective (8). Limited integrators were added to the outer vertical and lateral separation loops to improve tracking performance. It was determined that no architectural change or redesign of the control laws were required to the inner-loop controllers; and that there would be no significant change in dynamics for formation flight compared to isolated flight.

Subsequently, the performance of the trailing airliner in the sandwich region was investigated. For the bank-to-turn control strategy, it was found that the conventional gains are insufficient to stabilise the system. The skid-to-turn control strategy however, was found to be stable with negligible change in dynamics within the sandwich region. The non-linear simulations however uncovered that too small feedback gains would allow for large transients and steady state errors,

causing the trailing airliner to leave the sandwich region and enter an untrimmable region, causing effective instability. Larger feedback gains, as well as the addition of tracking integrators helped resolve this issue, successfully allowing formation flight within the sandwich region, in conditions of clean air without turbulence.

Next, the effect of the Dutch roll damper on the trailing airliner's performance was investigated. It was found that the DRD would degrade the system's performance in turbulent conditions if the gains were too large. The gains were thus iteratively tuned to nearly a quarter of the original value, for which the tracking performance proved to be significantly better.

Lateral motion limiters were added to improve the performance quality by reducing overshoot and aiding in the stability of the system by ensuring that the system operates within the scope of the design. These include saturation limits on the $\Delta\psi$-controller and the ϕ-controller, but also a more complex element which prevents the bank-to-turn controllers from causing an excessive heading difference. Next, a state machine was added to guide the trailing airliner through the various stages of formation flight, such as initiation, station-keeping, and scheduled and emergency disengaging from the formation.

Finally, a robustness analysis confirmed that the addition of the controllers managed to stabilise the system in the outer and sandwich regions, addressing research objectives (4) and (6). However, for certain non-zero vertical separations within the sandwich region, the model predicts instability, which is not reflected in full non-linear simulations. This is likely due to an unknown flaw in the derivation of the model, or augmentation of the flight controllers. This error only presents itself significantly in the sandwich region, and thus it was not investigated further. Furthermore, the robustness analysis proved that the controllers managed to regulate both the lateral and longitudinal dynamics of the system very well within the outer region.

Chapter 6

Extended Simulations

Numerous non-linear simulations were run in order to test different aspects of the system; particularly the tracking performance, as well as the performance of the engines and control surfaces. This was done throughout the design process, and for different following positions; but only the most relevant results will be discussed here, in particular focusing on the outer trim region. Where applicable, the leading airliner will be used as benchmark for comparison as it is analogous to a conventional airliner in isolated flight. The simulations were done for varying levels of turbulence, since turbulence was not explicitly considered during the design process. The desired outcome is to determine whether the designed control systems still function as expected in more realistic, or even in extreme, atmospheric conditions.

6.1 Tracking performance

Throughout the design of the lateral and vertical separation controllers in Chap. 5, non-linear simulations were done to verify that the tracking performance of the trailing airliner was acceptable, and that it matched with the design. These simulations however, did not include atmospheric turbulence; and as such, these extended simulations intend to evaluate the performance of the controllers in turbulent conditions.

Fig. 6.1 shows the tracking performance of the trailing airliner in moderate turbulence conditions. The separations measured are instantaneous, physical separation between the trailing and leading airliners, normalised to wingspan; and can be thought of as DGPS measurements. The lateral and vertical separation tracking performance is better than expected, and is kept far within bounds of 0.025 wingspans at all times. The scale of -0.1 to 0.1 wingspans was chosen to illustrate the success in maintaining the lateral and vertical separations tightly.

The longitudinal tracking performance is not as good, but this is due to the slow engine dynamics, and much less aggressive control in order to reduce dynamic engine throttling. Furthermore, it is more acceptable to have less aggressive longitudinal tracking performance, as the gradients of

induced moments and forces is much lower along the longitudinal axis. Too large deviations of vertical and lateral separation from trim with respect to the wake has the consequence of either leaving the wake, or entering the untrimmable region of the vortex core too deeply. No equivalent risk exists for the deviation from the longitudinal separation trim, as long as it maintains sufficient distance from the leading airliner to reduce risk of collision.

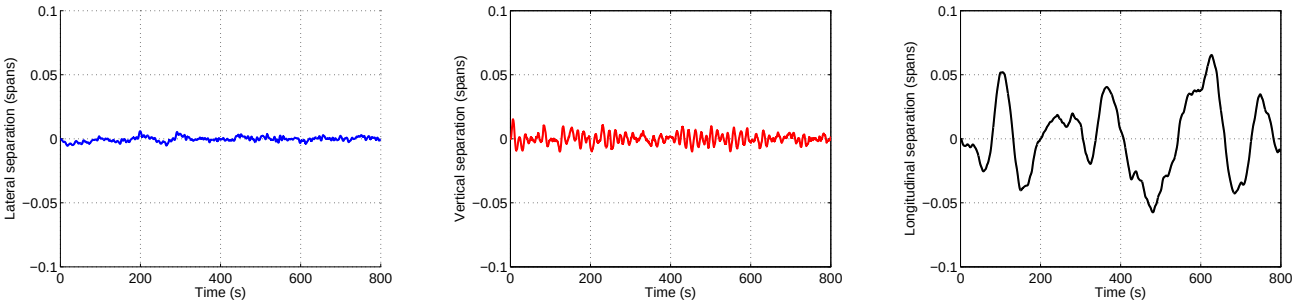

(a) η-tracking (b) ζ-tracking (c) ξ-tracking

Figure 6.1: Instantaneous separation tracking performance of trailing airliner in moderate turbulence

Fig. 6.2 shows the tracking performance results of the above simulation repeated, but with severe turbulence. This level of turbulence would rarely be encountered in actual flights, and formation flight will likely be disengaged for safety reasons. This level of turbulence however provides a more interesting challenge, and thus the simulations were included to illustrate the success of the design. There is much greater deviation from trim for both lateral and vertical separation; the lateral separation especially shows large peaks of deviation which could be very uncomfortable for passengers. The controllers however manage to recover without leaving the wake.

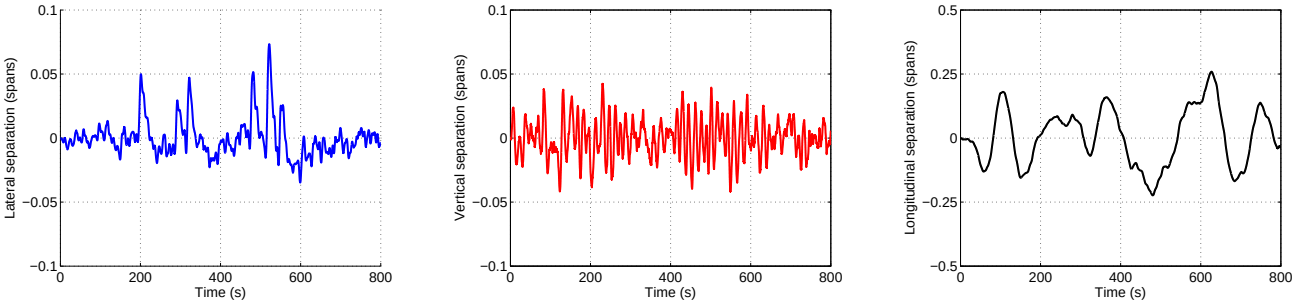

(a) η-tracking (b) ζ-tracking (c) ξ-tracking

Figure 6.2: Instantaneous separation tracking performance of trailing airliner in severe turbulence

Note that the simulations of Fig. 6.1 were done using the bank-to-turn control strategy for lateral separation regulation. Fig. 6.3 compares the lateral separation tracking performance of the bank-to-turn and skid-to-turn control strategies in moderate and severe turbulence. The tracking performance of the two control strategies appears to be comparable in moderate turbulence; though

the tracking performance of the skid-to-turn control strategy appears to be slightly better than that of the bank-to-turn controller in severe turbulence. A passenger comfort study is required to reveal if there is any benefit of one over the other in this regard.

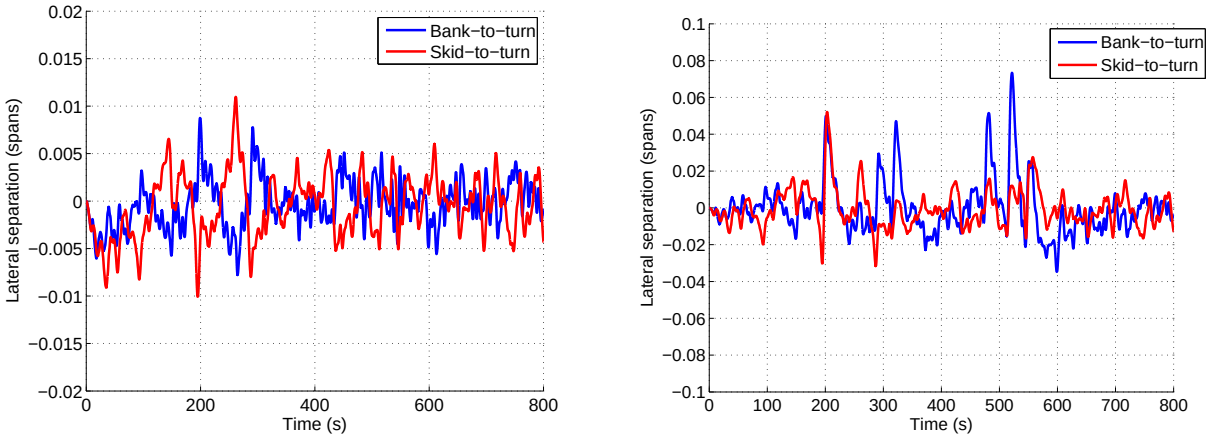

(a) Moderate turbulence

(b) Severe turbulence

Figure 6.3: Bank-to-turn vs. skid-to-turn lateral separation tracking performance

Figs. 6.4 and 6.5 show the effective separation for simulations of moderate and severe turbulence respectively. The effective separation is the separation measured from the trailing airliner to the vortex core. This is relevant, as it is this distance that effectively determines the induced forces and moments on the trailing airliner. The variance and magnitudes of the effective separation are much larger than those of the instantaneous separation, as the vortex is also displaced by turbulence. It is evident that the effective separation is completely dominated by the wake's displacement due to turbulence, rather than the inability of the controllers to track the instantaneous separations.

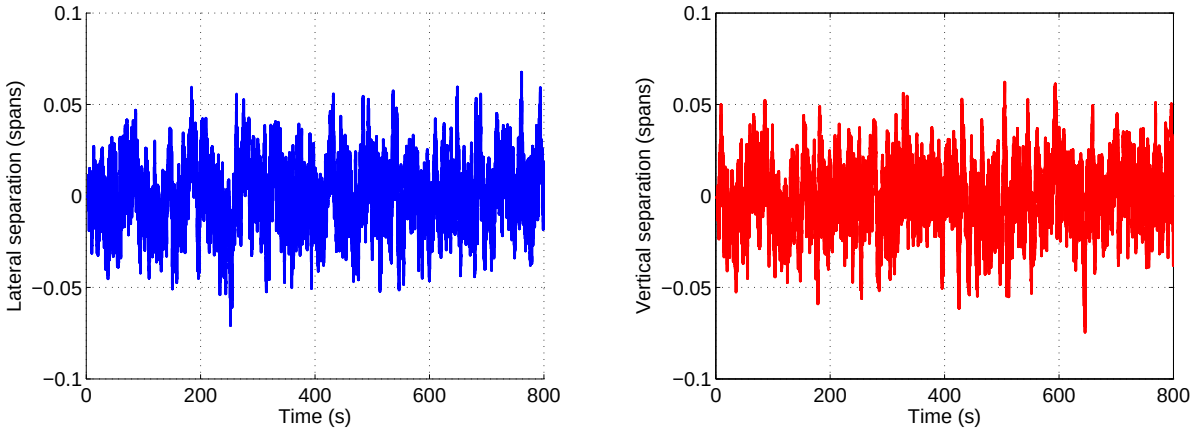

(a) Effective lateral separation

(b) Effective vertical separation

Figure 6.4: Effective separations in moderate turbulence

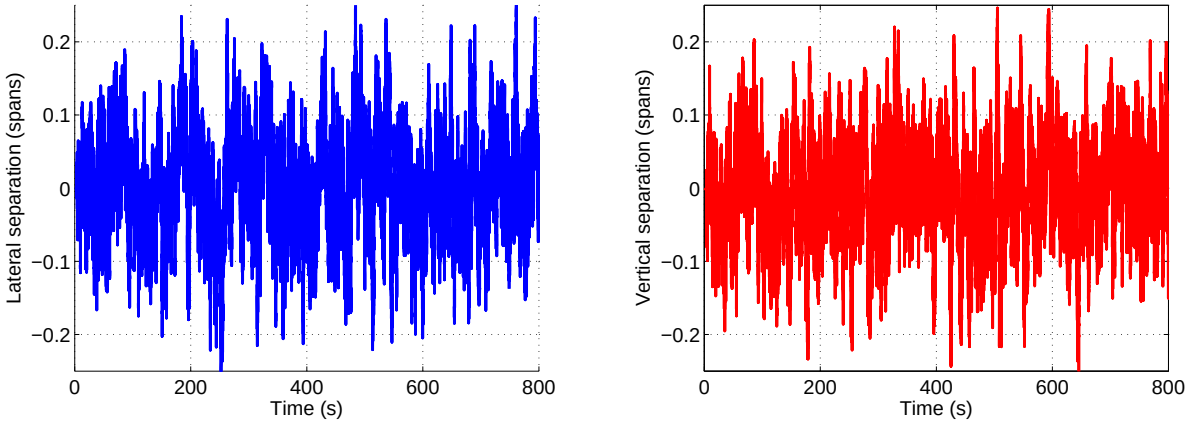

(a) Effective lateral separation

(b) Effective vertical separation

Figure 6.5: Effective separations in severe turbulence

Finally, Fig. 6.6 shows the tracking performance of both the bank-to-turn and skid-to-turn control strategies during extended, 1 hour long simulations in severe turbulence. It is evident that the skid-to-turn strategy performs better as it has much smaller peaks in lateral separation deviation from trim compared to those of the bank-to-turn strategy. Furthermore, no failures were observed during the simulations for either strategies. The controllers successfully managed to keep the trailing airliner within the wake throughout the extended simulations.

6.2 Engine and actuator performance

Besides the separation tracking performance, the engine and actuator performance are important metrics to consider. The trim analysis done in Chapter 3 gives an indication of how the mean engine and actuator settings compare to those of the conventional airliner in isolation. This is an especially important consideration, as it relates to fuel consumption. The relationship between engine setting and fuel consumption was not determined in this thesis however. The variation around the trim is an important consideration as well. Also note that the dynamic throttling of the engines will likely result in higher fuel consumption.

Furthermore, large variation in control surface deflections would result in greater energy expenditure, and would result in greater wear of the actuators. It is desirable that these variations are kept to a minimum, and that they are at least comparable to those of the conventional airliner.

Fig. 6.7 shows the throttle setting of the trailing airliner compared to that of the leading airliner. During this simulation, the leading airliner performed a descending manoeuvre followed by an ascending manoeuvre. The trailing airliner attempts to regulate the instantaneous separation during these manoeuvres, and has a similar profile in throttle setting compared to that of the leading airliner. No real increase in dynamic throttling of the trailing airliner is visible during this

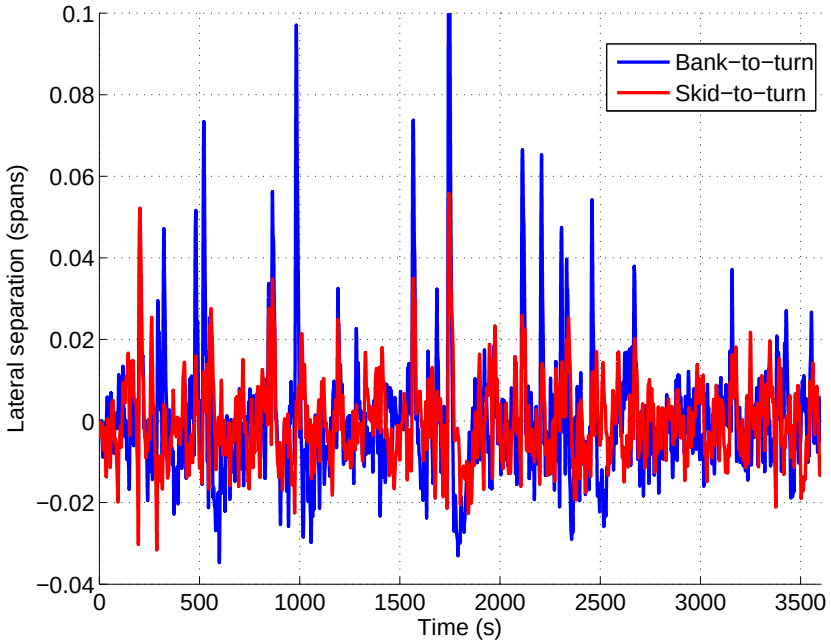

Figure 6.6: Instantaneous lateral separation tracking performance over 1-hour severe turbulence simulation

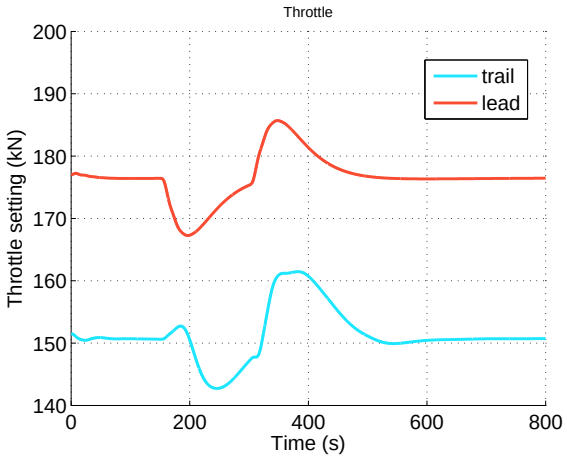

Figure 6.7: Throttle setting: leading airliner vs. trailing airliner

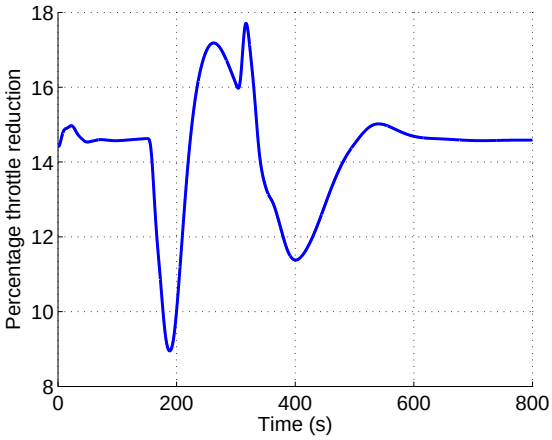

Figure 6.8: Time-wise percentage throttle reduction of trailing airliner

clear air simulation. Further, note that the trailing airliner approximately has a throttle setting reduction of just under 15% compared to that of the leading airliner in steady-state.

Furthermore, Fig. 6.9 also shows the throttle setting of trailing airliner compared to that of the leading airliner; however, the simulation was executed with moderate turbulence conditions, and

the leading airliner did not execute any manoeuvres. As expected, the trailing airliner still has a large reduction in throttle setting compared to the leading airliner, however, the dynamic throttling of the trailing airliner is considerably greater than that of the leading airliner. This could have implications for fuel consumption reduction, as dynamic throttling could potentially increase fuel consumption.

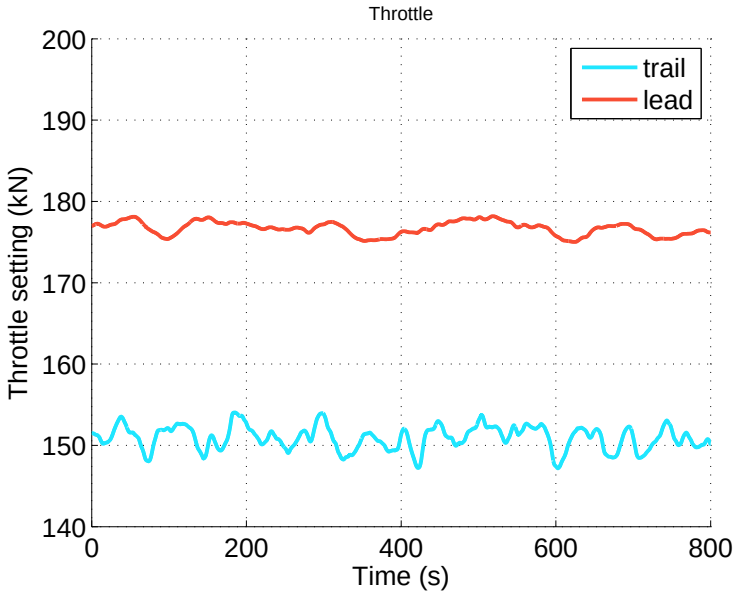

Figure 6.9: Throttle setting: leading airliner vs. trailing airliner in moderate turbulence

Fig. 6.10 shows the control surface deflections of both leading and trailing airliners for a simulation with moderate turbulence. As expected through the trim analysis, the leading airliner has mean aileron and rudder deflections of 0°, whereas the trailing airliner has mean corresponding deflections of approximately 11° and 0.3° respectively. The mean elevator deflections are nearly equal for the leading and trailing airliner, at approximately 3.5° deflection.

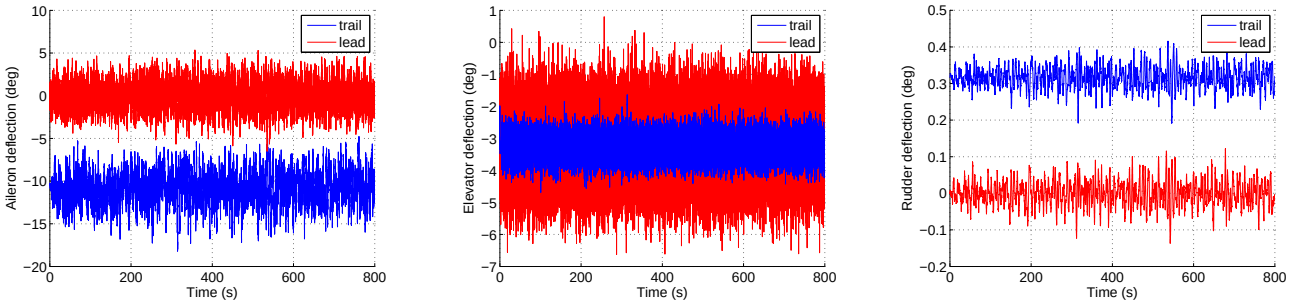

(a) Aileron deflection (b) Elevator deflection (c) Rudder deflection

Figure 6.10: Control surface deflections over the course of a simulation with moderate turbulence

It is interesting to note that the trailing airliner does not have a consistently greater standard deviation in control surface deflections compared to the leading airliner. It was expected that the trailing airliner would use its control surfaces more extensively, with greater standard deviations for the control surface deflections. This was expected as the trailing airliner experiences more severe turbulence, as the turbulent wake vortices induce forces and moments on the trailing airliner in addition to the normal atmospheric turbulence [3].

A possible explanation for this surprising result however, is that it is due to the time-delayed coupling of the turbulence experienced by the leading and trailing airliners. If the formation is displaced from the desired flight trajectory as a group, the physical separation between the airliners in the formation is small compared to the separation between the formation and the trajectory. As it is the formation leader's responsibility to regulate the entire formation, its actuators does more work to overcome the atmospheric turbulence and maintain a straight and level path. This result is especially visible in the elevator deflection comparison in Fig. 6.10b. The trailing airliner however, has a greater variance in aileron deflection; likely due to the particularly powerful induced rolling moments. Table 6.1 shows the standard deviations for the control surface deflections for the moderate turbulence simulation.

Control surface	**Leading airliner**	**Trailing airliner**
Aileron	1.48°	1.88°
Elevator	0.86°	0.33°
Rudder	0.035°	0.03°

Table 6.1: Control surface deflection standard deviations for moderate turbulence simulation

The control surface deflections for the trailing airliner compare acceptably well, and within an order of magnitude, to those of the conventional controllers designed in this thesis. This comparison is not conclusive however, as the conventional controllers use essentially the same architecture and control laws as that of the trailing airliner. For a more thorough, fair comparison, additional detail of current, real fly-by-wire architectures and control laws need to be known and included.

6.3 Conclusion

The extended simulations prove that the designed controllers successfully maintain formation, even in conditions of severe turbulence – addressing research objective (8). In moderate to light turbulence, instantaneous separation is tracked very tightly – easily within bounds of 0.025 wingspans for lateral and vertical separation. Longitudinal separation is tracked less tightly, as the controllers are designed to be less aggressive to avoid excessive dynamic throttling. Even so, the trailing airliner experiences greater dynamic throttling in turbulent conditions, of which the effects still need to be studied in further detail. Passenger comfort should also be further researched in order to

determine the effect of the wake on the comfort levels at various seating positions in the trailing airliner.

It was determined that the control surface usage for the trailing airliner compared to the leading airliner did not yield straightforward results. It was found that the trailing airliner had a greater variance in aileron deflection during a simulation with turbulent conditions. This could be expected, as the wake vortex induces particularly strong rolling moments with large lateral and vertical separation derivatives. Perturbations of lateral and vertical separation would thus excite roll-mode dynamics, which is then regulated with the control system by means of the ailerons.

The elevator deflection however, yielded an unexpected result for the same simulation. It was found that the leading airliner consistently had much greater usage of its elevator compared to that of the trailing airliner. A possible explanation of this is that the leading airliner does more work with its elevator while regulating the altitude of the formation. As the turbulence experienced by all members of the formation is coupled, but delayed with time, it is expected that the turbulence would cause similar deviations from the desired flight trajectory for all members of the formation. Furthermore, complex interactions between the turbulence, the wake and the trailing airliner could also cause the trailing airliner to be effectively sucked into position behind the leading airliner vertically, though this is purely speculative.

Chapter 7

Conclusion and Recommendations

7.1 Conclusions

Throughout this thesis, formation flight proved itself an interesting topic well worth researching. The benefit of formation flight lies in the aerodynamic interactions of the trailing airliner with the wake vortices generated by the leading airliner. These interactions result in a reduction of induced drag of the trailing airliner, and thus a decrease in the required throttle setting for steady flight, which ultimately yields a fuel-consumption reduction benefit. This has great potential for cost-savings for airlines, as well as their passengers. Furthermore, the greater fuel efficiency will result in less air pollution and fewer greenhouse gas emissions; and will thus be a welcome attempt at reducing the industry's environmental impact. Formation flight does not come without challenges however. This thesis investigated these challenges and potential obstacles, concerning the control of the trailing airliner in formation flight. The complex, highly non-linear interaction forces and moments yield challenges concerning the flight mechanics of the trailing airliner, especially regarding the trim.

The main focus of the thesis however, was to design a flight control system for the formation flight of commercial, passenger airliners – which proved to be successful in varying levels of atmospheric turbulence. Furthermore, the developed controllers are simple, and closely resemble current fly-by-wire systems; opening the possibility of implementing them on current airliners.

Firstly though, a traditional model for an airliner in isolated flight was developed and expanded to include formation flight interactions. These interactions were presented as functions of vertical and lateral separation between the trailing and leading airliners. A trim analysis was done, and resulting actuator trims were presented over ranges of lateral and vertical separation.

Regions of reduced throttle setting were identified, as well as risks and challenges for maintaining formation within these regions. These regions comprise of a potentially risky and challenging region, coined the "sandwich region"; as well as a safer, more practically viable region, coined the "outer region" – illustrated on Fig. 7.1. The former is a narrow region sandwiched between

two regions that are untrimmable with respect to maximum aileron deflection, whereas the latter is only constrained by an inboard untrimmable bound, but has less significant throttle setting reduction.

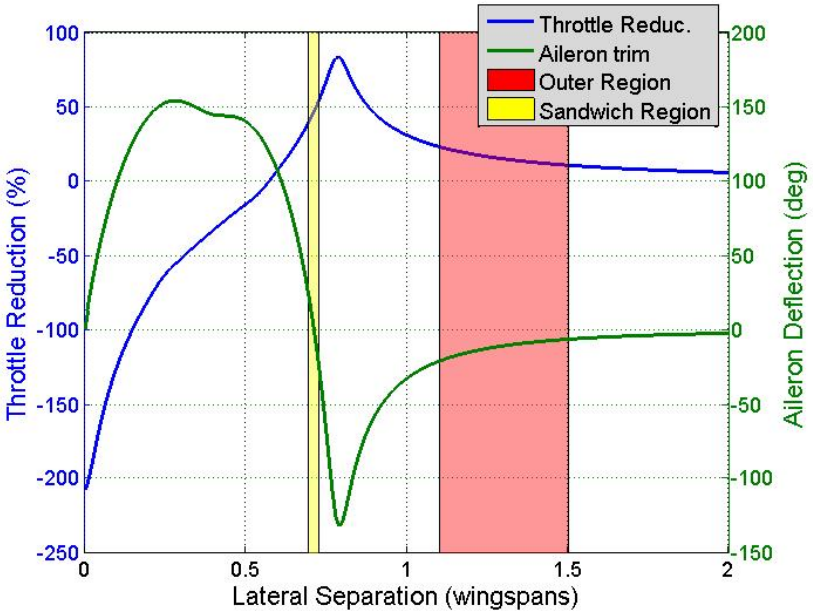

Figure 7.1: Trim comparison reveals "sandwich" region and "outer" trim regions.

Subsequently, a state space representation was constructed, which allowed for a linear dynamics analysis. It was determined that the trimmed, uncontrolled trailing airliner is naturally unstable; hence a flight control system is required for stability. Furthermore, the analysis revealed that the change in dynamics is effectively negligible, especially for the conventional modes, within the outer region. In the sandwich region however, the dynamics change much more drastically.

A control system for the conventional airliner was designed based on the available information of current representative fly-by-wire systems; and its performance was analysed in formation flight scenarios by means of both linear and non-linear simulations. It was found that, given sufficiently high control law gains, particularly for lateral controllers, the conventional architecture is sufficient for maintaining formation. Additional structures were suggested, such as saturation elements to limit the lateral separation rate and acceleration; and a state machine, with states for entering and exiting the wake vortices. A robustness analysis was then done, by once again evaluating the linear dynamics over ranges of lateral and vertical separation, though this time including the dynamics flight controllers in the linear models. The robustness analysis proved that the controllers are robust against lateral and vertical separation perturbation, at least in the outer region.

Finally, a series of non-linear simulations proved the success of the control system in maintaining formation in various conditions atmospheric turbulence conditions. The trailing airliner consistently showed a reduced throttle setting, though with greater dynamic throttling compared to

the leading airliner. Lastly, it was determined that the standard deviation of the control surface deflections of the trailing airliner is in the same order of magnitude as that of the leading airliner in simulations of moderate turbulence. Interestingly, it was found that the elevator deflection of the trailing airliner has a lower standard deviation than that of the leading airliner, possibly due to the leading airliner carrying the burden of regulating the formation's altitude.

Overall, the project was a success, and all research objectives were addressed. The non-linear and linear models were documented and verified for use in future projects. The trim and dynamics analysis yielded interesting, novel results pertaining to the trailing airliner's interactions with the wake vortices. Challenges and limitations relating to the trailing airliner's trim and dynamics were discussed, and practical recommendations were made where applicable. Controllers were designed for the conventional and trailing airliners; and the designs were verified in non-linear simulations. Finally, extended simulations evaluated the performance of the system in more realistic, as well as extreme, atmospheric turbulence conditions. The results of these simulations were very positive, and the trailing airliner controllers easily managed to fulfill the requirements of tracking a given relative position in the leader-generated wake vortices in formation flight.

7.2 Limitations of Work

This thesis discussed the first attempt at designing a control system for formation flight, and formed part of a series of formation flight projects in the collaboration between Stellenbosch University and the University of Cape Town. It lays the foundation for future projects, and covers a lot of ground. Though, throughout the projects, simplifications were made and some issues remained unsolved. A discussion of some of these follows:

- The engine and thrust model developed in this thesis is very simple. It is a first order model, which neglects pitching moments produced by the engines. This could have implications for the dynamic throttling of the engines, which could relate to tracking performance, passenger comfort and fuel consumption.
- The linear model, though verified with the non-linear model, contains an error for small, non-zero vertical separations, especially in the sandwich region. It is possible that this error was introduced during the augmentation of the controllers into the linear models, though this has not been confirmed. It may have something to do with the description of the flight path angle ($\gamma = \theta - \alpha$) in formation flight, as there is an extra induced angle of attack hidden away in the formation flight interaction terms, possibly not accounted for in this description. This is purely speculative however, and has not been verified.
- The engine dynamics and washout filter dynamics have only been included in the non-linear Simulink models, and not in the linear models used for the design. Though it was proven that these dynamics do not have a significant overall effect, it should be included for the sake of a more complete model.

7.3 Recommendations for Future Work

Though the project had a clear goal of developing controllers for the trailing airliner, capable of tracking a position in the leading airliner's wake vortices, it was largely open-ended with many avenues to explore – many of which have not been investigated during this thesis. In particular, passenger comfort and fuel consumption analyses are required to determine whether this project is practically viable for implementation on commercial airliners. Additionally, flight control systems could be designed to optimise for these aspects.

The research was limited to 2-ship formations, with a single leader and follower. Further research could be done to increase the size of the formation to three or more aircraft. This will also allow for the possibility of different formation configurations, such as the V, inverted-V or echelon. These configurations can be individually investigated and compared in terms of safety and fuel-economy.

The control laws designed during this thesis are intended for the purpose of tight formation flight. Furthermore, the Simulink environment was not structured in a way that could easily support a master controller based on a state machine architecture, without major structural changes. Motion limiting elements were added to prevent the system from reacting too aggressively to large inputs, which enables the controllers – designed for tight formation flight – to perform large manoeuvres successfully and with acceptable response. This situation is far from ideal however. The motion limiting elements are intended to enforce certain safety and performance margins; and were not designed for the purpose of performing specific manoeuvres, such as entry to and exit from the wake. As such, stability for these elements were never explicitly determined, other than non-linear simulations for selected initial conditions. Ideally, the state machine controller should reconfigure the control laws and saturation elements, according to the particular manoeuvre or formation configuration.

Lastly, higher level control systems to navigate and reorder the formation configuration could be investigated. This may include a master scheduler that could efficiently determine which flights are viable for grouping together in formation, and determine and schedule feasible routing options.

The individual state machine controllers would likely function as briefly discussed in this thesis. However, each state could be properly defined, investigated in more detail, and control laws designed to suit each individually. This would be done with the goal of entering and exiting the wake efficiently, comfortably and safely; and for different scenarios including hazards such as excessive turbulence, or catastrophic or partial failure of the leading airliner or other formation members.

These topics are likely only scratching the surface of the remaining work to be done towards the goal of ultimately achieving formation flight in commercial airliners, though they will certainly make good progress towards it.

Appendix A

Parameters, Constants and Calculated Gains

A.1 Stability Characteristics of the Boeing-747 and Corresponding Condition Parameters

The following parameters were used during thesis, and correspond to Condition 9 from Heffley and Jewel [24],

h	40 000 ft	M(mach number)	0.8
$\alpha(deg)$	4.6	$m(lbf)$	636 636
I_{xx}(slug-ft^2)	18.2×10^6	I_{yy}(slug-ft^2)	33.1×10^6
I_{zz}(slug-ft^2)	49.7×10^6	C_L	0.66
C_D	0.0415	C_{L_α}	4.92
C_{D_α}	0.425	C_{m_α}	-1.033
C_{L_α}	5.91	$C_{m_{\dot{\alpha}}}$	-6.41
C_{L_q}	6.00	C_{m_q}	-24.0
C_{L_M}	0.205	C_{D_M}	0.0275
C_{m_M}	0.166	$C_{L_{\delta_e}}$	0.367
$C_{m_{\delta_e}}$	-1.45	C_{y_β}	-0.88
C_{l_β}	-0.277	C_{n_β}	0.195
C_{l_p}	-0.334	C_{n_p}	-0.0415

C_{l_r}	0.3	C_{n_r}	-0.327
$C_{l_{\delta_a}}$	0.0137	$C_{n_{\delta_a}}$	0.0002
$C_{y_{\delta_r}}$	0.1157	$C_{l_{\delta_r}}$	0.007
$C_{n_{\delta_r}}$	-0.1256		

A.2 Calculated Control Law Gains

K_Q	-2.173
K_{E_C}	0.05
K_{n_z}	0.04
$K_{\bar{V}}$	50 000
K_γ	-80
K_ζ	-0.04
$K_{\int_\zeta}$	$0.03 \times K_\zeta$
$K_{\dot{\phi}}$	150
K_ϕ	$1.3 \times K_{\dot{\phi}}$
$K_{\Delta\psi}$	-80
$K_{\dot{\eta}}$	2.2
K_η	$0.12 \times K_{\dot{\eta}}$
$K_{\int_\eta}$	$0.02 \times K_\eta$
K_r	-1

Appendix B

Cramer's Rule

Cramer's rule [33] is an explicit formula for the solution of a system of simultaneous linear equations, with an equal number of equations and unknowns. It expresses the solution in terms of the determinant of the square coefficient matrix, and of matrices obtained by replacing one column by the vector of constants, usually on the right hand side of the equations.

A general system of equations that need to be solved is given, as follows:

$$\begin{aligned} a_{11}x_1 + a_{12}x_2 + \cdots + a_{1n}x_n &= b_1 \\ a_{21}x_1 + a_{22}x_2 + \cdots + a_{2n}x_n &= b_2 \\ a_{n1}x_1 + a_{n2}x_2 + \cdots + a_{nn}x_n &= b_n \end{aligned} \tag{B.1}$$

These can be rewritten as,

$$\mathbf{A}\mathbf{x} = \mathbf{b}, \tag{B.2}$$

where $\mathbf{A}$ is an n x n matrix of coefficients, $\mathbf{x} = (x_1, x_2, \ldots x_n)^T$, and $\mathbf{b}$ is a vector of constants. The solution to x_i, where $i = 1, 2 \ldots n$, is as follows:

$$x_i = \frac{|\mathbf{A}_i|}{|\mathbf{A}|}, \tag{B.3}$$

where $\mathbf{A}_i$ is formed by replacing the ith column of $\mathbf{A}$ by vector $\mathbf{b}$.

Bibliography

[1] Blake W., and Gingras D. R. "Comparison of predicted and measured formation flight interference effects," *AIAA, Journal of Aircraft*, vol. 41, pp. 201–207, 2004.

[2] Bower G., Flanzer T., and Kroo I. "Formation geometries and route optimization for commercial formation flight," *AIAA*, paper 2009-3615.

[3] Bizinos N., and Redelinghuys C. "Tentative study of passenger comfort during formation flight within atmospheric turbulence," *AIAA, Journal of Aircraft*, DOI:10.2514/1.C032018, 2012.

[4] Beukenberg M., and Hummel D. "Aerodynamics, performance and control of airplanes in formation flight," *ICAS*, paper 90-5.9.3, Bonn, Germany, 1990.

[5] Myatt J. H., and Blake W. "Aerodynamic database issues for modelling close formation flight," *AIAA*, paper 99-4194, 1999.

[6] Gingras D. R. "Experimental investigation of multi-aircraft formation," *17th Applied Aerodynamics Conference, AIAA*, paper 99-3143, Norfolk, VA, 1999.

[7] Kless J., Aftosmis, M. J., Ning S. A., and Nemec M. "Inviscid analysis of extended formation flight," *AIAA Journal*, vol. 51, no. 7, July 2013.

[8] Garodz L. J. "FAA full scale aircraft vortex wake turbulence flight test investigations: past, present, future," National Aviation Facilities Experimental Center, *AIAA*, paper 71-97, Norfolk, VA, 1971.

[9] Tinling B. E. "Estimation of vortex induced roll excursions based on flight and simulation results," *Proceedings of the Aircraft Wake Vortex Conference*, Federal Aviation Administration Rept. FAA-RD-77-68, edited by Hallock, J. N., pp. 1122, 1977.

[10] Green G. C., Dunham R. E. Jr., Burnham D. C., Hallock J. N. and Rossouw V. J. "Wake vortex research – Lessons learned," *Proceedings of the Aircraft Wake Vortex Conference*, Dept. of Transportation Rept. DOT-VNTSC-FAA-92-07, edited by Hallock, J. N., pp. 2-12-13, 1992.

[11] O'Callaghan J. J. "Flight control and wake turbulence effects on American airlines Flight 587," *AIAA Modelling and Simulation Technologies Conference and Exhibit*, paper 2005-6110, San Francisco, California, 2005.

[12] Misaka T., Ogasawara T., and Obayashi S. "Measurement integrated simulation of wake turbulence," *AIAA Aerospace Sciences Meeting and Exhibit*, paper 2008-466, Reno, Nevada, 2008.

[13] Burnham D. C., and Hallock J. N. "Chicago monostatic acoustic vortex sensor system," U. S. Dept. of Transportation Rept. DOT-TSCFAA-79-103.IV, 1982.

[14] Zou Y., Pagilla P. R., and Ratli R. T. "Distributed formation flight control using constraint forces," *Journal of Guidance, Control and Dynamics*, vol. 32, no. 1, DOI:10.2514/1.36826, 2008.

[15] Brodecki M., Kamesh S., and Qi-Ping C. "Formation flight control system for in-flight sweet spot estimation," *AIAA, Aerospace Sciences Meeting including the New Horizons Forum and Aerospace Exposition*, paper 2013-1037, 2013.

[16] Brodecki M., Kamesh S., and Qi-Ping C. "Emergent behavior of multi-vehicle formations using extremum seeking," *AIAA, Aerospace Sciences Meeting including the New Horizons Forum and Aerospace Exposition*, paper 2013-1033, 2013.

[17] Henmati M. S., Eldredge J. D., and Speyer J. L. "Wake sensing for formation flight," *Journal of Guidance, Control and Dynamics*, vol. 37, no. 2, DOI: 10.2514/1.61114, 2014.

[18] Okolo W., Blake W., and Dogan A. "Determination of sweet spot for trailing aircraft in formation flight," *AIAA, Atmospheric Flight Mechanics Conference*, paper 2011-6302, 2011.

[19] Chichka D. F., Speyer J. L., Fanti C., and Park C. G. "Peak-seeking control for drag reduction in formation flight," *Journal of Guidance, Control and Dynamics*, vol. 29, no. 5, 2006.

[20] Binetti P., Ariyur K. B., Miroslav K., and Bernelli F. "Formation flight optimization using extremum seeking feedback," *Journal of Guidance, Control and Dynamics*, vol. 26, no. 1, 2003.

[21] Xu J., Ning S. A., Bower G., and Kroo I. "Aircraft route optimization for formation flight," *Journal of Aircraft*, vol. 51, no. 2, March–April 2014.

[22] Kun Z., Lixin W., and Xiangsheng T. "Flying qualities reduction of fly-by-wire commercial aircraft with reconfigurable flight control laws," *IASSA, 2nd International Symposium of Aircraft Airworthiness*, doi:10.1016/j.proeng.2011.10.021, 2011.

[23] Hanke C. R., and Nordwall D. R. "The simulation of a jumbo jet transport aircraft volume II: Modeling data,", The Boeing Company, D6-30643, 1972.

[24] Heffley R. K., and Jewell W. F. "Aircraft handling qualities data," NASA CR-2144, 1972.

[25] "Military Specification," [Online]. Available: www.mechanics.iei.liu.se/edu_ug/tmme50/8785c.pdf

[26] US Department of Defense."Flying qualities of piloted aircraft," [Online]. Available: www.mechanics.iei.liu.se/edu_ug/tmme50/MIL-HDBK-1797.PDF

[27] Zipfel P. H. "Modeling and simulation of aerospace vehicle dynamics, 2nd edition," *AIAA Eduction Series*, 2007.

[28] Cook M. V. "Flight dynamics principles, 2nd edition," Elsevier Butterworth-Heinemann, 2007.

[29] Caughey D. A. "Introduction to aircraft stability and control," Sibley School of Mechanical and Aerospace Engineering, Cornell University, 2011.

[30] Etkin B. "Dynamics of atmospheric flight," chapter 13. John Wiley and Sons Inc., 1972.

[31] Engelbrecht J. A. A., Pauck S. J., and Peddle I. K. "A multi-mode upset recovery flight control system for large transport aircraft," *AIAA*, doi:10.2514/6.2013-5172, 2013.

[32] Peddle I. K. "Acceleration based manoeuvre flight control system for unmanned aerial vehicles," *PhD dissertation*, Stellenbosch University, 2008.

[33] Cramer G. "Introduction à l'Analyse des lignes Courbes algébriques," (in French). Geneva: Europeana, pp. 656-659, 1750.